

**Active Quasi-Optics  
and  
Measurements**

**Thesis by**

**Blythe Chadwick Deckman**

In Partial Fulfillment of the Requirements

for the Degree of

Doctor of Philosophy

California Institute of Technology

Pasadena, California

2000

(Submitted May 4, 2000)

To Christ, for giving me life and breath with which to study; to my wife, for her encouragement, attention, and understanding; and to my parents for their example of diligence and tenacity.

## Acknowledgements

For first the opportunity to study under him, and then his many insights, I thank Dr. David Rutledge. To say that there have been numerous instances where Dr. Rutledge has helped stretch my analytical abilities would be an understatement. After about 20 minutes of fiddling with a proof, an office mate and I came up empty handed. When I asked Dr. Rutledge for a tip, the reply was, "I've got a one-liner for that!" Such were many occasions. Many thanks to you, Dave!

I am equally grateful for the talented researchers at Rockwell Science Center: Emilio Sovero, Jon Hacker, Moonil Kim, Don Deakin, and Aiden Higgins, to name a few. The competent advice that they gave and patience with which each of them investigated aspects of this work, I greatly appreciate.

My wife, Wendy, has been a tremendous supporter for whom I am grateful beyond words. From listening to me ramble on about transistors and waveguides (and remembering how they operate), to just being a Proverbs 31 wife, I thank you Wendy from all of me.

To my parents, who provided not only a clear example of commitment to professional excellence, but also of personal excellence, I should surrender equal claims to this work. Without them, I would not have made it through school. They are wise, encouraging, understanding, and righteous. Many thanks to you, folks!

I am indebted to the students and adjuncts of the MMIC group at Caltech, especially Lawrence Cheung (the Volcan); Taavi Hirvonen, Alina Moussessian, John Davis, Polly Preventza, and Ichiro Aoki for many discussions of many things. Jim Rosenberg has been particularly inspiring and helpful with both microwave circuits and device physics. I am truly grateful for his attention to me.

For in Him we live, and move, and have our being.

—Acts 17:28

## Abstract

Quasi-optical grid amplifiers and oscillators have been limited in power to less than a watt at Ka-band until recently. Additionally, measurements of grid structures have been done with far-field techniques, making reflection measurements difficult. Some focused techniques have been used as well. Here are presented a 5-watt grid amplifier at 37.2 GHz, and a grid oscillator, after Moonil Kim, that shows 1 watt of effective transmitter power at 38 GHz. Focused beam measurement techniques are also discussed, introducing a new method to calibrate a network analyzer for reflection measurements. Measurements are presented on passive structures to validate the calibration technique, and then measurements of the active structures are presented.

Following the presentation of the 5-watt amplifier and 1-watt oscillator, a design technique for a 10-watt grid amplifier is presented, along with a mode converter that allows the grid to be fed from a standard waveguide port.

## Contents

<b>Acknowledgements</b> .....	iii
<b>Abstract</b> .....	v
<b>Chapter 1. Introduction</b>	
1.1. Motivation .....	1
1.2. Approaches.....	5
1.3. Modeling.....	6
1.4. Goal and Thesis Organization .....	7
<b>Chapter 2. Design of The First Grid and Performance</b> .....	14
2.1. Heat Removal.....	15
2.2.1. Lumped-Element Models .....	18
2.2.2. Full Electromagnetic Model.....	24
2.3. Unit Cell Design .....	27
2.4. Stability .....	31
2.5. First Grid Performance .....	38
<b>Chapter 3. High-Power Design and Performance</b> .....	44
3.1. Successful Grid Amplifier.....	46
3.2. Thermal Measurements.....	58
<b>Chapter 4. Measurements</b> .....	63
4.1. Description of Far-Field Measurement Techniques.....	63
4.2. Gaussian Beam Optics .....	65
4.3. Calibration.....	71
4.3.1. Calibration For Transmission Measurements .....	72
4.3.2. Calibration For Reflection Measurements .....	73
4.4. Power Measurements .....	83
<b>Chapter 5. A Kim Oscillator</b> .....	90
5.1. Oscillator Theory.....	90

5.2. Traditional Feedback Theory .....	91
5.3. Augmented Feedback Analysis .....	92
5.4. Grid Oscillators .....	94
<b>Chapter 6. Future Work</b> .....	<b>105</b>
6.1. A 10-W Grid .....	105
6.2. Waveguide Feed .....	108
6.3. Electronically Tuned Grid Oscillator .....	113
<b>Appendix 1. Gaussian Beams</b> .....	<b>116</b>

# Chapter 1

## Introduction

Quasi-optics found its beginnings before World War II, as Professor Uda of Tohoku University in Sendai, Japan, performed experiments with arrays of dipole antennas driven by vacuum tubes [24]. It wasn't until the late 1980's, with rapidly increasing demands for higher powers at higher frequencies, that the field began to draw the significant research attention it continues to receive today. Transmitter systems that require moderate to high powers and operate in the microwave and millimeter wave regions still use vacuum tube power amplifiers. Quasi-optics offers a promising solution to problems that have historically limited solid-state designs to low power levels, so it is no surprise that much of the research effort in the field has been devoted to amplifiers [1-12]. Recent amplifier results have begun to offer power levels approaching those attainable with lower power microwave tubes [25]. Along with amplifiers, Quasi-optical oscillators [16-20], mixers [22, 23], and frequency converters [21] have all been successfully demonstrated.

### 1.1 MOTIVATION

Fundamental properties of solid state devices that operate at millimeter and sub-millimeter wavelengths impose power limits on individual devices that remain quite low compared to increasing power level demands. (For example, a currently available FET that operates at Ka-band and is suitable for power

use can supply approximately 60 mW at about 2-dB gain compression.) Consequently, a combination scheme for the outputs of many devices is required to meet power specifications. Small-scale combination can be readily achieved using a typical transmission line combination scheme, and currently available MMICs use such designs to achieve powers of 2 Watts or less at Ka-band. Figure 1 shows a plot of available MMIC power using various device technologies and circuit combination schemes.

There is, however, a limit imposed by the losses in realizable designs on the number of devices whose outputs can be combined using a typical transmission line combination circuit. Figure 2a shows a plot of the output power as a function of the number of devices combined using a transmission line combiner similar to that shown in figure 2b. With reference to figure 2b, the number of  $\lambda/4$  sections of transmission line necessary for the circuit is  $N/2$ , where  $N$  is the number of individual devices whose outputs are combined. If  $L$  is the transmission coefficient of a single  $\lambda/4$  section ( $L$  close to unity for low loss), then the normalized power

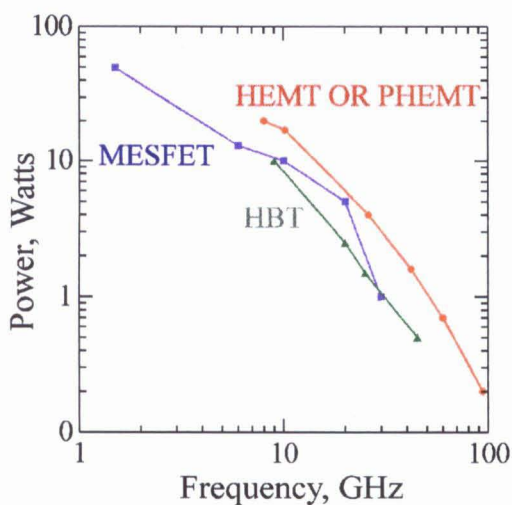


**Figure 1.** Comparison of the available powers for various technologies. Courtesy of Dr. Elliott Brown, DARPA ETO.

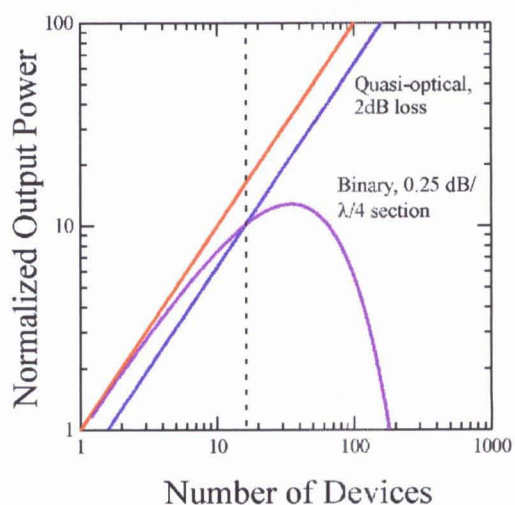


**Figure 2a.** Loss comparison between quasi-optic and traditional transmission line combination schemes.

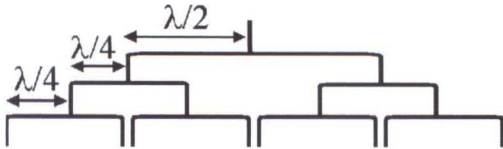


**Figure 2b.** Typical binary power combiner. Note that the separation between combination arms increases by a factor of 2 with each additional stage of combination.

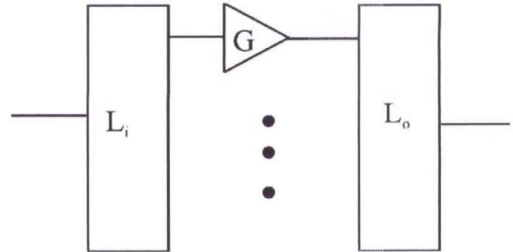


**Figure 2c.** General system showing power splitter and combiner.

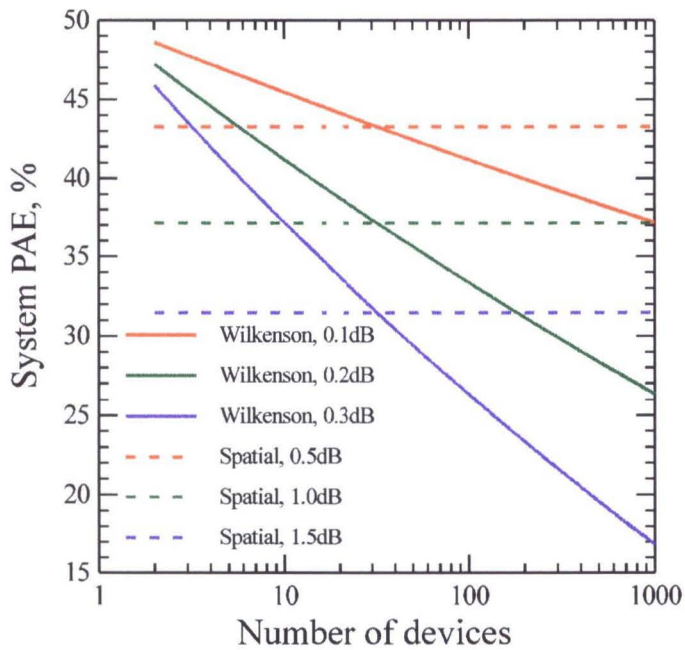


**Figure 2d.** Comparison between system PAE for quasi-optic and circuit splitters and combiners. The cross-over occurs at about 30 devices. Courtesy of Robert York of U.C. Santa Barbara.

delivered by the combiner is  $N \cdot (10)^{N/2}$ . Figure 1a shows the plot. As shown in the figure, the output power from a transmission line power combiner using even low-loss materials *is a convex function* with a peak around 60 devices.

There may be an even more fundamental limit on the number of devices that can be combined using a circuit combiner. The major disadvantage of the combiner circuit in figure 2b is that the lengths of transmission lines increases rapidly with the number of combined devices. The limiting case for the binary combiner results if all sections of transmission line could be reduced to  $\lambda/4$ . After Robert York of U.C. Santa Barbara, an approach from an efficiency calculation can show when a quasi-optic power combiner should be used. With reference to figure 2c, the system power-added efficiency is given by

$$PAE = \frac{L_i G L_o - 1}{(G - 1) L_i} \eta_a$$

where  $L_i$  is the loss per stage at the input power splitter assuming all stages use transmission lines exactly  $\lambda/4$  long,  $L_o$  the loss per stage at the output power combiner,  $G$  the gain of the amplifiers, and  $\eta_a$  the power-added efficiency of the amplifiers driving the combiner. Figure 2d shows a plot of the power-added efficiencies for quasi-optic power splitters and combiners compared to circuit splitters and combiners. As shown, for combination above about 30 devices (assuming a 50% PAE for each device) a quasi-optic system is advantageous.

Apart from the losses associated with typical circuit combiners, the complexity and size of the combiners scales rapidly with the number of devices. As a consequence, the limit on the number of outputs that may be combined using such a design may be set by the allowable size of the circuit before the number of combined devices reaches the peak of the curve in figure 2a.

The quasi-optic approach, so named for its design to operate with beams instead of guided waves, combines the outputs of many devices radiatively into a uniform medium (usually free space or a carefully designed oversized waveguide). As such, a complex transmission line combiner circuit is reduced to an array of

radiating elements operating in parallel, and the loss is reduced to that associated with a single radiator. Careful quasi-optic MMIC design leads to coherent combination of the radiated fields from each element, and the power available from such a design *scales linearly* with the number of devices on the MMIC, as figure 2a shows.

## 1.2 APPROACHES

Numerous design approaches to quasi-optic amplifiers have been successfully used, and they fall, naturally, into the categories of monolithic and hybrid designs. Hybrid designs have to date shown the greatest power capacities, with higher system complexity and cost associated. York *et al.* [6] of U. C. Santa Barbara have constructed an amplifier by populating free space-to-slot line transitions (printed metal transitions on a thermally conductive substrate) with power MMIC chips to achieve 60 watts<sup>1</sup> at X-band. Hubert *et al.* [7] of Lockheed Martin designed an over-moded waveguide loaded with dielectric material on two opposing walls to feed a through-plate coupler populated with 45 power MMIC chips to give 4 watts<sup>2</sup> at Ka-band.

Various monolithic designs have been successfully demonstrated [1-5, 12, 25-26] that show lower available powers than hybrid designs, but have the added advantage of simpler fabrication that may be suitable for production in moderate to high volumes. The costs associated with monolithic designs are considerably lower than hybrid designs as well. Among the monolithic designs, grid amplifiers have been demonstrated to operate up to Ka- and U-band frequencies. Liu *et al.* [4] of Caltech produced a grid amplifier giving 670 mW at 44 GHz. Hacker *et al.* [26] of Rockwell Science Center demonstrated a grid amplifier operating at 38 GHz and giving about 2 watts. Continued work on this amplifier yielded

---

<sup>1</sup> Presented results for this amplifier at MTT-S 1999 showed 150 watts.

<sup>2</sup> Presented results for this amplifier at MTT-S 1999 showed 25 watts.

4 watts of saturated power<sup>3</sup> [27]. The work presented throughout this document details the development of a Ka-band, monolithic grid amplifier that gives 5 watts at 5 dB gain.

### 1.3 MODELING

The structure of a monolithic grid amplifier consists of several sheets of concatenated dielectric material (possibly separated by air gaps) with various metal patterns and semiconductors constructed on them; figure 3 shows the layout of the grid amplifier presented here. Modeling of the structure begins by deducing the impedances of the various metal patterns by use of electromagnetic analysis. Weikle [29] developed a method to analyze simple metal gratings printed

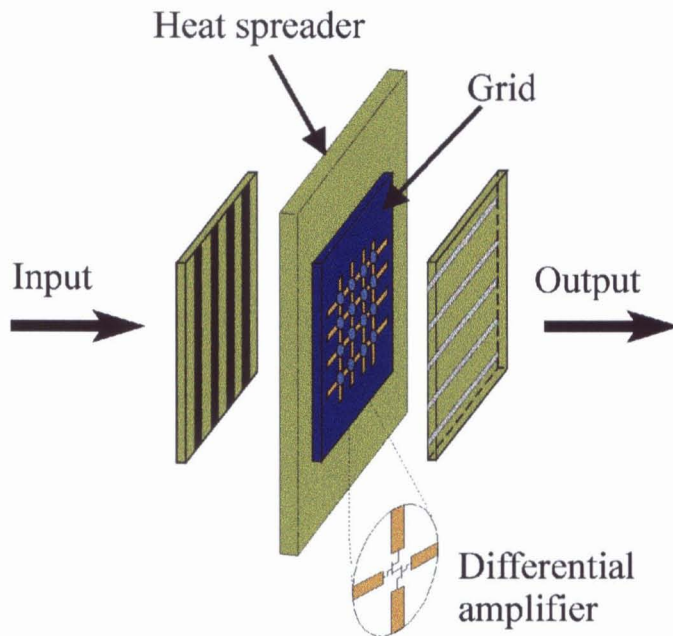


**Figure 3.** Grid amplifier layout. Detail shows the configuration of the transistors.

<sup>3</sup>The gain of the amplifier at 4 watts output was 0 dB.

on a dielectric substrate by deducing an EMF at symmetry points from surface currents on the gratings. Provided that the dimensions of the metal patterns remain small compared to a wavelength, the current distributions on them can be assumed with reasonable<sup>4</sup> accuracy. De Lisio extended Weikle's method, incorporating the method of moments to generate a better estimate of the current distribution on the grating metal patterns [28]. Figure 4 shows a generic grid pattern that can be analyzed using Weikle's method; the dashed lines show De Lisio's division of the patterns suitable for application of the moment method.

Once the metal patterns have been analyzed for an EMF, scattering parameters usable in standard circuit analysis programs can be generated, reducing the modeling of a grid amplifier to simple circuit elements. The grid amplifiers in [4, 5, 28] were analyzed after this technique, and significant agreement between model predictions and measured results was found.

Other modeling techniques have emerged as well. Steer *et al.* [13] have

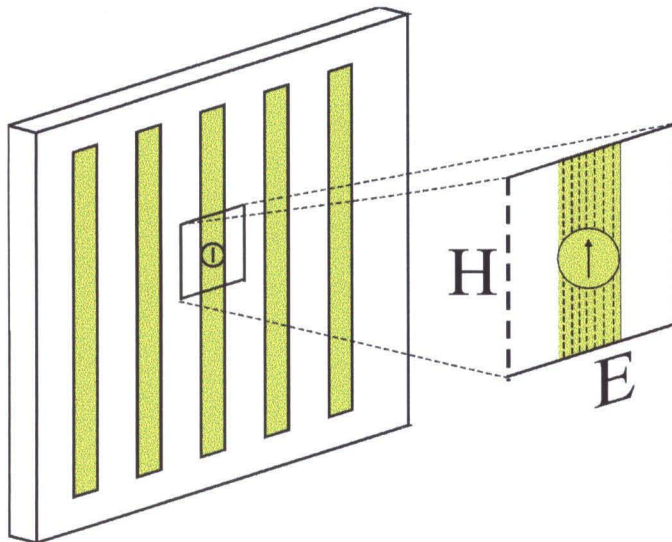


**Figure 4.** Typical model used with Weikle's method. Uniform current is assumed across the strip, as shown by the current source. The vertical dashed lines show De Lisio's division of the strip into smaller strips, and a current source would be associated with each.

<sup>4</sup>De Lisio showed that Weikle's method assuming a uniform current distribution is accurate to within 20%.

worked on full-wave simulations of specific geometries of grid amplifiers. With the advancement of computer speed and finite-element techniques, simulation of arbitrary geometries has become more realistic. Ansoft's High Frequency Structure Simulator (HFSS) uses finite-element techniques to analyze complex structures and produce scattering parameters for them. Preventza *et al.* [14] have developed two modeling techniques based on HFSS calculations that account for many of the parasitic interactions between the metal patterns on grid amplifiers, and excellent agreement between modeled and measured responses was shown. The modeling used throughout this work is after [14].

#### 1.4 GOAL AND THESIS ORGANIZATION

The grid amplifier in [4] was a 10x10 array mounted on a duroid carrier with no cooling plan implemented. As such, the grid could be powered on for less than one second at a time, and a 3-minute cooling time was required before reapplication of the bias. The goal of this work has been to demonstrate a monolithic grid amplifier capable of delivering 5 watts of power at Ka-band. The size of the grid, hence, needed to be even larger than that in [4], necessitating an external cooling plan. But beyond the heat removal issue, the size of the grid required long bias lines, immediately introducing a bias uniformity concern from the finite conductivity of the gold bias line traces.

Chapter 2 describes the design of the first iteration grid amplifier, including the heat removal plan and bias distribution plan. Modeling is discussed in greater detail, and results for model verification experiments are presented. The stability design for the grid amplifier is also discussed in some detail, and finally results for the fabricated array are presented.

Chapter 3 presents the second iteration grid, which meets the power goal of the program. An infrared image of a fully biased amplifier is presented, in conjunction with predictions from the simulations, and it is shown that the thermal performance of the grid amplifier is such that its temperature remains well below

the typical power amplifier operating temperature. An estimate of the power combination efficiency is also presented at the conclusion of chapter 3.

Chapter 4 shows the measurement setup and techniques used to characterize the grid amplifier. Calibration techniques for reflection and transmission measurements are described, and test measurements are shown to validate the accuracy of the calibrations.

Chapter 5 presents results obtained for an oscillator constructed by designing external feedback around the successful 5-W amplifier.

Chapter 6 introduces a design for a 10 watt grid amplifier with a slightly more efficient cooling design. Current and future work in quasi-optic amplifiers is presented.

Finally, a derivation of gaussian beam parameters is presented in the appendix.

## References

- [1] M. Kim, J.J. Rosenberg, R.P. Smith, R.M. Weikle, J.B. Hacker, M.P. DeLisio, D.B. Rutledge, "A grid Amplifier," *IEEE Microwave Guided Wave Letters*, vol. 1, pp. 322-324, November, 1991.
- [2] M. Kim, E.A. Sovero, J.B. Hacker, M.P. De Lisio, J.C. Chiao, S.J. Li, D.R. Gagnon, J.J. Rosenberg, D.B. Rugledge, "A 100-Element HBT Grid Amplifier," *IEEE Trans. Microwave Theory Tech.*, vol. 41, pp. 1762-1771, October, 1993.
- [3] C.M. Liu, E.A. Sovero, M.P. De Lisio, A. Moussessian, J.J. Rosenberg, D.B. Rutledge, "Gain and Stability Models for HBT Grid Amplifiers," *IEEE AP-S Int. Symp. Dig*, pp. 1292-1295, 1995.
- [4] C.M. Liu, E.A. Sovero, W.J. Ho, J.A. Higgins, M.P. De Lisio, D.B. Rutledge, "Monolithic 40-GHz 670-mW HBT Grid Amplifier," *IEEE International Microwave Symposium Diag.*, pp. 1123-1126, 1996.
- [5] M.P. De Lisio, S.W. Duncan, D.W. Tu, S.Weinreb, C.M. Liu, D.B. Rutledge, "A 44-60 GHz Monolithic pHEMT Grid Amplifier," *IEEE International Microwave Symposium Diag.*, pp. 1127-1130, 1996.
- [6] Nai-Shuo Cheng, Thai-Phuong Dao, Michael Case, David Rensch, Robert York, "A 60-Watt X-Band Spatially Combined Solid-State Amplifier," *IEEE International Microwave Symposium Diag.*, pp. 539-542, June, 1999.
- [7] J. Hubert, L. Mirth, S. Ortiz, A. Mortazawi, "A 4 Watt Ka-Band Quasi-Optical Amplifier," *IEEE International Microwave Symposium Diag.*, pp. 551-554, June, 1999.
- [8] C.E. Saavedra, W. Wright, K.Y. Hur, et al., "A millimeter-wave quasi-optical amplifier array using inclined-plane horn antennas," *IEEE Microwave and Guided Wave Letters* vol. 8, no. 2, pp. 81-83 February, 1998.

- [9] N.J. Koliass, R.C. Compton, "A monopole-probe-based quasi-optical amplifier array," *IEEE Transactions on Microwave Theory and Tech.* 45: (8) 1204-1207 Part 1 AUG 1997.
- [10] T.P. Budka, M.W. Trippe, S. Weinreb, et al., "A 75 GHz to 115 GHz Quasi-Optical Amplifier," *IEEE Transactions on Microwave Theory and Tech.* 42: (5) 899-901 May, 1994 .
- [11] A. Alexanian, R.A. York, "Broadband spatially combined amplifier array using tapered slot transitions in waveguide," *IEEE Microwave and Guided Wave Letters* 7: (2) 42-44 February, 1997.
- [12] H.S. Tsai, M.J.W. Rodwell, R.A. York, "Planar Amplifier Array With Improved Bandwidth Using Folded-Slots," *IEEE Microwave and Guided Wave Letters* 4: (4) 112-114 April, 1994.
- [13] M. Abdulla, U. A. Mughal, H.S. Tsai, M.B. Steer, R.A. York, "A Full-Wave System Simulation of a Folded-Slot Spatial Power Combining Amplifier Array," *IEEE International Microwave Symposium Diag.*, pp. 559-561, June, 1999.
- [14] P. Preventza, B. Dickman, E. Sovero, M.P. De Lisio, J.J. Rosenberg, D.B. Rutledge, "Modeling of Quasi-Optical Arrays," *IEEE International Microwave Symposium Diag.*, pp. 563-566, June, 1999.
- [15] M. Kim, J.B. Hacker, A.L. Sailer, S. Kim, D. Sievenpiper, J.A. Higgins, "A Rectangular TEM Waveguide with Photonic Crystal Walls for excitation of Quasi-Optical Amplifiers," *IEEE International Microwave Symposium Diag.*, pp. 543-546, June, 1999.
- [16] M. Kiyokawa, T. Matsui, "A New Quasi-Optical Oscillator With Gaussian Output Beam," *IEEE Microwave Guided Wave Letters*, 4: (5) pp. 129-131, May, 1994.
- [17] R.A. York, "Nonlinear-Analysis of Phase-Relationships In Quasi-Optical Oscillator Arrays," *IEEE Transactions on Microwave Theory And Techniques*, 41: (10) pp. 1799-1809, October, 1993.

- [18] J. Bae, Y. Aburakawa, H. Kondo, et al., "Millimeter And Submillimeter-Wave Quasi-Optical Oscillator With Gunn-Diodes," *IEEE Transactions on Microwave Theory And Techniques*, 41: (10) pp. 1851-1855, October, 1993.
- [19] H.C. Yin, Y.J. He, Q.R. Yang, "Input Impedance of Microstrip Patch In The Quasi-Optical Cavity Resonator," *International Journal of Infrared And Millimeter Waves*, 14: (11) pp. 2379-2386, November, 1993.
- [20] H. Kondo, M. Heida, M. Nakayama, et al., "Millimeter and Submillimeter Wave Quasi-Optical Oscillator With Multi-Elements," *IEEE Transactions on Microwave Theory And Techniques*, 40: (5) pp. 857-863, May, 1992.
- [21] A. Moussessian, M.C. Wanke, Y.J. Li, et al., "A terahertz grid frequency doubler," *IEEE Transactions on Microwave Theory And Techniques*, 46: (11) 1976-1981 Part 2, November, 1998.
- [22] R. Swisher, F. Lecuyer, I.F. Chio, J.C. Chiao, M.P. De Lisio, "A Blaanced Diode Grid Mixer," *IEEE International Microwave Symposium Diag.*, pp. 555-558, June, 1999.
- [23] S.V. Robertson, L.P.B. Katehi, G.M. Rebeiz, "A Planar Quasi-Optical Mixer Using A Folded-Slot Antenna," *IEEE Transactions on Microwave Theory And Techniques*, 43: (4) pp. 896-898, Part 1, April, 1995.
- [24] R.A. York, Z.B. Popovic, *Active And Quasi-Optical Arrays*, John Wiley Sons, Inc., New York, 1997.
- [25] B. Dickman, E. Sovero, D. Deakin, D. Rutledge, "A 5-Watt Ka-Band Grid Amplifier," *To be published in the 2000 IEEE International Microwave Symposium Digest*.
- [26] E.A. Sovero, J.B. Hacker, J.A. Higgins, D.S. Deakin, A.L. Sailer "A Ka-Band Monolithic Quasi-Optic Amplifier" *IEEE International Microwave Symposium Diag.* pp. 1453-1456, June, 1998.

- [27] J.A. Higgins et al., *Final Report, Contract No. N66001-96-C-8627*, prepared for Paul de la Houssaye, Communications and INFOSEC Systems Support and Integration Division, SPAWAR Systems Center, San Diego, November, 1999.
- [28] R.M. Weikle, "Quasi-Optical Planar Grids for Microwave and Millimeter-Wave Power Combining," Ph.D. Thesis, California Institute of Technology, Pasadena, Ca., 1992.

## Chapter 2

### Design of The First Grid and Performance

The goal of the grid amplifier presented here is to deliver 5 watts of power at Ka-band. The transistors selected for the task are GaAs *p*HEMTs supplied by Rockwell Science Center. Each transistor has a gate width of  $80\ \mu\text{m}$ , a gate length of  $0.18\ \mu\text{m}$ , and is capable of supplying more than 10 mW of power at Ka-band. An output specification of 5 watts, then, requires at least 500 such transistors operating together. So that the symmetry of the grid amplifier would be maintained, a square grid was designed with 16 unit-cells per side, each containing two transistors. Figure 2.1 shows a simplified view of the unit cell with its corresponding electric and magnetic symmetry planes (with respect to the input polarization).

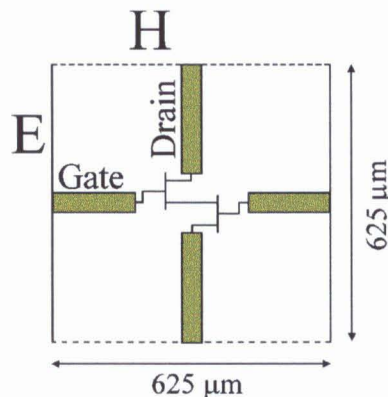


**Figure 2.1.** Unit cell layout.

## 2.1 HEAT REMOVAL

Assuming a power-added efficiency of 20%, a cooling system capable of dissipating 17 watts of waste heat while maintaining a transistor junction temperature below 150°C is needed<sup>1</sup>. Taking a thin heat spreader with uniform heat flux incident from the top, isothermal sides, and an insulating bottom, a very rough estimate of the temperature rise at the center of the spreader is given by  $\Delta T = Q/2\pi Kt$ , where  $Q$  is the heat flux,  $K$  the thermal conductivity (W/mK), and  $t$  the thickness of the spreader. Roughly, then, the grid amplifier temperature rise goes as the inverse of the product of the thickness of the spreader and its thermal conductivity. Table 2.1 lists common materials and their properties suitable for microwave circuits. From the table and the estimate of the temperature rise, it is obvious that neither duroid, alumina, nor fused quartz is suitable for use as a heat spreader here, and that the active GaAs substrate should be as thin as practically feasible. Diamond offers the best thermal performance but was not readily available in dimensions germane to the grid amplifier design<sup>2</sup>. Consequently, aluminum nitride was selected as the thermal spreader.

Figure 2.2 shows a layout for the thermal design. In order to minimize

Material	$\epsilon_r$	Thermal Cond. (W/mK)
GaAs	13.2	46
Duroid	2.2	0.4
Fused Quartz	4.0	1.38
Alumina	9.3	31
BeO	6.4	254
Aluminum Nitride	8.6	170
Diamond	5.6	1000
Copper	-	394

**Table 2.1.** Common microwave materials and their properties.

<sup>1</sup> 30% PAE had been measured for individual transistors; 20% was used here to include a safety margin.

<sup>2</sup> Recently, CVD techniques for growing diamond have enabled vendors to deliver substrates up to 1.8 mm thick, and up to 4 inches square. The cost is currently about \$50/cm<sup>2</sup>.

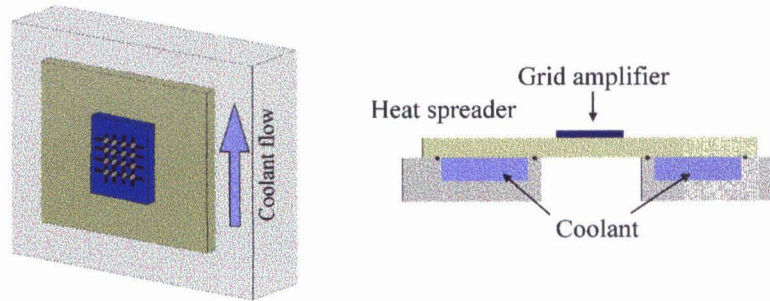


**Figure 2.2.** Thermal management. Water circulates around the bottom edges of the heat spreader at 4 liters per minute.

heating from the poor thermal conductivity of the GaAs substrate, the fabricated chip was thinned to  $75\ \mu\text{m}$ . A thermal polymer less than 1 mil thick, loaded with aluminum nitride, attaches the grid to the heat spreader. The thermal spreader is attached to a plastic frame with a water channel machined into it. Water circulating around the lower edges of the heat spreader conducts waste heat away, holding the edge temperatures of the spreader constant.

Because the aspect ratio of the gate length to the size of the heat spreader is entirely impractical for direct simulation, thermal modeling of the structure was performed in two parts, using a finite-element thermal simulator by Tanner Research. The first simulation assumed a uniform heat flux (equal to the dissipated power in the amplifier) over the GaAs area of the grid amplifier. The result gives an estimate of the average temperature rise of the bulk GaAs substrate. The second simulation was performed on a single unit-cell, surrounded by isothermal walls, with the heat flux provided by the gate fingers of the transistors in the cell. Adding the peak temperatures from both simulations yields an estimate of the temperature rise of GaAs in the area close to the gates<sup>3</sup>. Figure 2.3 shows the simulated heat profiles for the two cases.

To investigate the accuracy of the thermal model, a fabricated amplifier that

<sup>3</sup>The aspect ratio between the transistor gates and the unit-cell is again such that the simulation produces temperature rise data only in the vicinity of the gate. The actual gate temperature is expected to be slightly higher.

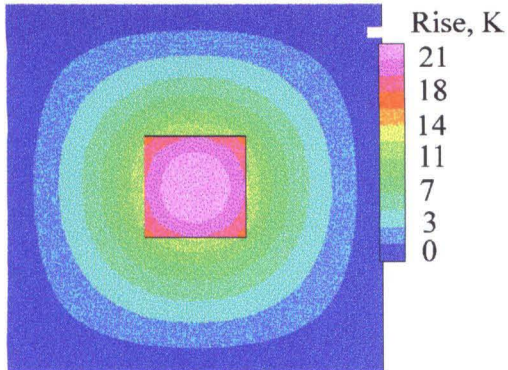


**Figure 2.3a.** Thermal simulation assuming a uniform heat flux incident on the entire GaAs area.

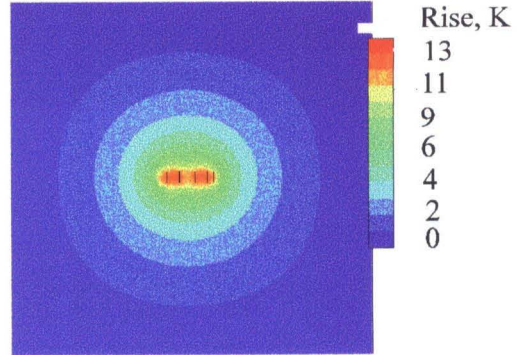


**Figure 2.3b.** Thermal simulation of a single unit cell with the heat flux provided by the gate fingers of the transistors in the cell.

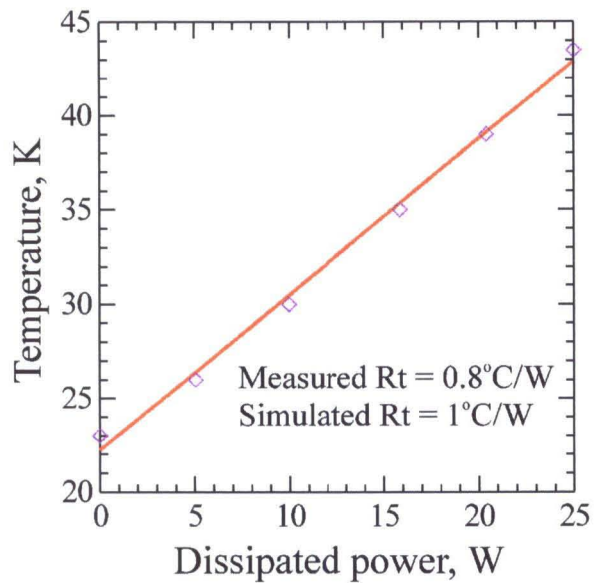


**Figure 2.4.** Thermal test measurement. Measured data points are plotted as symbols; the solid line is a linear fit. The data were measured with a mercury thermometer, using thermal paste to ensure contact, at the center of the grid under varying bias applied.

showed poor RF performance was mounted and biased. A mercury thermometer was gently placed at the center of the grid with sufficient thermal paste to ensure good thermal contact. The bias applied to the chip was varied, and the temperature of the center of the grid was plotted as a function of the applied power. Figure 2.4 shows the measured temperature rise of the center of the grid amplifier. As the plot shows, measured data agrees well with the model predictions, showing the grid amplifier to operate well below the typical maximum temperature of 150°C.

### 2.2.1 LUMPED-ELEMENT MODELS

Analysis of a finite structure illuminated by an impinging field is in general a forbidding task. Edge effects from the finite structure are at best difficult to model, and coupling from one area of a structure to another through the radiated fields complicates the analysis even further. Even with recent advancements in computing abilities, complete simulation of an array of elements is at best impractical<sup>4</sup>, leaving the approach of whole-structure simulation unsuitable for design purposes. As a consequence, several simplifications have been used to make the task of design a bit more tractable.

Kim *et al.* of Caltech simplified the fields problem by applying empirical intuition to guess at the RF models suitable for grid amplifier design. to the grid amplifier design [1, 5]. A later amplifier was designed by constructing several different grids, testing them, and selecting the arrangement with the best performance [2]. Though this approach successfully demonstrated that grid amplifier arrays can be built, a more rigorous approach became immediately necessary to begin to understand the physics of a grid amplifier.

Weikle proposed two approximations to reduce the complexity of the edge and coupling effects that plague grid amplifier analysis [4]. The first approxima-

---

<sup>4</sup>Simulation of a simple single element antenna radiating into free space requires approximately **eight hours** of simulation time on a PC running at 450MHz.

tion is to model the grid amplifier as an infinite plane array, leaving no edges. The second approximation is to design an array with periodic symmetry and then to assume it is illuminated with a plane wave. Figure 2.5 gives a view of a general array that fits the two assumptions here.

The symmetry of the grid allows electric (E) and magnetic (H) walls to be inserted as shown, reducing the analysis problem even further to a disturbance in a waveguide. The symmetry walls are placed as shown as a result of image currents, both electric and magnetic. To see this, consider a current source above a conducting plane where negative charge flows toward the conductor. The situation is equivalent to a mirror image of the current source below the conducting plane where positive charge flows toward it. But that is identical to an exact reflection of the current source across the conducting plane, preserving the direction and polarity of charge flow<sup>5</sup>. The same argument applies for magnetic charges. If the grid is illuminated by a plane wave, then the impressed currents will match the symmetry of the image charges giving the result shown in figure 2.5. Figure 2.6 shows the equivalent waveguide problem, allowing the grid amplifier to be modeled as a single unit cell.

Once the problem has been reduced to a disturbance in an equivalent waveguide, several analysis techniques can be used. Weikle proposed the use of an analysis technique that extracts the driving point impedance (and hence an equivalent circuit) of the metal structure as seen by a current source. This technique proceeds by assuming a current distribution on the metal patterns, deriving the fields excited by the current, and then calculating the total power in the fields and lost in the conductor using Poynting's theorem. The driving point impedance is then given by

$$Z_{dp} = -\frac{1}{I_0^2} \iint_{cell} \bar{E}_t \cdot \bar{J}_t dS.$$

$Z_{dp}$  is the parallel combination of the metal pattern impedance with the wave-

---

<sup>5</sup> Positive charge flow directed upward is identical to negative charge flow directed downward.

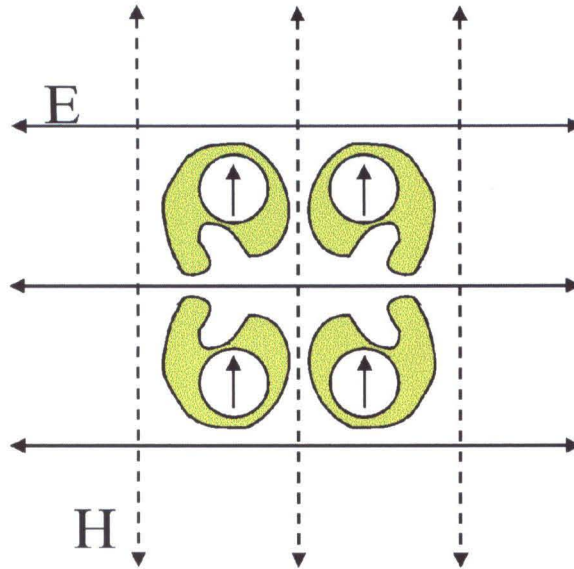


**Figure 2.5.** General metal pattern showing electric (E) and magnetic (H) symmetry planes.

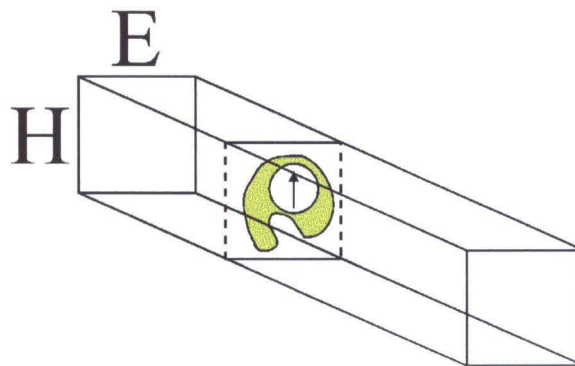


**Figure 2.6.** Equivalent waveguide model for the symmetric grid layout of figure 2.5.

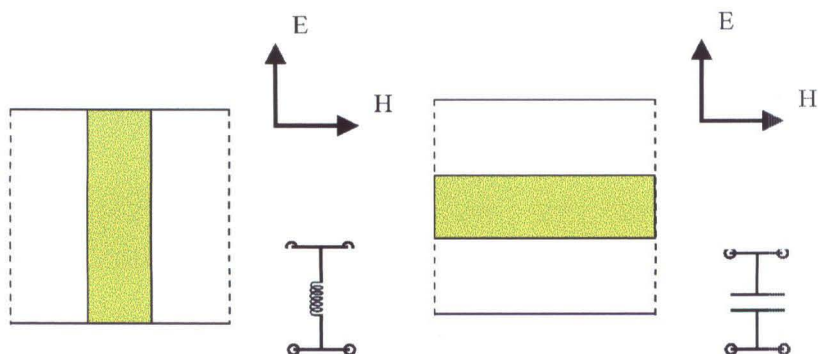


**Figure 2.7.** Inductive strip (a), and capacitive strip (b).

guide port impedance on either side [4].

One of the limiting factors on the accuracy of the EMF method is the precision with which the currents on the metal patterns can be assumed. De Lisio [3] extended the technique from assuming a uniform current distribution to allowing subdivisions of it into smaller strips (moments of currents). The technique estimates the relative amplitudes of the moment currents by setting the resulting electric field tangent to the metal equal to zero. Significant improvement was seen, and this analysis technique was used to design the grid amplifiers in [6, 7]. Figure 2.7 shows equivalent circuits that result from analyzing two metal patterns commonly used with grid amplifier designs.

Having found an equivalent circuit model for the metal patterns, all that remains of the electromagnetics problem is to analyze the dielectric sheets. Straightforward application of Maxwell's equations to a TEM waveguide filled with a uniform, isotropic dielectric material shows that the impedance of the waveguide is given by

$$Z_{TEM} = \frac{b}{a} \frac{\eta_0}{\sqrt{\epsilon_r}}$$

where  $b$  is the extent of the waveguide cross section parallel to the electric field,  $a$  is the extent of the waveguide parallel to the magnetic field,  $\eta_0$  is the impedance of vacuum, and  $\epsilon_r$  is the dielectric constant of the material.

After solving the electromagnetics of the problem for the various equivalent circuits, the remainder of the modeling can be done using a standard microwave circuit simulator. Figure 2.8(a) shows a grid amplifier circuit model. Measured device parameters can be inserted as general two-port models. Further simplification of the circuit is possible, however. Because the currents in the circuit are symmetric, a virtual ground may be placed at points in the circuit where the voltages go to zero. Figure 2.8(b) shows an equivalent single-ended circuit model that exploits the symmetry of the differential mode. Note that the impedances of the transmission lines in the single-ended circuit are half of those in the differential circuit. This results from modeling only half the unit cell giving an equivalent waveguide of half the cross section. The inductance  $L_g$  results from analysis of the grating pattern connected to the gates. Because the bias traces are parallel to the gate traces, they are modeled as inductors shunting the input;  $L_b$  models the bias traces.  $L_d$  models the drain leads. Polarizers are modeled as reactances backed by dielectric sheets. The input-side polarizer loads the output circuit inductively and the input capacitively. The reason is that the beam polarization changes by  $90^\circ$ , changing a capacitive strip to an inductive one, and vice versa.

The circuit of figure 2.8(b) has been used by De Lisio [7] and Liu [6] to successfully design grid amplifiers at X-band, Ka-band, and U-band. The measured performance of the amplifiers designed with 2.8(b) agreed reasonably well with the modeled performance, but the gains were lower than expected [8]. One reason for the discrepancy in the gain is that the various metal patterns on the grid amplifier were analyzed independently: the gate traces were analyzed without the source or drain leads present, and so on. The consequence is that parasitic coupling effects between the metal traces were ignored. Table 2.2 shows the significance of the coupling between the gate and the bias lines. As shown, without the parasitic coupling effects accounted for, the inductance of the gate with the

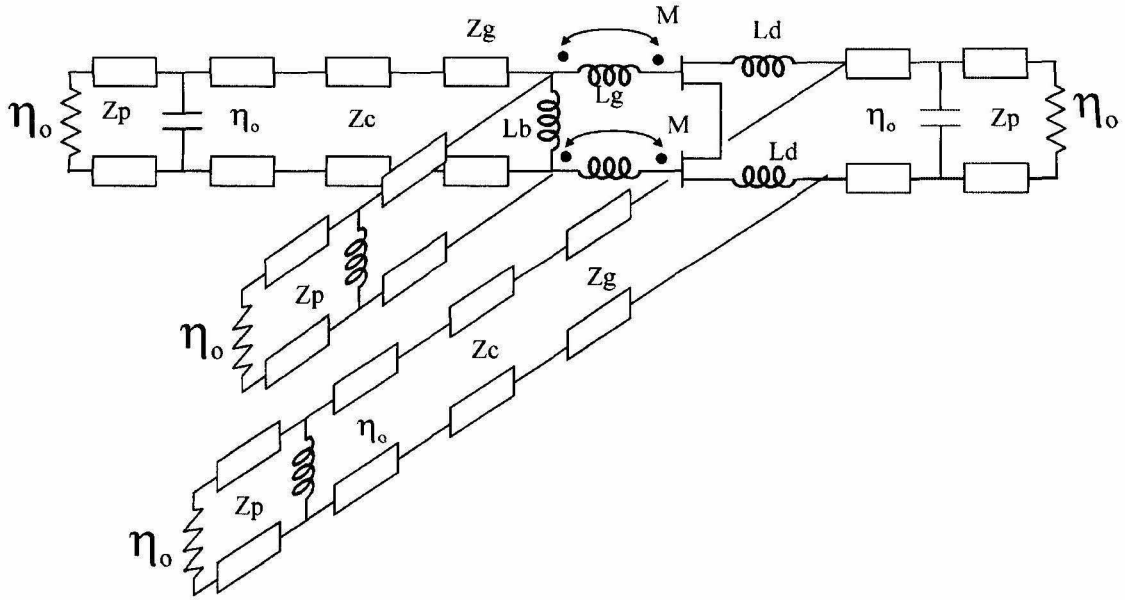


**Figure 2.8a.** Complete circuit model for the symmetric grid amplifier.  $Z_p$  is the impedance of the polarizer substrate,  $\eta_o$  is the impedance of vacuum,  $Z_g$  is the impedance of GaAs. Polarizers are shown as either a capacitance or inductance, depending on the polarization: the input-side polarizer loads the output inductively and the input capacitively.

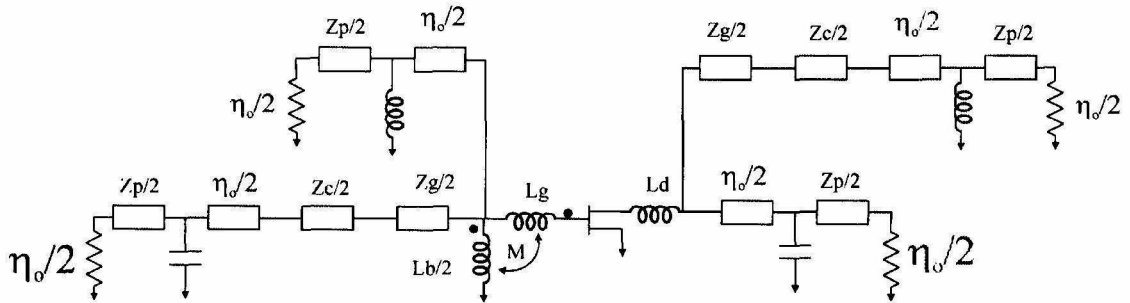


**Figure 2.8b.** Half circuit model taking advantage of the differential symmetry of the original circuit. All impedances get divided by 2.

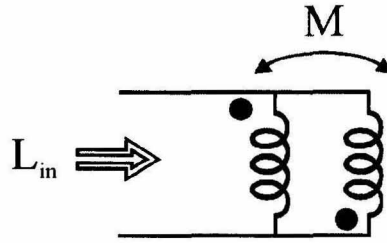


**Figure 2.9.** Parallel combination of gate and bias metal traces used to find the mutual inductance.

bias is significantly higher.

The procedure to find the mutual inductance between the gate and the bias is to analyze the two patterns independently, and then analyze them together. With reference to figure 2.9, the mutual inductance between the gate and bias traces is given by

$$L_{eff} = \frac{L_1 L_2 - M^2}{L_1 + L_2 + 2M}$$

where  $L_1$  is the inductance of the bias,  $L_2$  the inductance of the gate lead, and  $L_{eff}$  the inductance of the two in parallel. The circuit of figure 2.8 with the mutual inductance included has been used to predict the gain of grid amplifiers to better than 0.5 dB [8, 9]. Parasitic capacitive coupling effects may also be calculated in a similar manner, but they are usually much less significant than the inductive coupling effects and are thus ignored.

Metal Pattern	Circuit Model	Element Value
Gate		126 pH
Bias		27 pH
Uncoupled		22 pH
Coupled		17.4 pH

**Table 2.2.** Various metal patterns and their inductances. Ignoring the mutual inductance between the gate and the bias causes more than a 25% difference in the combined inductance.

### 2.2.2 FULL ELECTROMAGNETIC MODEL

The modeling of the previous section approaches the electromagnetics by modeling the metal patterns on the grid amplifier as lumped capacitances or inductances, with various coupling effects included. Another approach is to analyze the unit-cell directly to generate a three-port scattering matrix for it. The resulting matrix can be then used with a circuit simulator to design the amplifier. Preventza *et al.* have developed a model based on HFSS simulations of the unit cell.

Consider the layout of figure 2.10. Here half the unit cell is analyzed, so that the resulting scattering matrix can be used directly with a circuit similar to that of figure 2.8(b). Port 3 in figure 2.10 is the location where the gate of the transistor will be connected, but defining a port there destroys the symmetry of the layout during simulation. A full three-port scattering matrix can, however, still be found by performing various two-port simulations with the third port terminated in some known load. Noting that the three-port device is reciprocal at the third port ( $S_{31} = S_{13}$  and so forth), its matrix has the form

$$\begin{pmatrix} S_{11} & S_{12} & S_{13} \\ S_{21} & S_{22} & S_{23} \\ S_{13} & S_{23} & S_{33} \end{pmatrix}.$$

$S_{13}$ ,  $S_{23}$ , and  $S_{33}$  can be treated as three unknowns for which three equations are necessary. To generate the three equations, port three is terminated in various known loads (a short, a known resistance, and an open are the most convenient) and two-port scattering matrices are generated by direct simulation with HFSS. The unknowns are then given by [8]

$$S_{33} = \frac{S_{21s} + S_{21o} - 2S_{21r}}{S_{21o} - S_{21s}}$$

$$S_{13} = \sqrt{(S_{11r} - S_{11s})(1 + S_{33})}$$

$$S_{23} = \sqrt{(S_{22r} - S_{22s})(1 + S_{33})}$$

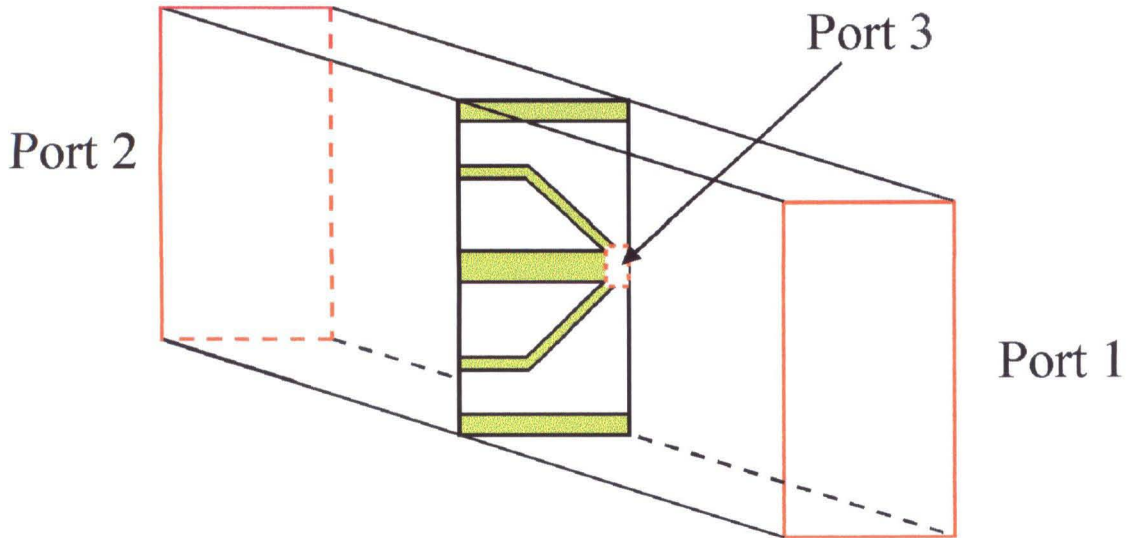


**Figure 2.10.** Layout for the direct E&M model of the unit cell. GaAs and the chip carrier are usually added.

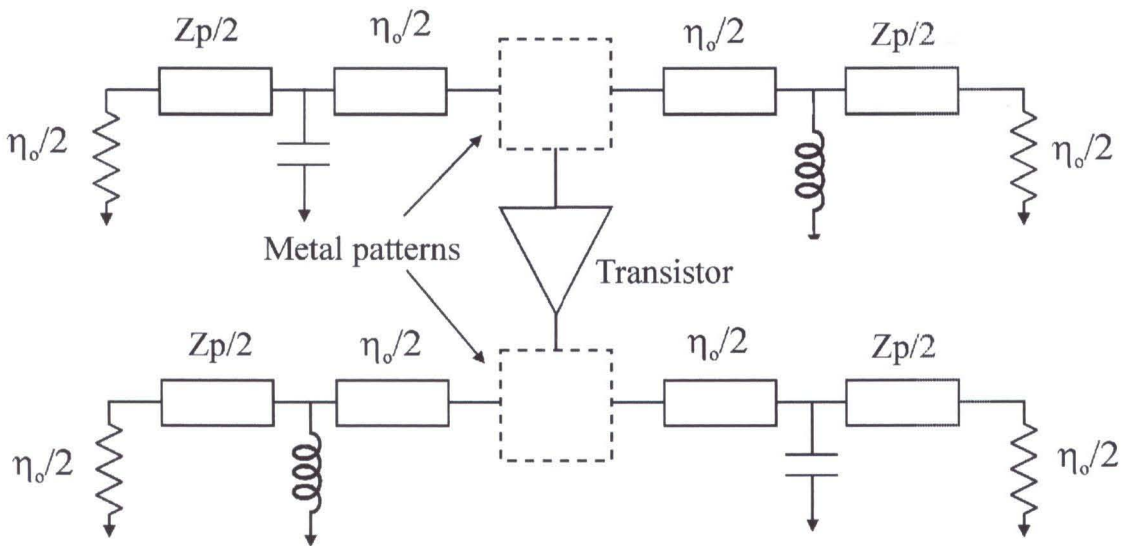


**Figure 2.11.** Circuit model resulting from the full E&M approach.

where the subscripts “s,” “o,” and “r” correspond to two-port simulations with the third port shorted, open and resistively terminated, respectively. Because the output polarization is perpendicular to the input, this procedure is followed for each polarization. The result is two three-port models for the unit cell metal patterns that can be used directly in a circuit simulator. Figure 2.11 shows the circuit model used in [8] to predict the gain of an X-band grid within .5 dB.

The drawback of using this technique is that it is simulation intensive. Six simulations need to be performed on the same unit cell over a broad range of frequencies<sup>6</sup>. The lumped-element approach requires four simpler simulations, and because the lumped element values are quite stable with frequency, only one frequency point is necessary. As a consequence, then, the lumped-element model is used throughout.

### 2.3 UNIT CELL DESIGN

Figure 2.12 shows a photograph of the unit cell layout; the grid amplifier consists of a 16 by 16 array of such unit cells. There are three important issues

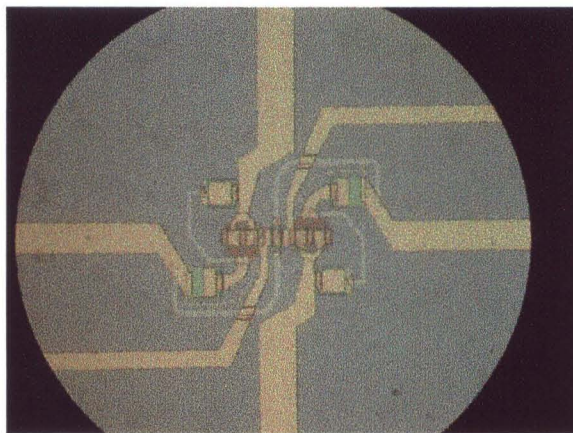


**Figure 2.12.** Photograph of the fabricated unit cell.

<sup>6</sup> S parameters are needed at every frequency point used in the circuit model. Though most simulators are capable of interpolating, a large number of frequency points is still required, resulting in very long simulation times for this technique.

to address when selecting a layout. The first is the shunt RF reactance the bias lines present to the input beam, the second is the DC resistance of the traces, and the third is how to pass the gate bias voltage from cell to cell.

A meander line has been successfully used in the design of previous grid amplifiers; figure 2.13(a) shows a sketch of its design [5, 7, 6]. Kim shows the reactance of the meander line to be approximately twice that of a flat line [5], reasonably independent of frequency. Another approach was proposed by Liu [1] to design a resonant pattern into the bias lines, giving very high reactance. Figure 2.13(b) shows the layout of the design, and Liu showed the design to have a sharp resonance so that the shunting effects of the bias could be completely removed [10]. For smaller grids, both bias line designs have been used successfully. For a large grid with 16 cells (32 transistors) on a side, the required line length for both designs introduced prohibitive DC resistance. The resonant structure had the additional drawback of its very sharp resonance so that the bandwidth would be limited.

Each transistor in the array operates with approximately 20 mA of current, giving 320 mA of current from each side of the grid (bias connections are made from both sides of the array to distribute the bias current). The resistance in the gold traces causes a voltage drop along the bias lines. The voltage difference between the cells on the edges of the array and those in the center is given by  $\Delta V = I_0 R/2$ , where  $I_0$  is the net current for half of the devices connected to a particular bias line<sup>7</sup>, and  $R$  is the resistance of half the length of a bias line. For a meander line suitable for the large grid design (figure 2.13 (a)), assuming a gold conductivity of  $2 \cdot 10^7$  S/m<sup>8</sup>, the DC resistance of the meander line would be about  $21\Omega$ , leading to a voltage drop to the center of the grid of 1.7 V. Because the transistors operate between 2 and 3 volts drain-to-source, a 1.7 V drop in the

---

<sup>7</sup> Bias connection is made from both sides of the grid so that half the bias current flows from the sides of the lines toward the center of the grid.

<sup>8</sup> The tabulated conductivity of gold is about  $4 \cdot 10^7$ , but plated gold has about half that value.

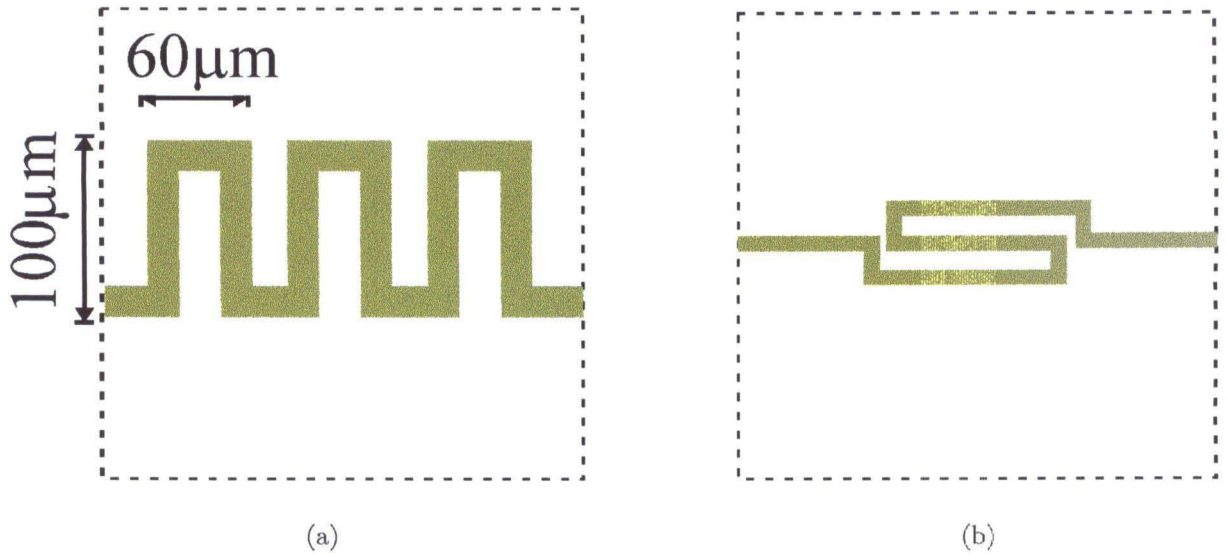


**Figure 2.13.** Various bias line layouts. Meander line (a) and hairpin line (b). Both lines are approximately  $2\mu\text{m}$  thick. The line width is  $20\mu\text{m}$ .

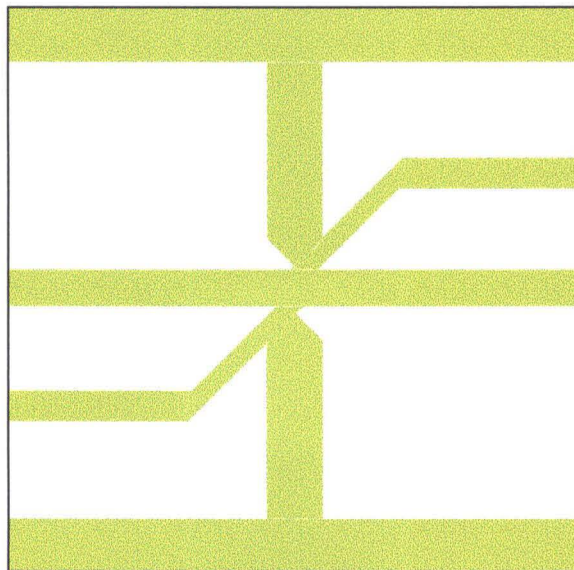


**Figure 2.14.** Metal pattern layout. The transistor pair is placed in the center of the layout.

bias would ensure that the grid would be the world's most expensive heater. But the problem is compounded by the source current: the same current flows in the source bias lines, but in the *opposite* direction. The result is that the devices in the center of the grid (most of the transistors in the array) would have a bias of nearly 0 V drain-to-source, and the few edge devices would have nearly 3 V drain-to-source.

To mitigate the bias drop problem, a flat bias line design was chosen. The reactance of that line dropped by a factor of 2 from the meander line (from  $j31\Omega$  to  $j15\Omega$ ) but the DC resistance dropped by a factor of 3. Increasing the thickness of the line a little (to about  $5\mu\text{m}$ ), the voltage drop reduced to about .5 V on the drain line. With an equal source drop, the worst case bias for the transistors near the center of the grid would have a drain-source bias of at least 2 V.

Previous grid amplifiers have used symmetric source bias lines with respect to half the unit cell: there were two source bias lines per cell instead of one. The additional bias line decreases the RF shunt reactance presented to the input beam, and thereby lowers the bandwidth of the amplifier. Simulations predict a bandwidth of about 3% with symmetric lines, and greater than 10% with the shown asymmetric line. A grid with symmetric bias lines was also designed on the same lot.

With reference to figure 2.15, the gate bias voltage needs to pass from one gate in a cell, under an electric symmetry plane, to the gate of the second device in the cell. The electric symmetry plane in the center of the cell provides a virtual ground, so that a direct metal connection would short the input signal. Since the DC input impedance of a pHEMT should be huge, on the order of mega-ohms, the gates should draw truly negligible DC current, so that a resistor could pass the bias from gate to gate without voltage drops. Provided that the value of such a resistor remains high compared to the RF input resistance of the transistor, its RF shunting effects will be small, so that negligible RF power is

lost. This approach has been used on previous  $p$ HEMT grid amplifier designs with satisfying results [3, 10], and the technique was selected here for the larger grid.

## 2.4 STABILITY

Though the grid amplifier unit cell is designed to operate differentially, previous grid amplifier arrays have shown common mode oscillations. As a consequence, stability analysis of the grid amplifier examines both common and differential modes of operation. Differential mode oscillations over the grid amplifier excite the same current patterns in the gate and drain leads as would an incident beam amplified by a stable grid. Figure 2.16(a) shows the current patterns for differential mode oscillations, and the excited fields radiate into space normal to the grid amplifier surface. Common mode oscillations were observed by Liu [11] and excite current patterns that cause radiation into the substrate and lead to electric symmetry around the unit cell of the grid amplifier, as shown in 2.16(b). Two different circuit models are used to ensure the stability of the

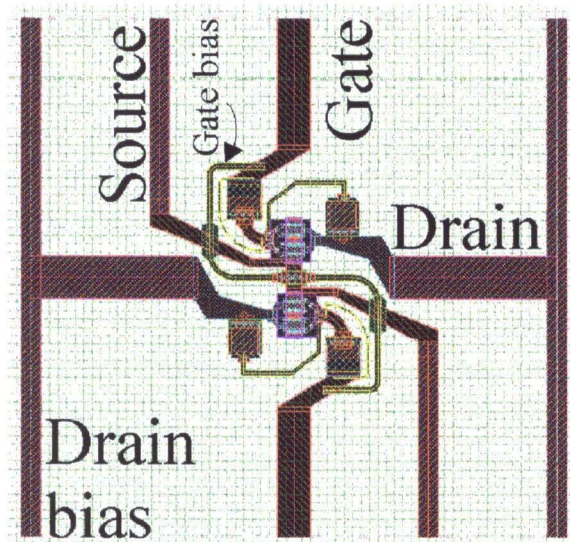


**Figure 2.15.** Unit cell layout. The long, yellow trace is the gate bias resistor. The capacitors in the gate leads are for input matching. An RC feedback network is used for stabilization.

grid amplifier.

Because of the symmetry of the current patterns in the differential mode oscillations, stability analysis can use the circuit model of figure 2.8(b) and apply well-known two-port stability theory<sup>9</sup>. With reference to figure 2.17, the two-port is unconditionally stable at a given frequency when  $\Gamma_{in} < 1$  and  $\Gamma_{out} < 1$ , where

$$\Gamma_{in} = S_{11} + \frac{S_{12}S_{21}\Gamma_L}{1 - S_{22}\Gamma_L}$$

$$\Gamma_{out} = S_{22} + \frac{S_{12}S_{21}\Gamma_S}{1 - S_{11}\Gamma_S}$$

Clearly,  $\Gamma_{in}$  is a function of the load reflection coefficient,  $\Gamma_L$ , and  $\Gamma_{out}$  is a function of the source reflection coefficient,  $\Gamma_S$ . A two port device is conditionally stable (or potentially unstable) if for some load or source reflection coefficients  $\Gamma_{in}$  or  $\Gamma_{out}$  can equal or exceed 1. The two-port is unconditionally stable if for no (passive) load or source reflection coefficients can either  $\Gamma_{in}$  or  $\Gamma_{out}$  equal or exceed unity. Tuning of the grid amplifier is done by translating the polarizers along the output beam's axis of propagation until the gain performance is optimized. But translating the polarizers causes the source and load reflection coefficients to vary widely, so that a potentially unstable transistor may be induced to oscillate. To prevent instabilities during tuning, the transistors were compensated so that they are unconditionally stable for all passive load and source reflection coefficients. This is equivalent to the simultaneous satisfaction of the following [12]:

$$K > 1$$

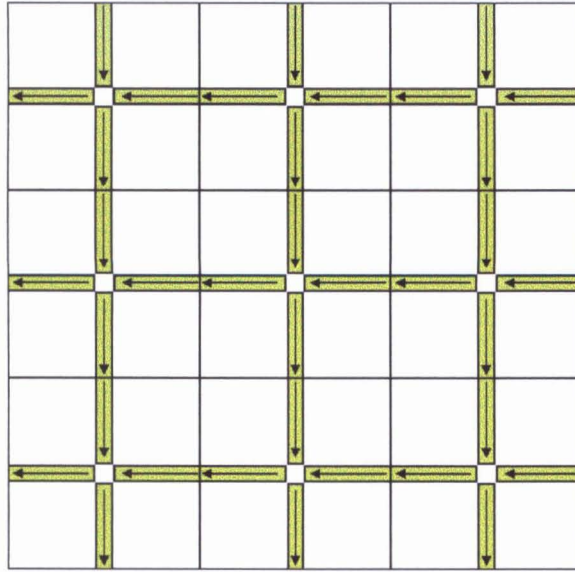
$$\Delta < 1$$

$$\Delta = S_{11}S_{22} - S_{12}S_{21}$$

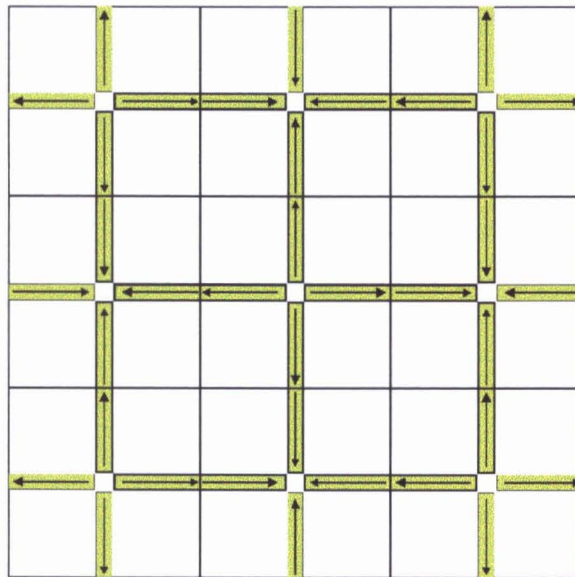
$$K = \frac{1 - |S_{11}|^2 - |S_{22}|^2 + |\Delta|^2}{2|S_{12}S_{21}|}$$

---

<sup>9</sup>Two-port stability theory is dealt with in nearly every microwave book available. Gonzalez gives a clear and simple treatment of the subject in [12].

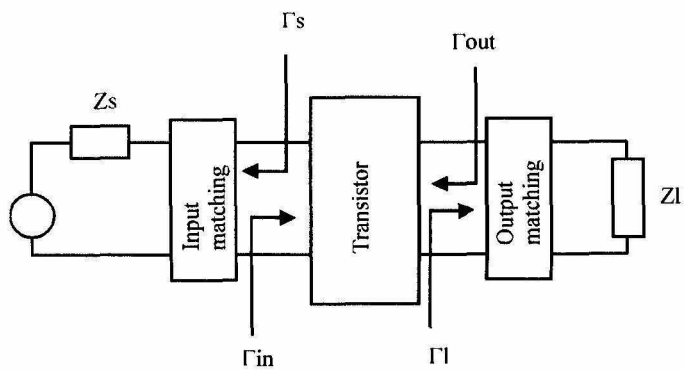


(a)

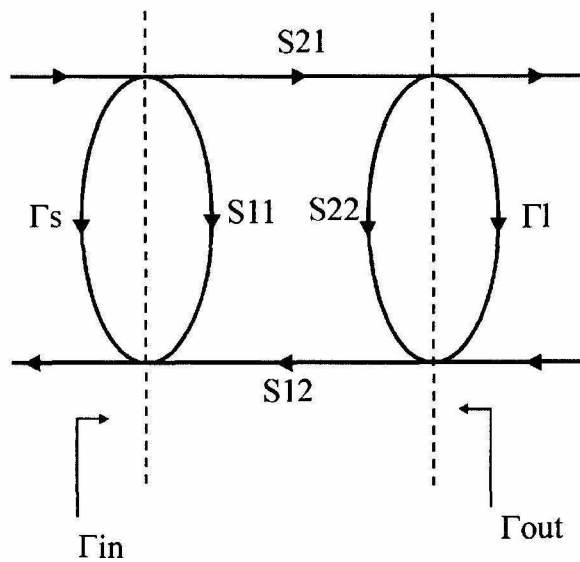


(b)

**Figure 2.16.** Currents excited by a differential mode oscillation (a) and by a common mode oscillation (b). Common mode oscillations result in electric boundaries at the cell walls, and the fields radiate into the substrate.



(a)

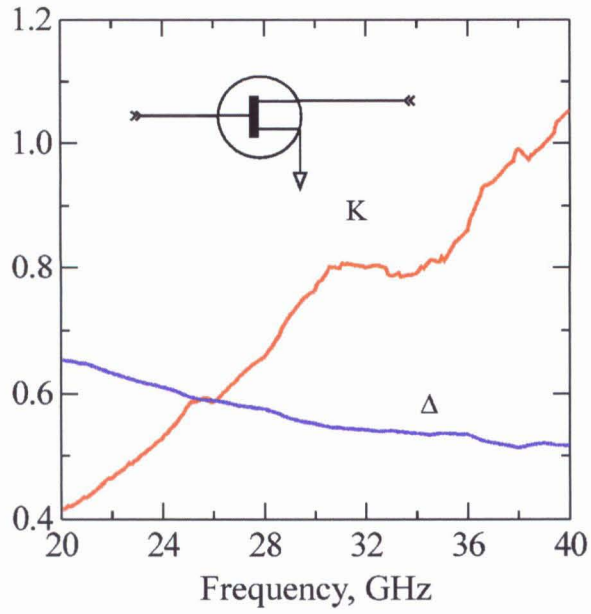


(b)

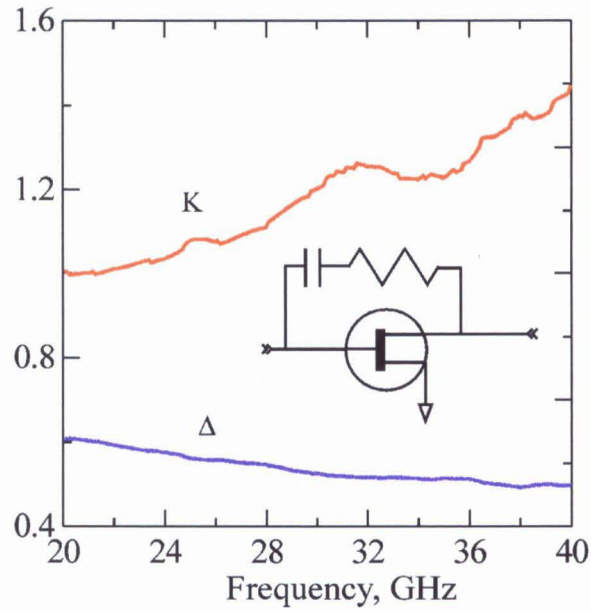
**Figure 2.17.** General two-port circuit layout (a). Signal flow graph for the network (b).

Figure 2.18(a) shows plots of  $K$  and  $\Delta$  for the devices used in the grid amplifier design. As shown, the device is potentially unstable over the entire range of interest, so that some source or load reflection coefficients may cause oscillations. Adding resistive feedback from drain to source (and using a large-valued capacitor to protect the bias) improves the stability. Adding a  $1245\text{-}\Omega$  resistor makes the device unconditionally stable so that no polarizer position can cause oscillations during tuning. Figure 2.18(b) shows plots for  $K$  and  $\Delta$  with the RC feedback network added. Once the device has been stabilized unconditionally, a simultaneous conjugate match at the input and output is possible to maximize the gain and minimize reflection losses.

Common mode oscillations require a different model for stability. Liu *et al.* at Caltech developed a stability model for the common mode oscillations that follows the design of oscillators [11]. The symmetry of the currents excited by the common mode oscillation imposes electric wall boundary conditions on the unit cell. Radiation of the oscillating fields is into the substrate, so the unit cell is loaded by its walls, which are here short circuits. Since the fields are guided by the substrate, the input and output traces connected to the gates and drains of the transistors appear as transmission lines in the circuit model. Figure 2.19(a) shows the circuit model that results from the current symmetry in 2.16(b). Since the unit cell is surrounded by electric walls, the cell can be treated with quarter-cell symmetry. The stability model operates on one quarter of the cell, so the active device is now “half” of a transistor. To derive the parameters for the “half” transistor, the Y parameters for the full transistor are divided by two. A complete treatment of the technique is given in [10]. The analysis determines the loop gain of the amplifier as seen by the input. The amplifier will be stable for a loop gain less than unity at  $0^\circ$  or  $180^\circ$  phase shift (this is basically the Nyquist criterion for stability). The circulator in the circuit model is used to track the loop gain. Figure 2.19(b) shows the Smith chart plot of the circulator



(a)



(b)

**Figure 2.18.** Stability factors for the transistor without compensation (a), and with compensation (b). As shown, the compensated transistor is unconditionally stable across the whole band of interest.

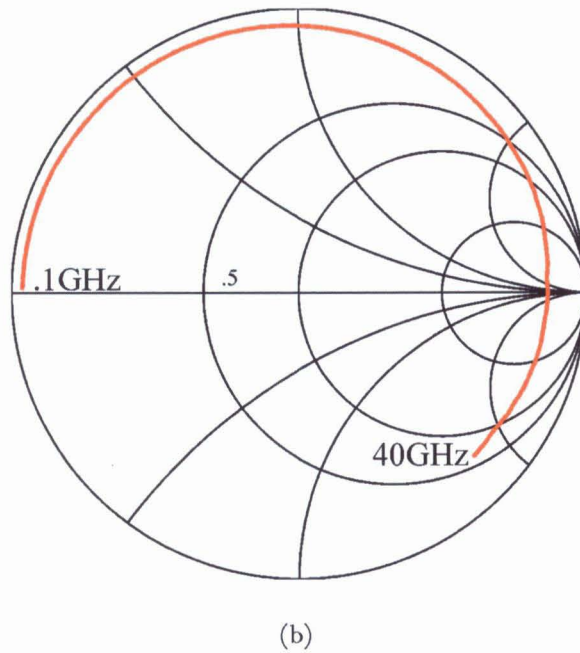
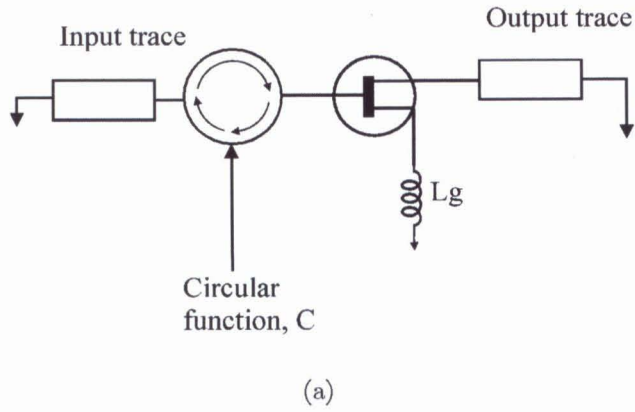


**Figure 2.19.** Circuit model used for the common mode stability analysis (a). The inductor in the source lead models the short metal trace that connects to the virtual ground in the center of the unit cell. In the analysis here it is neglected because it is so short: less than  $20\ \mu\text{m}$ . The circulator function shows the loop gain in (b). As shown, the device is stable over the entire range of interest.

function. As shown in the plot, the loop gain is always less than unity, so the amplifier should be stable in the common mode. It should be noted that this is an empirical theory in the sense that the transmission line values are set to match an observed oscillation. For design, then, the procedure is to sweep the values of the line impedance and electrical length across a sufficiently wide range as to subsume what may be physical. In this case, the impedance values of the lines were swept from nearly 0 to 1000  $\Omega$  to watch for possible oscillations. In all cases the amplifier was seen to be stable.

## 2.5 FIRST GRID PERFORMANCE

The performance of the first grid was less than satisfying. Though no oscillations were observed, the likely explanation was disappointing. Figure 2.20 shows that gain of the grid amplifier was measured at slightly above 1dB. To investigate the performance of the grid, DC measurements were made at each unit cell across the grid to verify the bias distribution. Figure 2.21(a) shows a DC

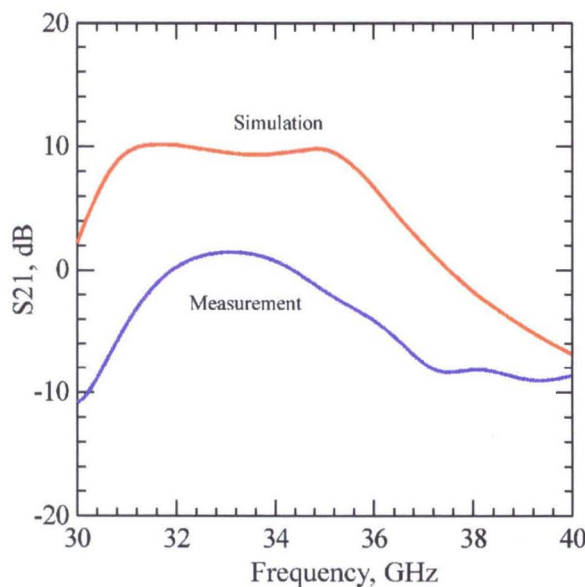


**Figure 2.20.** Measured and simulated performance of the first iteration grid amplifier. Device leakage causes poor bias distribution and poor performance.

probe measurement of the gate voltages over several rows of the grid amplifier, and 2.21(b) shows the drain-source voltages of several rows. As the figures show, the bias profile of the grid prevented most of the devices from even turning on. Measurements of the gate voltage shows significant changes from the center of the grid to the edges. Since the gate voltage is passed from cell to cell via a high valued resistor, a small amount of current from a leaky device can change the voltage at each gate toward the edge from it. But the slope of the gate voltage curve changes at each cell; the shape is parabolic, concave down. Such a shape indicates that *each* transistor in the entire row leaks current onto the gate line. To verify the leakage, discrete transistors from the same lot as the fabricated grid were biased and tested for leakage. A *p*HEMT should, under normal DC bias conditions, show very little (less than  $1\mu\text{A}$ ) leakage. Figure 2.22 shows a scatter plot of the leakages of various discrete transistors. As shown, the leakage varies widely from less than  $1\mu\text{A}$  to more than  $25\mu\text{A}$ . An average is difficult to derive from the measurements, but approximately  $5\mu\text{A}$  is shown to be a realistic guess from the data. Figure 2.23(a) shows a DC leakage model for the gates of the grid amplifier, and using  $5\mu\text{A}$  as the current source value, the simulated profile in figure 2.23(b) results.

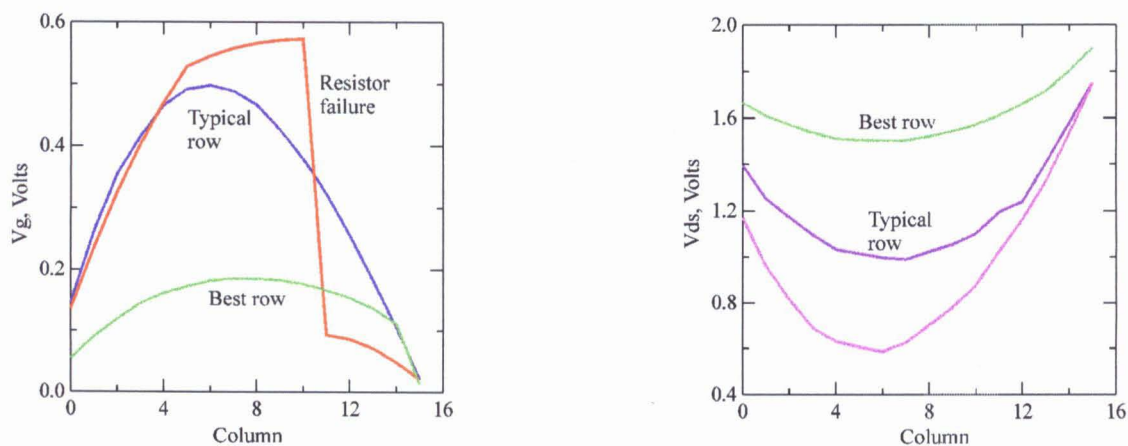


**Figure 2.21.** (a) Measured gate voltage, (b) measured  $V_{ds}$  profile.

Another cause of the poor performance of the first grid amplifier may be resistor failure. The gate resistor is fabricated with nichrome, and is long. Adhesion trouble caused numerous resistors to fail. Each row of the grid can tolerate one resistor failure, since the bias is connected at both sides of the grid. But two failures would cut the bias from all devices in between the failures on a row.

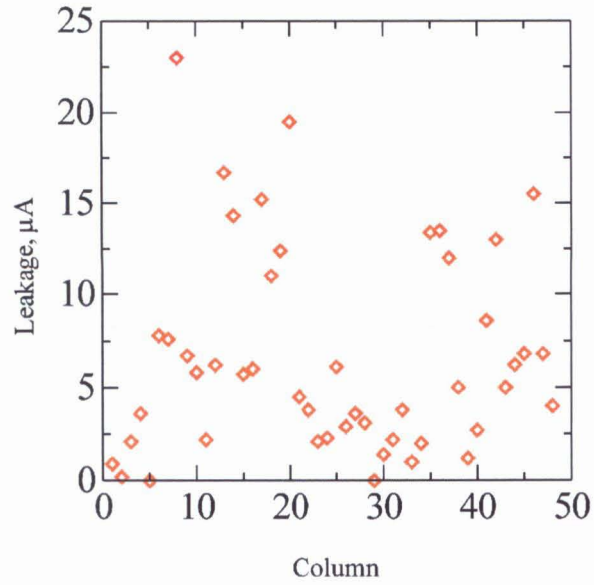


**Figure 2.22.** Measured leakage data for discrete transistors. The leakage should be less than  $1\mu\text{A}$ . The worst device showed  $45\mu\text{A}$ .

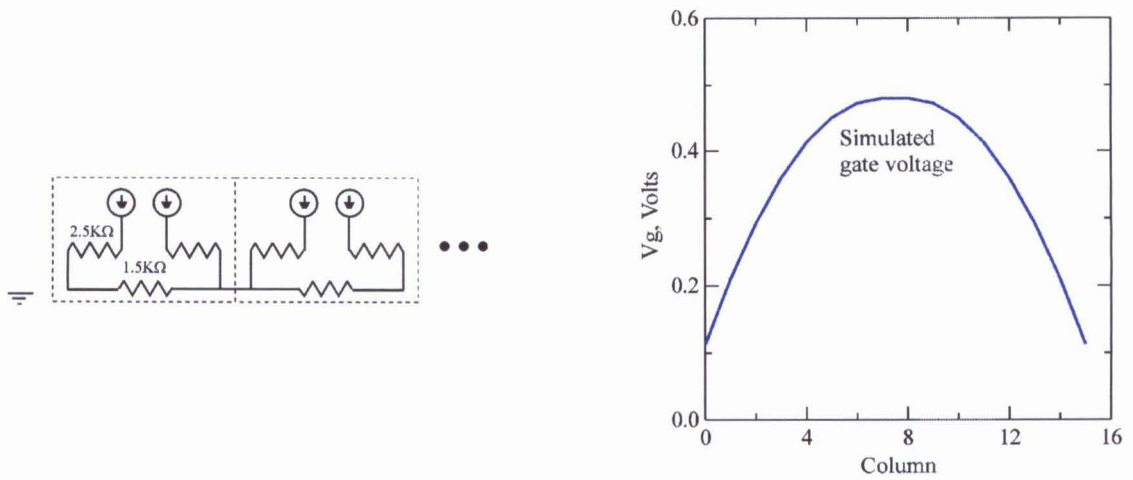


**Figure 2.23.** DC model of the unit cell. The current source supplies  $5\mu\text{A}$  of current. The plot shows the gate voltage derived from the DC model.

### References

- [1] M. Kim, J.J. Rosenberg, R.P. Smith, R.M. Weikle, J.B. Hacker, M.P. DeLisio, D.B. Rutledge, "A grid Amplifier," *IEEE Microwave Guided Wave Letters*, vol. 1, pp. 322-324, November, 1991.
- [2] M. Kim, E.A. Sovero, J.B. Hacker, M.P. De Lisio, J.C. Chiao, S.J. Li, D.R. Gagnon, J.J. Rosenberg, D.B. Rugledge, "A 100-Element HBT Grid Amplifier," *IEEE Trans. Microwave Theory Tech.*, vol. 41, pp. 1762-1771, October, 1993.
- [3] M.P. De Lisio, "Hybrid and Monolithic Active Quasi-Optical Grids," Ph.D. Thesis, California Institute of Technology, Pasadena, Ca., 1996.
- [4] R.M. Weikle, "Quasi-Optical Planar Grids for Microwave and Millimeter-Wave Power Combining," Ph.D. Thesis, California Institute of Technology, Pasadena, Ca., 1992.
- [5] M. Kim, "Grid Amplifiers," Ph.D. Thesis, California Institute of Technology, Pasadena, Ca., 1993.
- [6] C.M. Liu, E.A. Sovero, W.J. Ho, J.A. Higgins, M.P. De Lisio, D.B. Rutledge, "Monolithic 40-GHz 670-mW HBT Grid Amplifier," *IEEE International Microwave Symposium Diag.*, pp. 1123-1126, 1996.
- [7] M.P. De Lisio, S.W. Duncan, D.W. Tu, S. Weinreb, C.M. Liu, D.B. Rutledge, "A 44-60 GHz Monolithic pHEMT Grid Amplifier," *IEEE International Microwave Symposium Diag.*, pp. 1127-1130, 1996.
- [8] P. Preventza, B. Dickman, E. Sovero, M.P. De Lisio, J.J. Rosenberg, D.B. Rutledge, "Modeling of Quasi-Optical Arrays," *IEEE International Microwave Symposium Diag.*, pp. 563-566, June, 1999.
- [9] B. Dickman, E. Sovero, D. Deakin, D. Rutledge, "A 5-Watt Ka-Band Grid Amplifier," *To be published in the 2000 IEEE International Microwave Symposium Digest.*

- [10] Cheh-Ming Jeff Liu, "Monolithic Grid Amplifiers," Ph.D. Thesis, California Institute of Technology, Pasadena, Ca., 1993.
- [11] C.M. Liu, E.A. Sovero, M.P. De Lisio, A. Moussessian, J.J. Rosenberg, D.B. Rutledge, "Gain and Stability Models for HBT Grid Amplifiers," *IEEE AP-S Int. Symp. Dig*, pp. 1292-1295, 1995.
- [12] G. Gonzalez, "Microwave Transistor Amplifiers," second edition, Prentice Hall, Upper Saddle River, New Jersey, 1997.

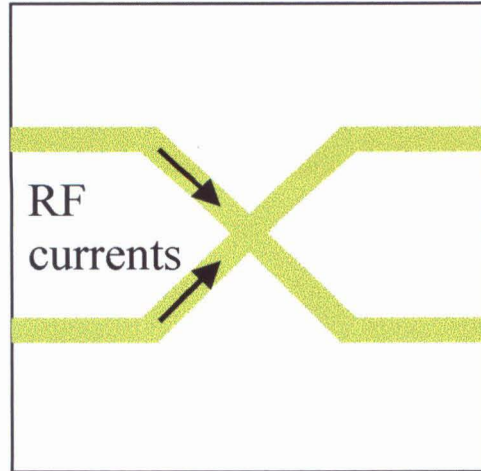
## Chapter 3

# High-Power Design And Performance

Three significant problems with the first fabrication of the grid amplifier were gate current leakage, bias line drops, and resistor failure. To address these issues, two options were designed onto a common pattern for the second fabrication mask set. The common pattern moves all of the resistors in the layout to the epitaxial layer. Epitaxial resistors are fabricated by selectively doping areas of the substrate to locally alter its conductivity. Use of epi-layer resistors solves the adhesion problem that caused resistor failures on the first grid. The common mask pattern also overlays an extra metal deposition to the bias lines to thicken them, decreasing the DC resistance associated with them.

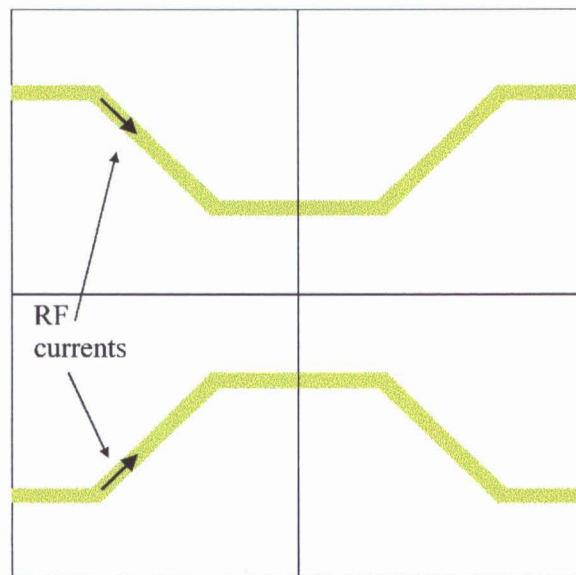
The first option to modify the common pattern is to add a second source bias line to the unit cell restoring the symmetry used in previous designs. There are two reasons for this addition. The first is the plain DC advantage the second bias line adds: the DC resistance of the source bias lines drops by two. The second reason is that the symmetric source lines should be coupled reasonably tightly. As such, any RF currents that may be excited in the diagonal sections of the lines should interfere destructively and eliminate a possible feedback path. RF currents excited in the asymmetric source line would have to couple to a source line in a neighboring cell, resulting in much weaker interference. The result may lead to instabilities. Figure 3.1 shows a schematic of the two mechanisms.

The second option to the common pattern is a self-bias short in the gate of



(a)

**Figure 3.1a.** Vertical components of RF currents excited in the source bias lines interfere destructively when the lines are close together, and hence tightly coupled.



(b)

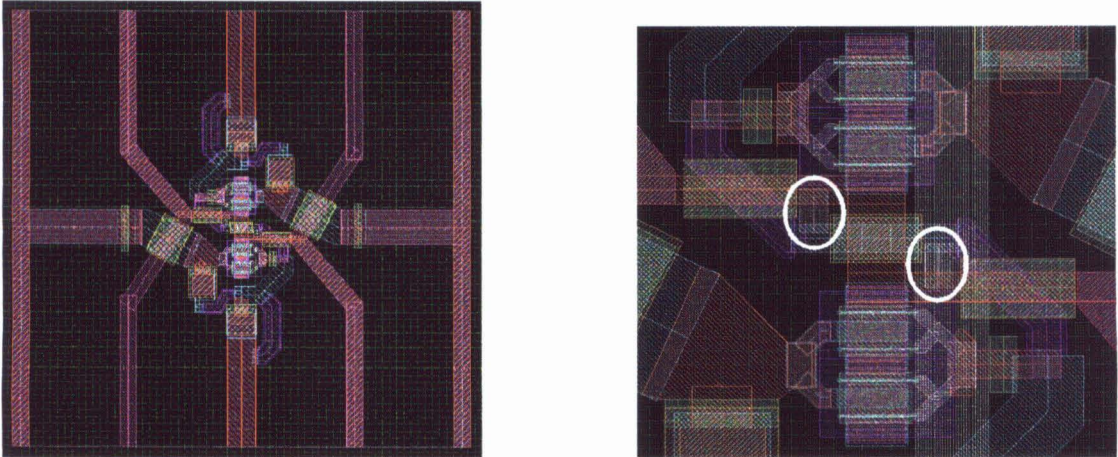
**Figure 3.1b.** Vertical components of RF currents excited in the source bias lines may not interfere as strongly with the asymmetric bias line design.

the transistors. With reference to figure 3.2, the gate resistor passes under the source line in the center of the unit cell where there is a virtual ground. Shorting the resistor to the source at that point has no effect on the AC performance, but provides a path for leakage current in the gate directly to ground. The only voltage drop that can result from gate current leakage is reduced to a single voltage drop at the gate of the leaky transistor. The gate resistor's value to ground is  $1.25\text{ k}\Omega$ , and the average leakage is about  $5\mu\text{A}$ , so the drop should be less than  $10\text{ mV}$ . It turned out that optimal power performance of these transistors requires a gate-source voltage of about  $-0.3\text{ V}$ , so this self bias idea was abandoned for a grid that showed excellent DC performance.

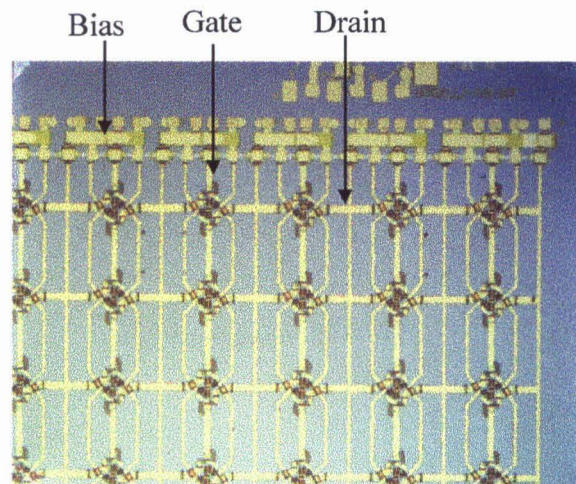
### 3.1 SUCCESSFUL GRID AMPLIFIER

Figure 3.3 shows a photograph of a corner of the successful grid amplifier. Of the 512 transistors on the grid, all were operational. The gate leakage current for the entire grid running at full bias was less than  $1\text{ mA}$ , giving an average single transistor leakage of about  $1\mu\text{A}$ . Modeling of the structure is after [2.8], and uses the circuit of figure 2.8(b), adding an RC network at the input for matching. Figure 3.4 shows the complete circuit model.

Figure 3.5 shows geometries used with Ansoft's HFSS program to analyze the bias lines and the coupling between them and the gate. Scattering parameters direct from HFSS are plotted against circuit model data in figures 3.6 - 3.8. Figure 3.9 shows the small-signal performance of the grid amplifier. The symmetric bias lines limit the bandwidth by virtue of the lower RF inductance. The theory curve uses device parameters measured from discrete devices fabricated on the wafer from which the working grid was taken. In the measured circuit, the input side polarizer is closer than the theory would suggest. This is most likely due to variance across the grid amplifier and difference between modeled and fabricated circuit values. Because the shunt inductance modeling the polarizers is designed to be quite low, errors in its actual inductance are not surprising.



**Figure 3.2.** Layout of the second grid amplifier. The self-bias option is circled in the zoom. Because optimal power performance is achieved with a gate-source voltage of  $-3\text{ V}$ , and a grid with excellent DC performance was found, the self-bias option was not used.



**Figure 3.3.** Photograph of the fabricated grid.

Electromagnetic analysis of the polarizer structure suggests a  $j10\ \Omega$  impedance, while measurements of the grid amplifier suggest its value to be  $j13\ \Omega$ . The modeling assumes the value  $j13\ \Omega$ .

Figure 3.10 shows the power and gain performance of the amplifier. As shown, the gain at 5 W output is 5 dB. Figure 3.11 shows the efficiencies of the amplifier. At 5 W of output power, the power-added efficiency is 17%. The previous Ka band amplifier fabricated with HBTs showed a PAE of 4% at an output level of 670 mW. Figure 3.12 shows an estimate of the combination efficiency of the grid. The data shows an estimate in the sense that the curve showing the single device performance was measured under load pull conditions at 39 GHz. The grid amplifier data is, clearly, an amplifier measurement without load pull tuners at 37.2 GHz. But the grid amplifier uses devices that are feedback compensated for stability, and hence have lower gain than discrete devices, so the power performance is expected to be lower. No load pull measurements have been made on discrete devices with feedback at 37.2 GHz, so the shown plot gives the best estimate currently available.

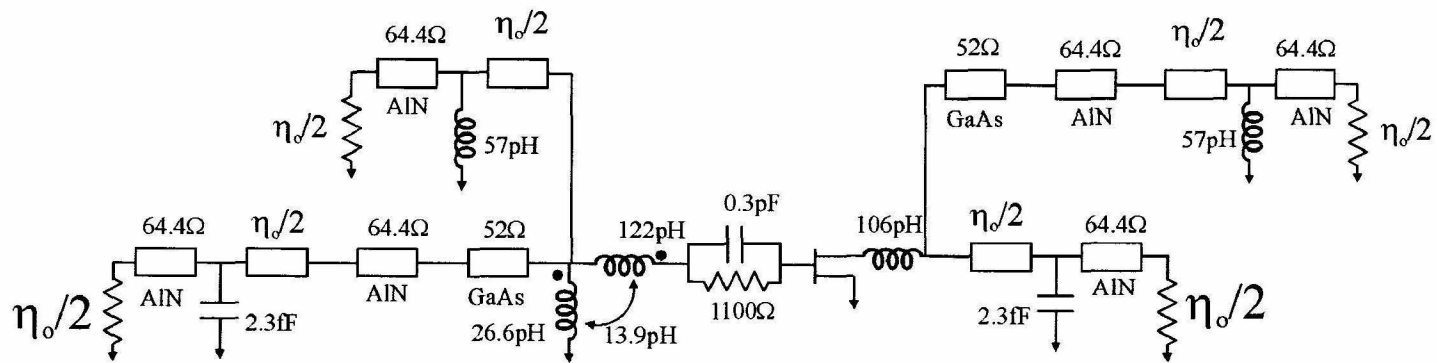


**Figure 3.4.** Circuit model for the grid amplifier with symmetric bias lines.

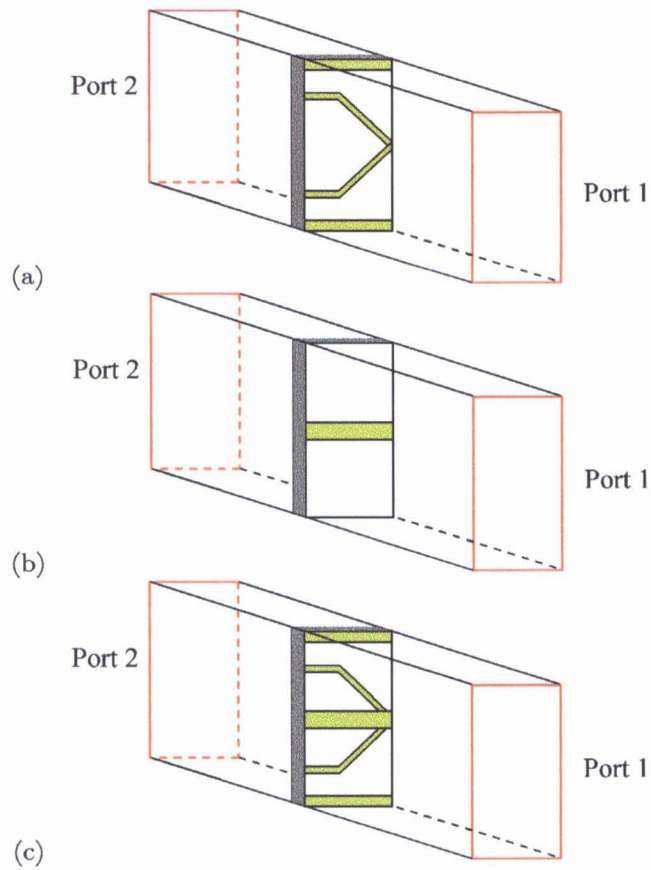
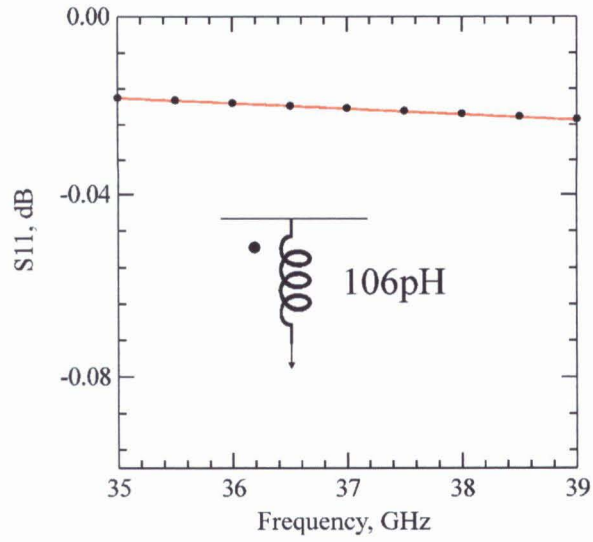
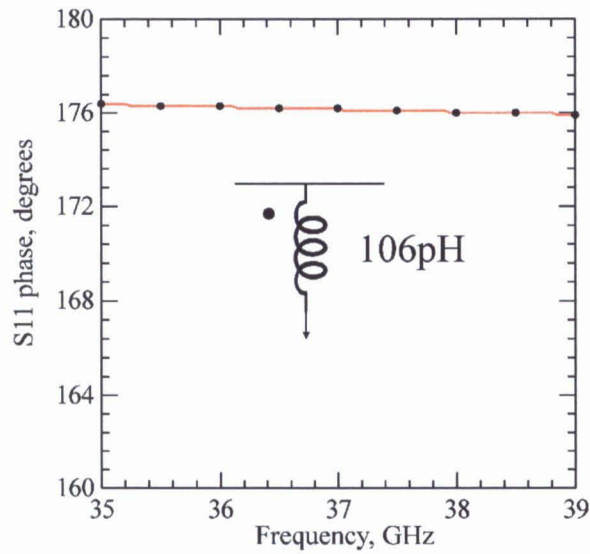


**Figure 3.5.** Model for bias lines (a); gate alone (b); and coupling between gate and bias (c). The GaAs substrate is included in the simulation, and the inductance value is derived from the resulting scattering parameters.

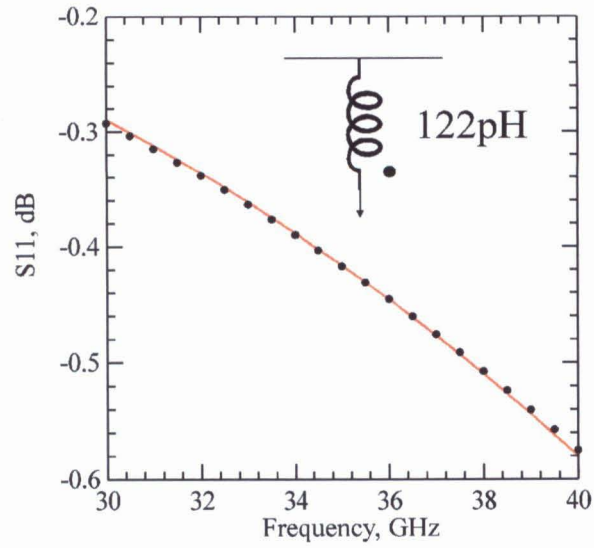


(a)

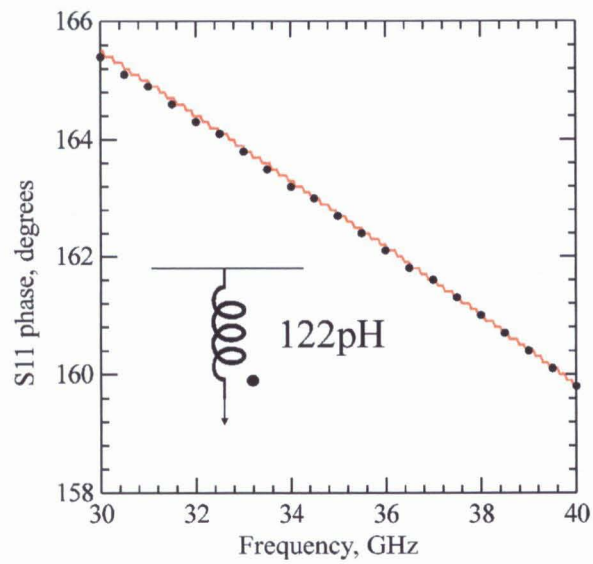


(b)

**Figure 3.6.** Magnitude (a) and phase (b) responses from the equivalent circuits for the bias pattern shown in figure 3.5(a). The solid line results from the circuit model; the dotted line results from HFSS.

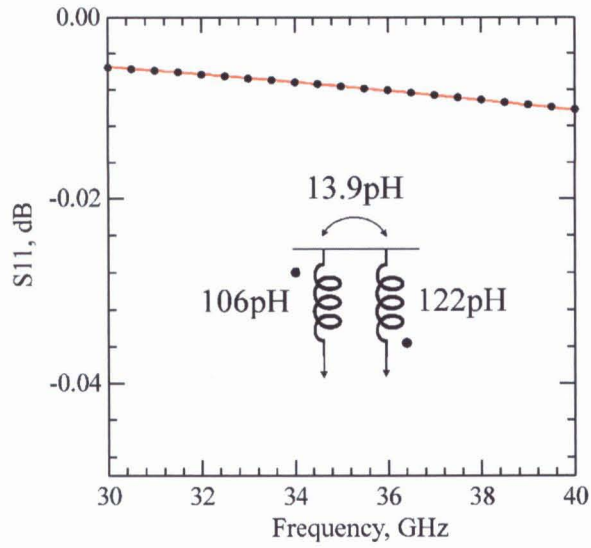


(a)

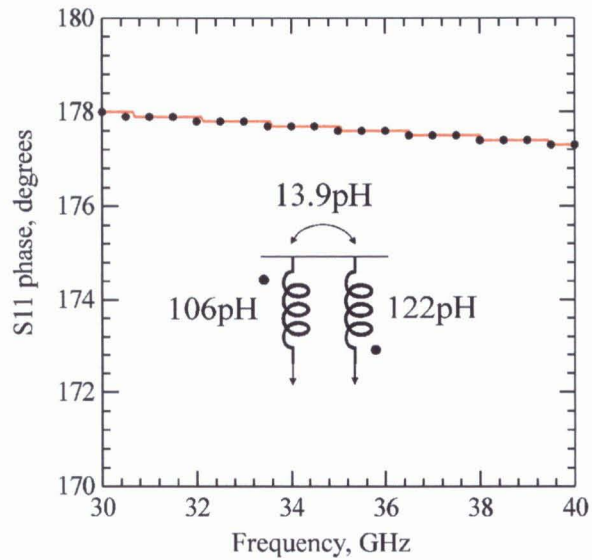


(b)

**Figure 3.7.** Magnitude (a) and phase (b) responses from the equivalent circuit for the gate trace shown in figure 3.5(b). The solid line results from the circuit model; the dotted line results from HFSS.



(a)



(b)

**Figure 3.8.** Magnitude (a) and phase (b) responses from the equivalent circuit for the gate and bias shown in figure 3.5(c). The solid line results from the circuit model; the dotted line results from HFSS.

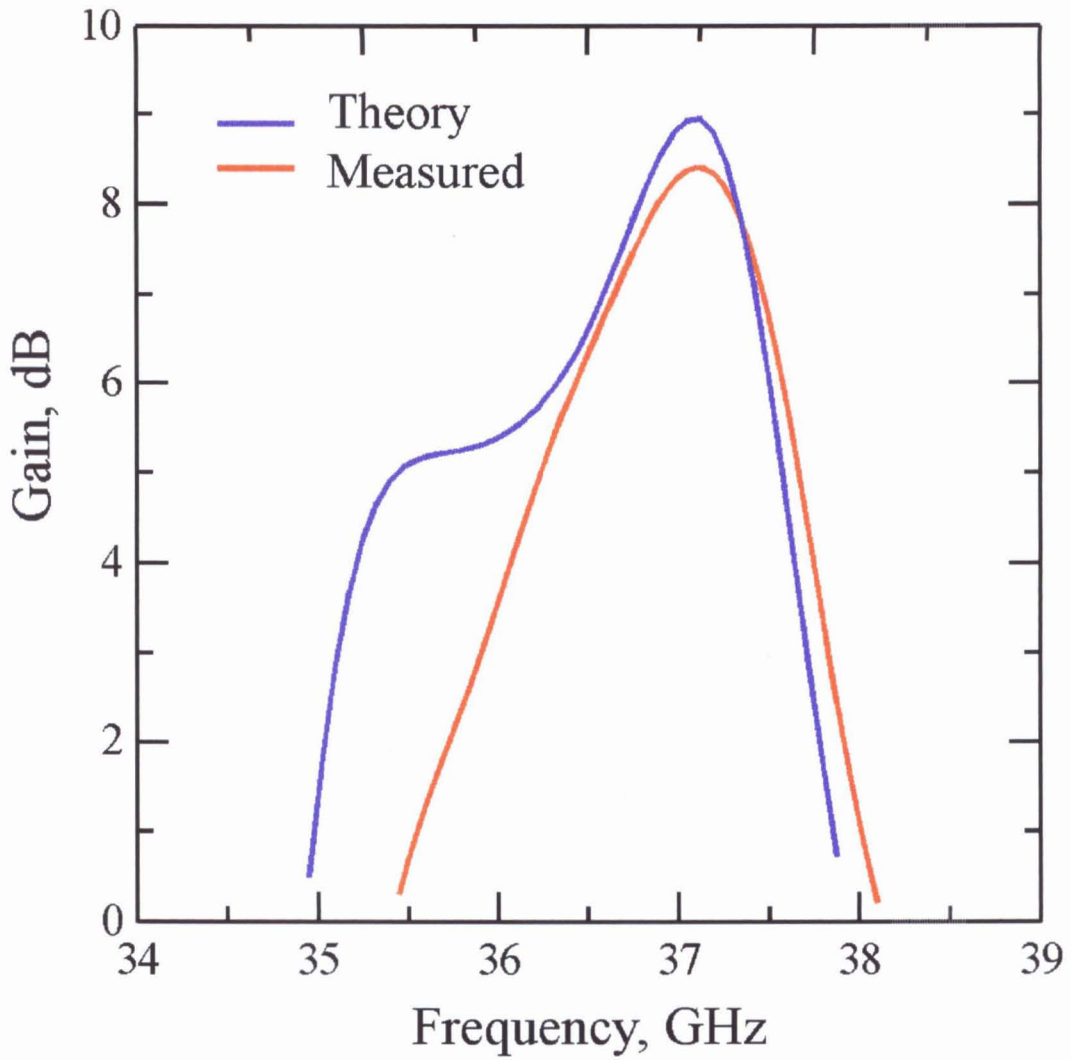


**Figure 3.9.** Small signal performance of the grid amplifier. The peak gain is shown to be 8 dB, with a bandwidth of 3.5%.

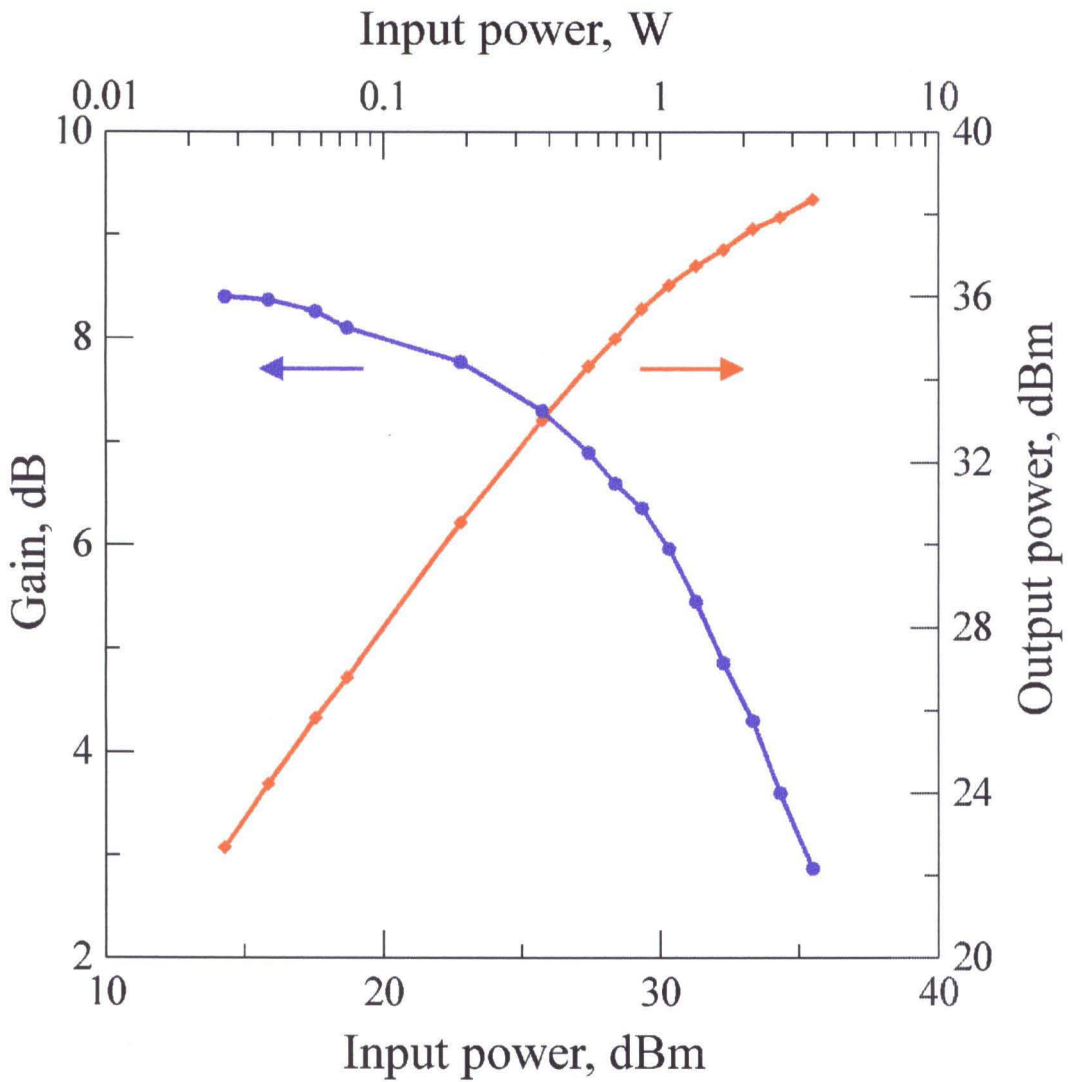


**Figure 3.10.** Gain and power performance of the grid amplifier. The gain of the grid is 5 dB at an output of 5 W.

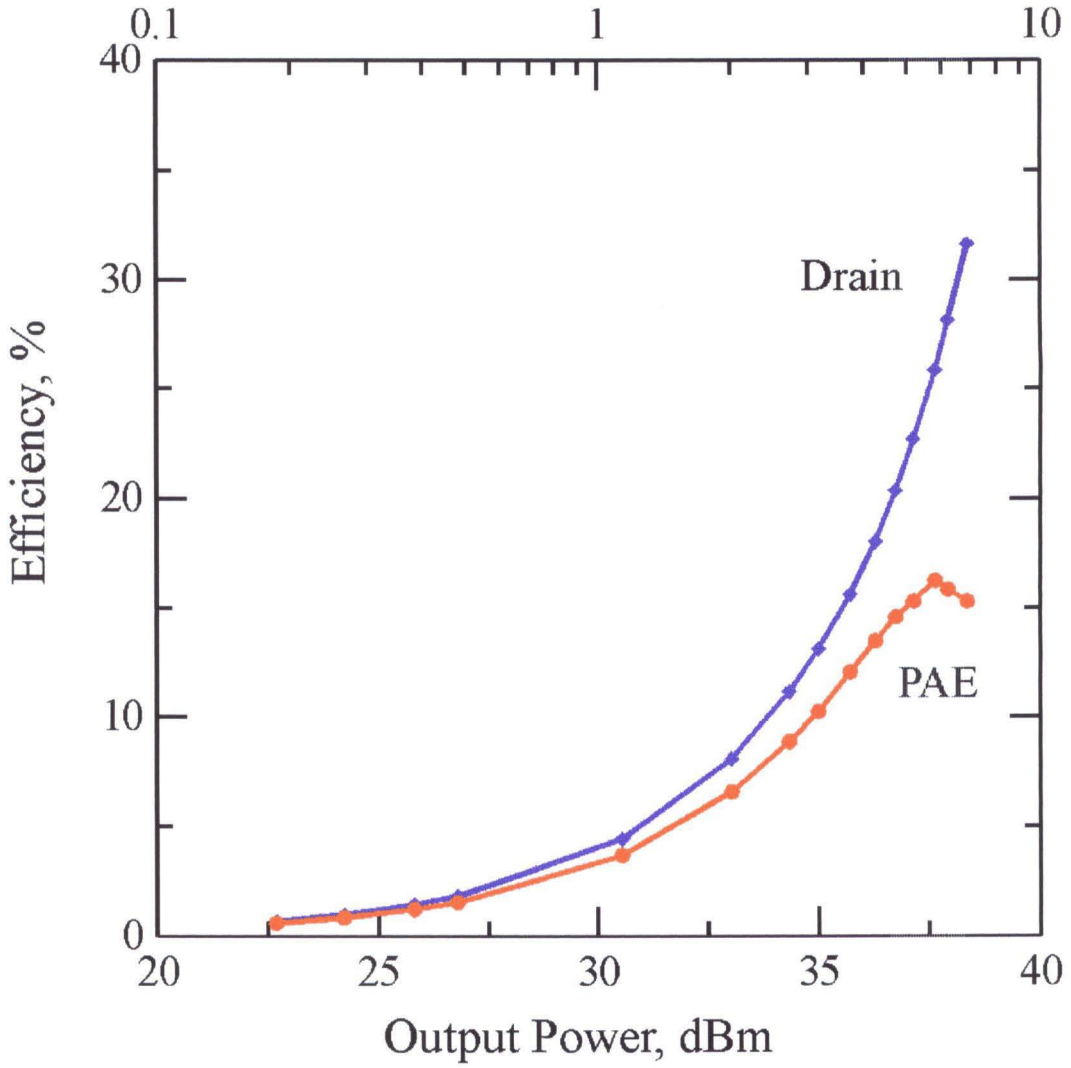
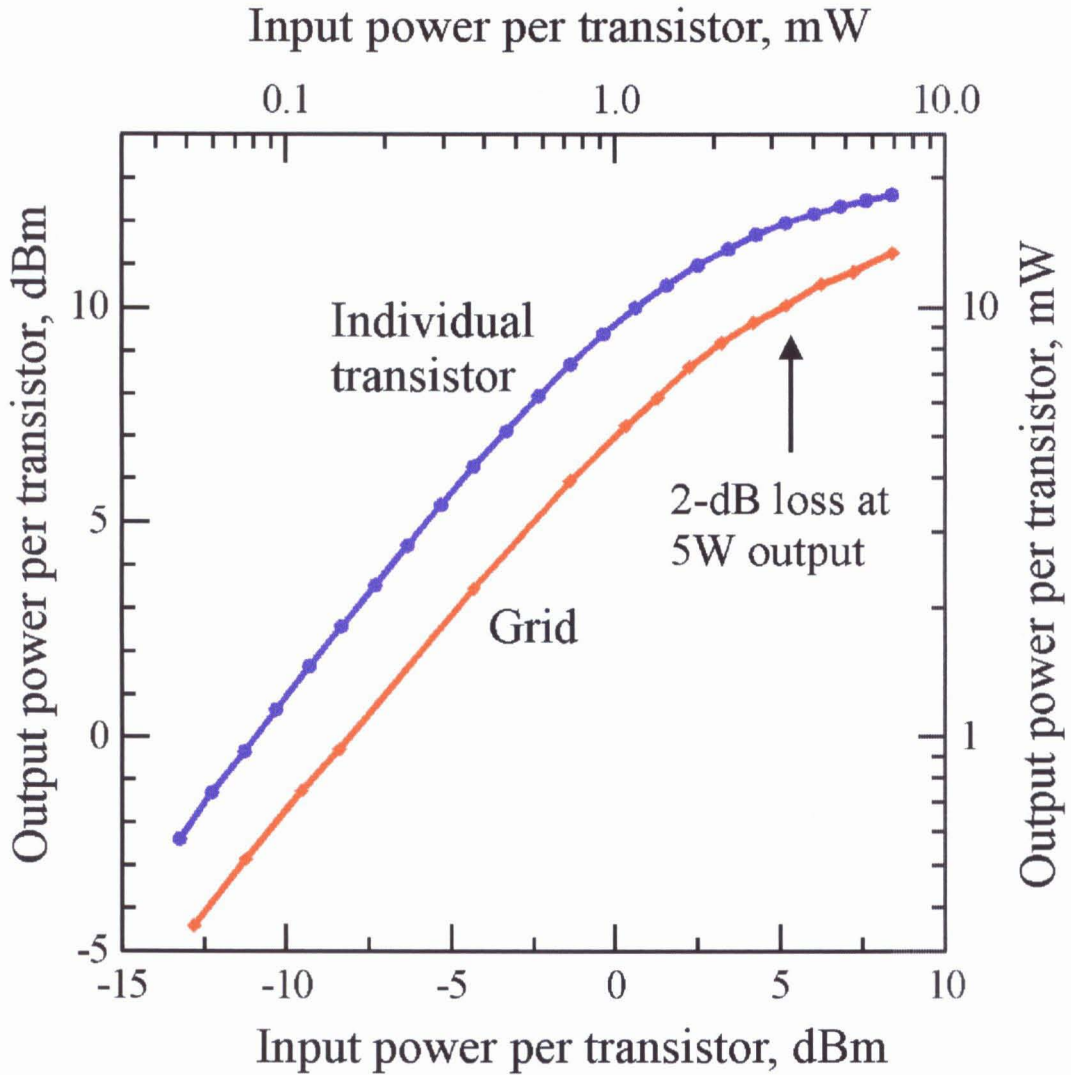


Figure 3.11. Drain and power-added efficiencies of the grid amplifier. At 5 W output, the PAE is 17%.



**Figure 3.12.** Estimate of the combination loss for the grid amplifier. The discrete data is a load pull measurement at 39 GHz, and the amplifier data is taken at 37.2 GHz using devices that have been feedback compensated for stability.

### 3.2 THERMAL MEASUREMENTS

Figures 2.3 and 2.4 show the results of thermal modeling and a simple thermal measurement for the biased grid amplifier. The measurement was made with a mercury thermometer attached to the center of the grid amplifier to sense its temperature under varying DC power applied to the circuit. While the measurement gave some insight into the bulk temperature rise of the grid, it cannot give an estimate of the junction temperatures of the transistors on the grid. A second thermal measurement, done under full operating bias, was made using a ThermaCam PM290 infrared imaging system.

The energy band gap between the conduction and valence bands of bulk gallium arsenide is 1.43 eV, resulting in a strong emission line at  $.87 \mu\text{m}$ , well below the spectrum to which the imager is sensitive. The ThermaCam imaging system used here is sensitive to radiation in the 3-5  $\mu\text{m}$  range. The consequence is that bulk GaAs is transparent over the spectral region where the ThermaCam senses temperature. Figure 3.13 shows that an IR spectrum emitted from behind a GaAs wafer travels directly through the wafer. The only interactions between the GaAs and the IR energy are surface reflections from the dielectric mismatch between GaAs and air. Such reflections complicate the measurement further: figure 3.14 shows a close-up image of the same wafer. The spectrum is a reflection spectrum from the lens: the glass and metal materials of the lens emit a highly non-uniform heat spectrum that is reflected back to the imager from the GaAs wafer. As a consequence, a calibration procedure is necessary to eliminate lens reflections from the measurement, and some procedure is necessary to get at the temperature of the GaAs apart from its inherent emission spectrum.

Calibration to remove the lens reflections from the GaAs surface is accomplished by a correction table available in the camera. The procedure is to point the camera at an isothermal surface, and then sample the image multiple times. Each pixel in the image is then corrected to yield an isothermal image. This

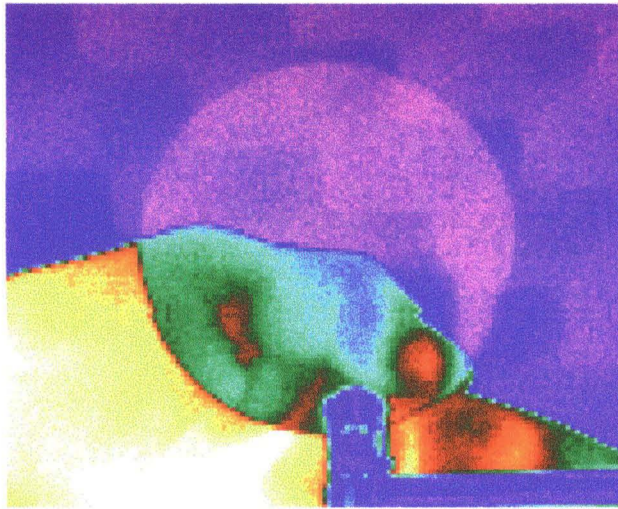


**Figure 3.13.** GaAs is transparent to the IR spectrum detected by the imaging system. The hand behind the GaAs wafer emits IR energy directly through the wafer. The image viewed through the wafer appears different because of the impedance transformation the energy undergoes through the GaAs dielectric mismatch with air.

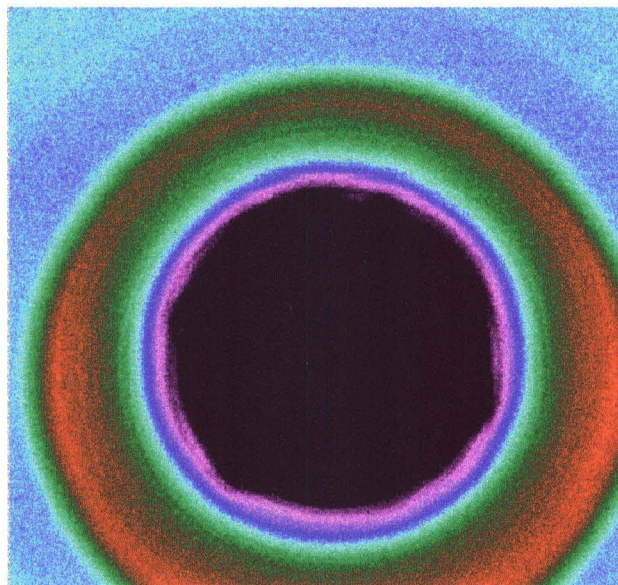


**Figure 3.14.** Lens reflections from a GaAs wafer. The dielectric mismatch between GaAs and air causes the heat spectrum emitted by the lens to reflect directly back to it, resulting in an image of the lens. Note that the glass surface of the lens appears cold. The material used for the optics likely has an extremely low emissivity in the  $3\text{-}5\ \mu$  range of the camera. The result is that the lens surfaces are transparent so that the reflection image shows the detector array, a cryo-cooled surface.

correction table is used to calibrate out lens reflections, and figure 3.15 shows a measurement of the GaAs wafer after the correction was made. The calibration is tremendously sensitive to camera movement. Since the correction is pixel-wise, changes in the reflected image that result from camera movement yield a ghost image of the calibration table in subsequent measurements. Figure 3.15 shows a faint ghost of the correction table that resulted from slight camera vibration. The ambient temperature is set manually to give an isothermal surface at the known temperature of the background (measured with a thermocouple attached to the wafer, not shown here).

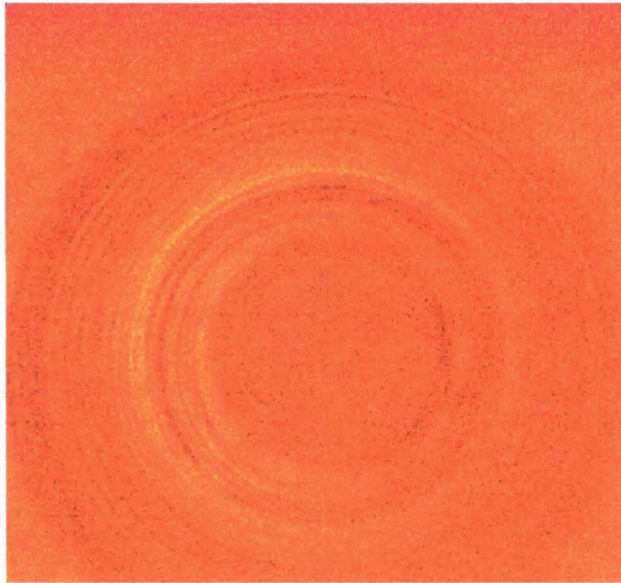
The thermal polymer used to attach the active chip to the heat spreader does, in fact, have strong emission lines in the IR spectrum to which the camera is sensitive. Since the chip is only  $75\ \mu\text{m}$  thick, heat is easily conducted from the substrate to the thermal polymer. The emission spectrum of the thermal polymer can then be detected by the camera to yield an estimate for the temperature of the GaAs in the vicinity of the transistors. The remaining calibration of the imaging system is to set the measurement emissivity to that of the thermal polymer through the GaAs substrate. This is accomplished by attaching a strip of black electrical tape next to the chip and letting it sit sufficiently long to reach thermal equilibrium. Since the emissivity of black electrical tape is known to be  $.95^1$ , the temperature of the tape can be measured very accurately. After measuring the temperature of the tape, the measurement emissivity of the imager is adjusted until the measured temperature of the thermal polymer matches the recorded temperature of the black tape.

Figure 3.16 shows a thermal image of a fully biased grid amplifier. The image shows that the grid operates at about  $55^\circ\text{C}$  with  $60^\circ\text{C}$  hot spots. The bias lines appear cooler because of the emissivity difference between gold and the polymer. The heat profile shown gives an *estimate* of the temperature of the

---

<sup>1</sup> Reported by Thermetrics with the camera literature.

GaAs in the vicinity of the transistors. There are two limits on the resolution that disallow precise measurements of the gate temperatures here. The first is the measurement mechanism itself, as described above: the image is one of a mechanically conducted temperature profile through the GaAs substrate to the polymer. The second is the resolution of the imaging system. The detail of the imager is limited to  $100\mu\text{m}$  steps, so the gate length of  $.18\mu\text{m}$  is *well* below the resolution of the camera. Even the gate width of  $20\mu\text{m}$  per gate finger is not resolvable by the camera, so the resulting image is truly an estimate of the GaAs temperature in the vicinity of the transistors. The typical operating temperature for GaAs power amplifiers is  $150^{\circ}\text{C}$ , so the measurement could be off by more than a factor of 2 and still result in acceptable thermal performance. The conclusion is that the heat spreader cooled by circulating water effectively manages the required heat dissipation for continuous operation of the grid amplifier.



**Figure 3.15.** Calibrated isothermal measurement. The faint ghost of the lens results from camera vibration after calibration.

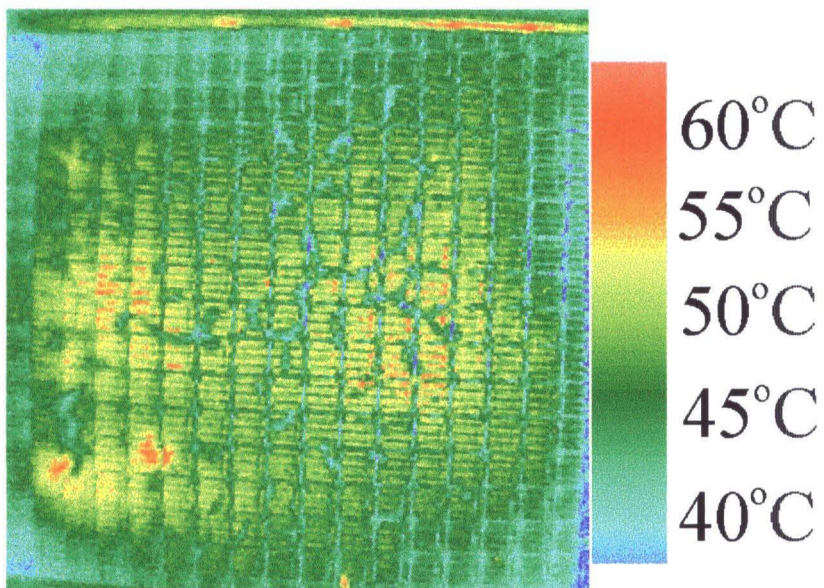


**Figure 3.16.** Thermal image of the grid amplifier running at operating bias. The image shows hot spots of 60°C. The bias lines appear cooler because of differences between the emissivity of gold and GaAs.

## Chapter 4

# Measurements

The modeling of grid amplifiers presented in chapter 2 was formulated from an assumption that the structure is illuminated by a plane wave. There were two important characteristics of the plane wave that allowed the modeling process to be reduced to the unit-cell based circuit theory that has been used. The first property of the plane wave is a uniform amplitude distribution, and the second is a uniform phase distribution. In practice, there are two approaches that have been used to approximate a plane wave illumination of a grid amplifier structure. The first positions the amplifier structure in the far field of a radiating horn so that the phase and magnitude variations of the field across the area of the grid amplifier do not change significantly. The second approach is to exploit the properties of focused gaussian beams.

### 4.1 DESCRIPTION OF FAR-FIELD MEASUREMENTS

The gain of an antenna above an isotropic radiator is defined as the power density at some point in space distant from the antenna, divided by the power density at the same point distant from an isotropic radiator transmitting the same power:

$$G_a = \frac{S_a}{S_i} \quad (4.1)$$

where  $S_a$  is the power density received at the field point from the transmitting antenna and  $S_i$  is the power density received at the same field point from an

isotropic radiator. Integrating the received power density over the full spherical surface at the field point gives the transmitted power:

$$\iint S_a dS = P_t. \quad (4.2)$$

Use of the definition of antenna gain in (4.1) allows (4.2) to be rewritten as

$$\begin{aligned} \iint S_i G_a r^2 d\Omega &= P_t \\ \iint \frac{P_t}{4\pi r^2} G_a r^2 d\Omega &= P_t \\ \iint G_a d\Omega &= 4\pi. \end{aligned}$$

The power received by an antenna of effective area  $A$  in the far field of an antenna with gain  $G$  is

$$P_r = \frac{GA}{4\pi r^2} P_t. \quad (4.3)$$

This is known as Frii's transmission formula. The antenna theorem for lossless structures

$$\iint A d\Omega = \lambda^2$$

can be used to show that

$$\frac{A}{G} = \frac{\lambda^2}{4\pi}$$

so that Frii's transmission formula can be rewritten as

$$\frac{P_r}{P_t} = \frac{A_r A_t}{\lambda^2 L^2}.$$

The pivotal assumption used to derive (4.3) is that the power density incident on the receiving area is constant. This is reasonable provided that the receiving structure area is much smaller than the spatial extent of the transmitter power, i.e., that the receiver lies in the far field of the transmitter. With reference to figure 4.1, Frii's transmission formula can be used in conjunction with knowledge

of the areas of the horns and grid to calculate the power incident on the grid from a measurement of the transmitted power. The formula can be applied again to calculate what power is transmitted from the grid structure to the receiving horn from a measurement of the received power. The gain of the grid can then be calculated from the ratio of the grid's transmitted to incident powers which is given by

$$G = \frac{\lambda^2 L_1^2 L_2^2}{A_g^2 A_h^2} \cdot \frac{P_r}{P_t}$$

where  $L_1, L_2$  are the far-field distances of the horns and grid, respectively;  $A_g, A_h$  are the areas of the grid and horns, respectively; and  $P_r, P_t$  are the received and transmitted powers, respectively. The effective areas of the horns can be measured by positioning two identical horns facing each other in the far field, measuring the ratio of transmitted to received power, and then applying Frii's formula to determine

$$A_h = \sqrt{\frac{P_r}{P_t} \cdot \lambda^2 L^2}$$

where  $A_h$  is the effective area of the horns, and  $L$  is the far-field distance for the horns. This technique has been used by various researchers [3-5] to measure the gain and power performance of grid amplifiers.

The difficulty in making measurements with the far-field technique is that the inherent space loss associated with it, which can become rather large, limits the dynamic range of the system. Reflection measurements are difficult, and vector measurements may be next to impossible. Another approach to free-space measurements is to use a focused beam system.

## 4.2 GAUSSIAN BEAM OPTICS

Though a Gaussian beam system is a bit more difficult to setup and calibrate than a far-field system, one of its primary advantages is that transmitted power can be focused to a small spot. Positioning the grid amplifier at the focal point of the system ensures that most of the power in the beam is delivered to

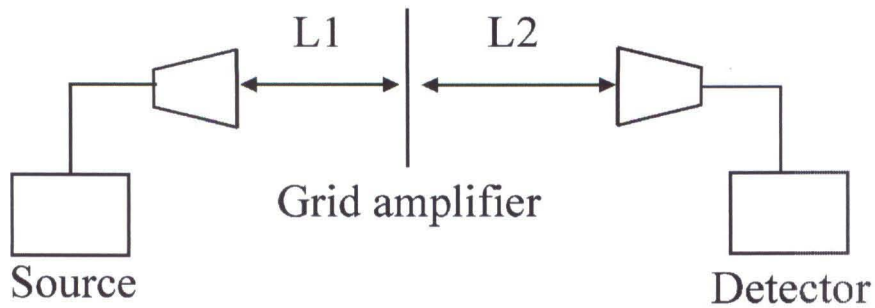


**Figure 4.1.** Far-field measurement set up. The grid amplifier is located in the far field of the transmitting horn, and the receive horn is located in the far field of the grid amplifier. Frii's transmission formula is used to de-embed the space loss and calculate the power gain of the grid, assuming its radiating area is equal to its geometrical area.

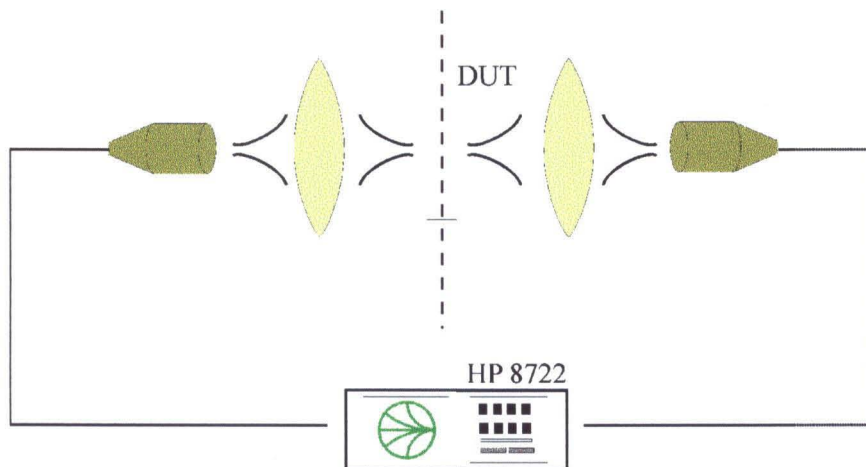


**Figure 4.2.** Simplified schematic of a gaussian beam measurement setup suitable for two-port measurements. Because a large fraction of the transmitted power impinges on the grid amplifier, a vector network analyzer can be used directly as the power source. The horns are corrugated feed horns that launch a highly gaussian beam in the fundamental mode.

it. As a result, the power source for small-signal measurements can be supplied by a network analyzer, allowing direct vector measurements of all four of the grid amplifier's scattering parameters. Figure 4.2 shows a simplified layout of the focused beam measurement system that is an extension of Gagnon's reflectometer [1] and has been used by Koliass [2] and others to make grid amplifier measurements.

Treatment of Gaussian beam optics can be found in numerous sources [6-7], and a derivation of some of the important properties of Gaussian beams is given in the appendix. Gaussian beam systems offer at least two very attractive characteristics for use in measurement apparatuses. The first is that the field can be derived at any point in space from a few simple relations using techniques similar to ray tracing with geometrical optics. The second is that the spot of a focused gaussian beam (the *beam waist*) has a uniform phase distribution over its area.

The fundamental Gaussian beam mode is given by [6]:

$$u = \sqrt{\frac{2}{\pi w^2}} \exp\left(\frac{-r^2}{w^2} - ikz - \frac{i\pi r^2}{\lambda R} + i\phi\right)$$

where  $w$  is the  $1/e$  radius of the field;  $k$  is the propagation constant; and  $R$  is the beam's radius of curvature. The  $1/e$  radius and radius of curvature are given by

$$w = w_0 \sqrt{1 + \left(\frac{\lambda z}{\pi w_0^2}\right)^2}$$

$$R = z + \frac{\left(\frac{\pi w_0^2}{\lambda}\right)^2}{z}$$

where  $w_0$  is the minimum size of the beam radius; the beam waist. The inverse relations allow determination of the waist radius and position of the waist given a beam radius and radius of curvature at some point in space:

$$w_0 = \frac{w}{\sqrt{1 + \left(\frac{\pi w^2}{\lambda R}\right)^2}}$$

$$z = \frac{R}{1 + \left(\frac{\lambda R}{\pi w^2}\right)^2}.$$

Starting from an analysis of the horns used to launch a Gaussian beam, the above relations can be used to determine the field at any point in space. Defining a *complex beam parameter*  $q$  by

$$q = z + iz_c,$$

$$z_c = \pi w_0^2 / \lambda,$$

it can be shown that the same ray matrices used to transform geometrical rays can be used to transform the complex beam parameter. This is a tremendous advantage in system design as it reduces a complex field problem to multiplying a few matrices. For a system matrix of the form

$$\begin{pmatrix} A & B \\ C & D \end{pmatrix},$$

operating on an input beam parameter  $q_{in}$ , it can be shown that the output beam parameter is given by [6]

$$q_{out} = \frac{(Aq_{in} + B)}{(Cq_{in} + D)}.$$

With reference to figure 4.3,  $q_{out}$  can be inverted to give

$$d_{out} = \frac{(Ad_{in} + B)(Cd_{in} + D) + ACz_c^2}{(Cd_{in} + D)^2 + C^2z_c^2}$$

$$w_{o\ out} = \frac{w_{o\ in}}{\sqrt{(Cd_{in} + D)^2 + C^2z_c^2}}.$$

With these relations, a focused beam measurement system can be designed readily. Table 4.1 shows three of the matrices germane to focused beam system design.

Component	Ray Matrix
Thin lens	$\begin{pmatrix} 1 & 0 \\ -1/f & 1 \end{pmatrix}$
Thick lens	$\begin{pmatrix} 1 + \frac{(n_2 - n_1)t}{n_2 R_1} & \frac{n_1 t}{n_2} \\ -1/f - \frac{t(n_2 - n_1)^2}{n_1 n_2 R_1 R_2} & 1 + \frac{(n_1 - n_2)t}{n_2 R_2} \end{pmatrix}$
Propagation	$\begin{pmatrix} 1 & L \\ 0 & 1 \end{pmatrix}$
Dielectric interface	$\begin{pmatrix} 1 & 0 \\ 0 & \frac{\sqrt{\epsilon_{r1}}}{\sqrt{\epsilon_{r2}}} \end{pmatrix}$

**Table 4.1.** Several common matrices used in designing quasi-optic systems.

The setup used to measure the grid amplifier is similar to that shown in figure 4.2. The lenses used are plano-convex hyperbolic, cut from Rexolite. The lens diameter and focal length are 12 inches. The bi-convex arrangement is accomplished by concatenating two plano-convex lenses, giving a converging lens with a focal length of 1/2 that of the individual plano-convex lenses. With reference to figure 4.3, using a thin lens as the optical system, the magnification of the beam waist,  $w_{out}/w_{in}$ , and its location are plotted as a function of input

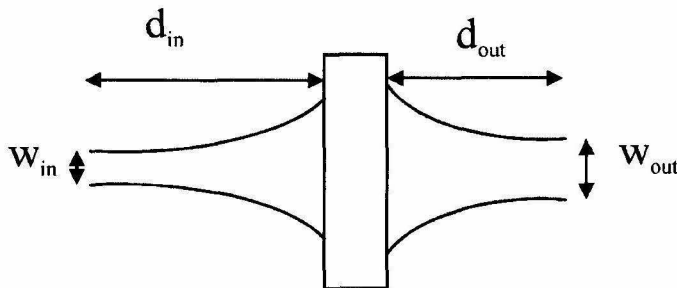


**Figure 4.3.** Generic system layout to calculate the location and size of the exiting beam waist. The system is described by an ABCD matrix similar to those used in geometrical optics. Matrix transformation is performed on the complex beam parameter at the input, and the output parameters result from the output complex beam parameter.

distance in figure 4.4.

The phase over the plane where the Gaussian beam waist is located is constant. Placing the grid amplifier at this plane ensures that the phase condition for the plane wave assumption is satisfied. The magnitude, however, cannot be uniform by virtue of the focused property of the beam. But if the extent of the waist is such that the amplitude variation of the beam across the area of the grid can be kept small, a plane amplitude distribution can be approximated. Figure 4.5 shows beam scans at the location of the beam waist in the focused system used here. The magnification of the beam was set at 2, which gave a beam amplitude difference of 1 dB from the center of the grid to the edges. H-plane, E-plane, and theoretical plots are all shown to register exactly. This suggests that the beam is highly symmetric, and that the simple matrix theory shows suitably accurate results.

A few caveats need to be pointed out. Siegman [11] illustrates the near-field effects of truncating a gaussian beam. Truncating a beam so that 99% of the power is transmitted leads to a near-field ripple of 17%. This ripple can cause several performance degradations in a grid amplifier. The first is that the cells located near the minima of ripples are driven at a lower power level than devices near the maxima. This can cause poor saturation performance of the grid. The second degradation is that the rippling field may sufficiently violate the plane-wave approximation as to disrupt the cell-to-cell coupling and give results not predicted by the model.

### 4.3 CALIBRATION

The setup of figure 4.2 was used to measure the small signal performance of the grid amplifier. Because a large fraction of the transmitted power impinges on the grid, small signal measurement can be done directly with the network analyzer after an appropriate calibration has been performed. There are two classes of measurement conditions relevant to focused gaussian beam systems.

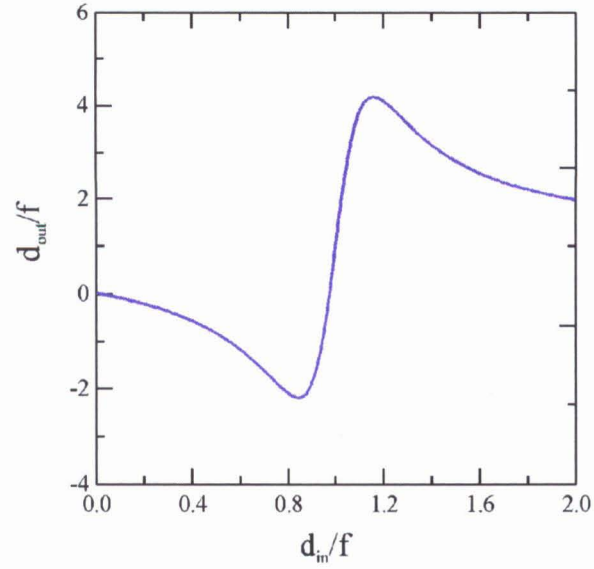


**Figure 4.4a.** Distance from the output surface of a thin lens to the beam waist. Note that until the input waist is sufficiently distant from the lens, the output waist distance is negative. This means that the input beam is diverging too rapidly for the lens to focus. The result is a diverging beam at the output of the lens.

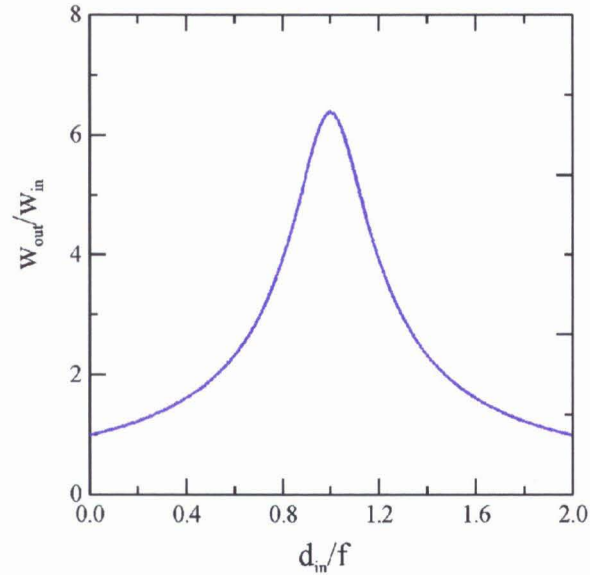


**Figure 4.4b.** Magnification for the single lens system. Note that with the lenses used here, the maximum magnification is about 6. Also note that with the input distance equal to twice the focal length, the output distance is equal to the input distance, and the magnification is 1.

The first is the class of conditions for which the measured structure is larger in spatial extent than the focal spot of the beam. In this case, calibration standards are usually simple to devise and measurements can be performed directly on the structure of interest. The second class of conditions complicates the measurement and calibration procedures considerably, and usually requires that measurements be performed on some modified structure. This is the case when the focal spot of the measurement beam is larger than the structure of interest.

#### 4.3.1 CALIBRATION FOR TRANSMISSION MEASUREMENTS

Calibration for transmission measurements when the focal spot of the measurement beam is smaller than the structure under test can be accomplished with straightforward transmission standards. Provided that the structure under test is not highly reflective, a simple response calibration can be used that corrects measurement data for transmission path loss and distortion. The calibration is performed by aligning the horns and leaving the focal plane vacant. The measured transmission coefficient becomes the calibration factor. The only caveat is that this is a co-polarized measurement. Cross-polarized measurements can use the resulting calibration factor if one of the horns is rotated after calibration, a process that has been shown to introduce negligible error. Alternatively, a known transmission standard may be inserted into the measurement plane that rotates the polarization of the beam. This technique is most useful when the beam is larger than the structure under test, and is described below.

A wire polarizer oriented at  $45^\circ$  with respect to the input horn divides the incident beam into components parallel and perpendicular to its wires. The wire polarizer reflects half of the incident power back to the input, and allows half to pass to the receive horn. The OMT at the back of the receive horn divides the received beam (impinging at  $45^\circ$  with respect to its ports) into components parallel and perpendicular to its ports. Half the receive power is delivered to a matched termination, and half is sent to the network analyzer. This mechanism

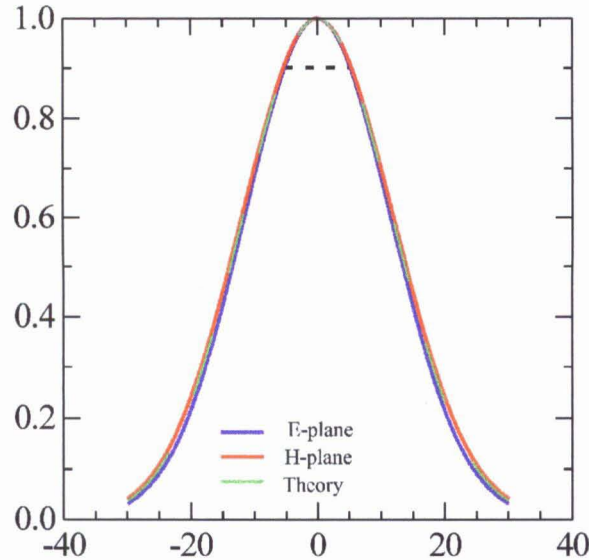


**Figure 4.5.** Beam scans and predicted beam profile. The scans and predictions lineup very closely showing that the simple Gaussian beam theory gives acceptable results.

results in  $1/4$ , or  $-6$  dB, transmission, giving a  $-6$  dB calibration standard. Figure 4.6 shows a photograph of the wire polarizer used here. Provided that the polarizer has the same area as the grid amplifier, it provides a  $-6$  dB calibration standard for transmission measurements.

#### 4.3.2 CALIBRATION FOR REFLECTION MEASUREMENTS

Calibration for reflection measurements is generally more difficult than calibration for transmission measurements<sup>1</sup>. As with transmission measurements, calibration proceeds differently for structures smaller or larger than the focal spot of the beam. The following calibration technique is published in [9].

For structures that are larger than the focused beam, calibration for reflection measurements is simple and uses the signal flow model shown in figure 4.7. In the figure, port  $a_i$  represents the network analyzer excitation port and  $b_i$  represents the network analyzer measurement port for reflected signals.  $S_{11}$ ,  $S_{22}$ ,  $S_{21}$ , and  $S_{12}$  give a linear model for distortion to an excitation signal introduced by

<sup>1</sup> Assuming structures that are not highly reflective. Full two-port calibration is required to make accurate transmission measurements of structures that are not well matched.

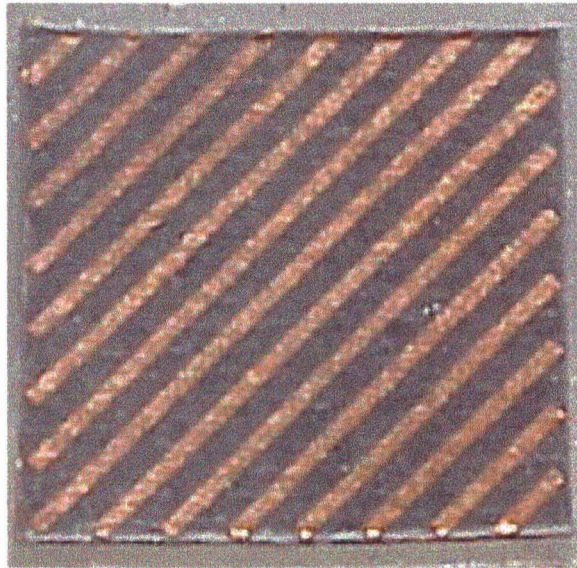


**Figure 4.6.**  $-6$  dB calibration standard. The polarizer has the same area as the grid amplifier, and is oriented at  $45^\circ$  with respect to the incident beam, and hence horns. The traces are of different lengths so as to avoid stray resonances that may be excited between them.

imperfections in the signal path: cable mismatches, coupler directivity, connector mismatches, and so forth. Direct application of Mason's rule results in the expression

$$S_{11m} = S_{11} + \frac{S_{12}S_{21}\Gamma_L}{1 - S_{22}\Gamma_L} \quad (4.4)$$

where  $S_{11m}$  is the reflection measured at port  $b_i$ , and  $\Gamma_L$  is the reflection coefficient of the structure under test. Since  $S_{21}$  and  $S_{12}$  show up only as a product and not individually, (4.4) involves three complex, independent unknowns that are necessary to measure<sup>2</sup>. Three known standards are thus necessary, and it is particularly convenient to use a match and a short. Use of absorbing material at some distance from the focal plane of the measurement system provides an excellent match, and from a reflection measurement of it (4.4) collapses directly to yield  $S_{11}$ . Knowledge of  $S_{11}$  reduces (4.4) to two complex linear equations with the unknowns  $S_{12}S_{21}$  and  $S_{22}$ . Use of a large, flat metal sheet mounted on a translation stage provides a short that can either reside exactly at the measurement plane or be delayed for a second known standard [9].

Following this calibration procedure, a test measurement was made on a large sheet of dielectric material placed in the measurement plane. Figure 4.8 shows smith chart data for both reflection and transmission measurements compared to models. As shown in the figure, the measured and modeled responses register exactly, showing the calibration procedure to be trustworthy.

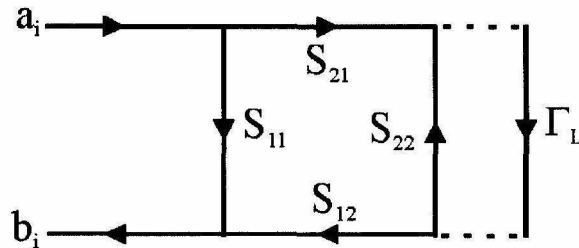


**Figure 4.7.** Signal flow graph representation for the error model used to calibrate the network analyzer.

<sup>2</sup>Since  $S_{21}$  and  $S_{12}$  always show up as a product, it is common in the literature to assign a value of 1 to  $S_{21}$  in the flow graph, and then represent  $S_{12}$  as the product  $S_{12}S_{21}$ .

After development of the calibration technique, a bandpass structure was measured and the data were compared to HFSS simulations of the array [9]. Figure 4.9 shows the comparison between theory and measurement, and it is again shown to register very well.

When the measurement beam is larger than the structure under test, the simple calibration procedure described above cannot be used. One of the complicating factors to the measurement is that a match standard may be impossible. But even if a match could be designed, it may not be possible to include the entire test structure in the measurement after calibration.

The accuracy of the calibration depends on the fixture that supports the test structure to remain constant between calibration and actual measurement. The grid amplifier is mounted on a large aluminum heat spreader so that reflections from the heat spreader outside the area of the grid amplifier need to be calibrated out of the measured data. Calibration standards, then, need to have the same shape and area as the grid amplifier, surrounded by aluminum nitride exactly as the grid amplifier. Fabricating a match standard would involve, hence, cutting a square aperture that has the same area as the grid amplifier in a slab of aluminum nitride. The measurement beam could be focused into the aperture and a sheet of absorber could be used as a match. There are at least two difficulties in applying this technique. The first is that cutting a precise aperture in aluminum nitride is forbidding. A laser cutter may be used, but the thickness of the substrate may prevent the cutter from penetrating it entirely. The second problem is that the thickness of the substrate would present an oversized waveguide to the impinging beam, distorting the fields the standard is supposed to calibrate. This effect may be negligible, but quantifying it is difficult.

The measurement is complicated by the fact that the grid is tuned by the use of polarizers that are larger than the amplifier chip. Tuning usually involves some movement of the polarizers after the amplifier is assembled in the measurement

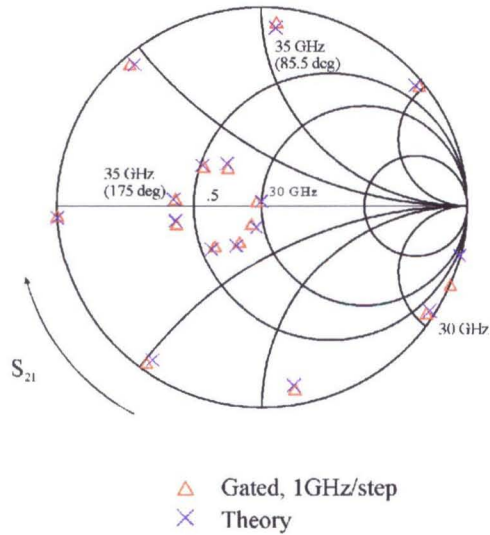


**Figure 4.8.** Measurements of a 1-inch thick slab of polystyrene. The slab is modeled as a TEM transmission line. Note that the measurement registers directly with the theoretical prediction.

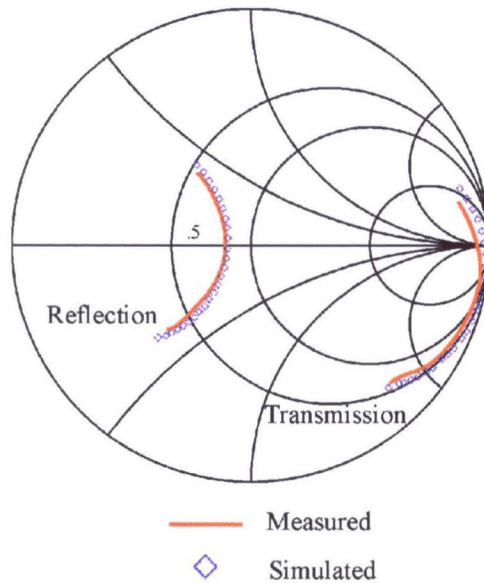


**Figure 4.9.** Measurement of a bandpass array using the calibration procedure described. This measurement is presented in [2].

plane. Because the polarizers are larger than the grid, the area of the polarizers beyond the edges of the amplifier chip appear to the measurement apparatus as fixturing. So either calibration needs to be performed with the polarizers present, or measurement must exclude them. But if the calibration is performed with the polarizers present, they cannot be moved to tune the grid, or the fixturing changes. Apart from that, calibration with the polarizers present would remove their effects from the measurement data, giving an apparently untuned result that is erroneous. As a consequence, reflection measurements for the grid amplifier were made without the polarizers.

Expanding (4.4) into a set of three complex equations results in the following:

$$S_{11m_i} = S_{11_i} + \frac{S_{p_i} \Gamma_L}{1 - S_{22_i} \Gamma_{L_i}} \quad (4.5)$$

where  $i = 1, 2, 3$  and  $S_{p_i}$  is the product  $S_{12}S_{21}$ . Without a match standard to deliver the value of  $S_{11_i}$  directly, it is apparent that (4.5) represents a system of three nonlinear, complex equations to be solved simultaneously. One efficient method for solving the system is to expand it into a set of six nonlinear real equations by dividing (4.5) into its real and imaginary parts. Straightforward (although a bit cumbersome) algebra results in the following set of equations:

*Real part :*

$$\begin{aligned} S_{11m}^r &= S_{11}^r - \Gamma_L^r S_{11}^r S_{22}^r + S_{11}^i S_{22}^i \Gamma_L^r + S_{11}^r S_{22}^i \Gamma_L^i \\ &+ S_{11}^i S_{22}^r \Gamma_L^i + S_{22}^r \Gamma_L^r S_{11m}^r - S_{22}^i \Gamma_L^i S_{11m}^r - S_{22}^r \Gamma_L^i S_{11m}^i \\ &- S_{22}^i \Gamma_L^r S_{11m}^i + S_p^r \Gamma_L^r - S_p^i \Gamma_L^i \end{aligned}$$

*Imaginary part :*

$$\begin{aligned} S_{11m}^i &= S_{11}^i - S_{11}^r S_{22}^i \Gamma_L^r - S_{11}^i S_{22}^r \Gamma_L^r - S_{11}^r S_{22}^r \Gamma_L^i \\ &+ S_{11}^i S_{22}^i \Gamma_L^i + S_{22}^r \Gamma_L^i S_{11m}^r + S_{22}^i S_{11m}^r \Gamma_L^r + S_{22}^r S_{11m}^i \Gamma_L^r \end{aligned}$$

$$-S_{22}^i S_{11m}^i \Gamma_L^i + S_p^r \Gamma_L^i + S_p^i \Gamma_L^r$$

where the superscripts  $r, i$  indicate real or imaginary parts, respectively, and  $\Gamma_L$  are the standards used. At this point, any number of numerical solvers may be applied to the system to solve for the unknowns. The Newton-Raphson method is a simple, yet efficient, numerical method that solves for the roots of a given function. The principal (in one dimension) is to approximate the function at a given point with a line, and solve for the intersection of that line with the  $x$  axis. Let  $f(x)$  be some real-valued function of  $x$  with at least one real root. Applying a Taylor expansion,  $f$  may be approximated by [10]

$$f(x + \delta) \approx f(x) + f'(x)\delta + \frac{f''(x)}{2}\delta^2 + \dots \quad (4.6)$$

Ignoring terms proportional to  $\delta^2$  and above, a linear approximation for  $f(x + \delta)$  can be easily solved to give

$$\delta = -\frac{f(x)}{f'(x)}.$$

The significance of  $\delta$  is that it represents the distance from a guess  $x$  to the root of  $f$ , so the next guess to use is  $x + \delta$ . This procedure may be iterated with successive guesses

$$x_{k+1} = x_k - \frac{f(x_k)}{f'(x_k)}$$

until a precision limit has been reached (say  $\delta < 10^{-12}$ ). This method generalizes easily into multiple dimensions. Let  $f_i(\mathbf{X})$  be a set of  $n$  functions ( $i = 1, 2 \dots n$ ) of vector  $\mathbf{X}$ . Then by a Taylor series [10],

$$f_i(\mathbf{X} + \delta\mathbf{X}) = f_i(\mathbf{X}) + \sum_{j=1}^n \frac{\partial f_i}{\partial x_j} \delta x_j + O(\delta\mathbf{X}^2), \quad (4.7)$$

where  $x_j$  are components of the vector  $\mathbf{X}$ , and  $O(\delta\mathbf{X}^2)$  is a sum of all terms in the series proportional to  $\delta\mathbf{X}^2$  or higher powers. Again neglecting all terms of  $O(\delta\mathbf{X}^2)$ , the roots of (4.7) are given by

$$\sum_{j=1}^n \frac{\partial f_i}{\partial x_j} \delta x_j = -f_i. \quad (4.8)$$

(4.8) is a system of  $n$  linear equations to be solved for  $\delta x_j$  that are the components of  $\delta \mathbf{X}$ , the distance from  $\mathbf{X}$  to the root of  $f$ . Setting  $\mathbf{X}_{k+1} = \mathbf{X}_k + \delta \mathbf{X}$  results in an iterative process that can be continued until some precision limit is reached. Note that the procedure depends on the function evaluated at  $\mathbf{X}$  as well as its derivative there. There are two procedures to find the derivative of  $f$  at  $\mathbf{X}$ . The first is to use the numerical approximation

$$\frac{\partial f_i}{\partial x_j} \approx \frac{f_i(\mathbf{X} + \delta x_j) - f_i(\mathbf{X})}{\delta x_j}.$$

The difficulty is that overflow may be a real problem, and other numerical ghosts may haunt the application of this technique. For complicated functions, this may be the only alternative. But the real and imaginary parts of (4.5) are simple monomials that have well-behaved derivatives, so the exact expressions for  $\partial f_i / \partial x_j$  were used here.

The solution process needs to be carried out at each frequency point in the measurement sweep. Initial guesses for all  $x_j$  need to be given to start the process. Because the network of figure 4.7 is passive, we expect that the magnitudes of all the error terms are less than unity. Conveniently, then, initial guesses for all  $x_j$  may be set to some small value less than 1. From experience, the error terms oscillate quickly with frequency. To improve the execution efficiency of the code, the initial guesses for successive frequency points are set to the solution of the preceding frequency point<sup>3</sup>. Once the system has been solved for each frequency point in the measurement sweep, the error terms can be downloaded directly to the network analyzer.

With reference to figure 4.10, three standards can be constructed on a slab of aluminum nitride identical to the heat spreader of the grid amplifier. It is relatively simple to deposit metal on a ceramic substrate, so two of the reflection

---

<sup>3</sup> Code written in C++ to implement this procedure converged to the solutions of the error terms in 3 or fewer iterations per frequency point, and solved for 201 points in less than 1 second running on a 100 MHz processor.

standards are shorts. The first is a short on the back surface the aluminum nitride (a flush short), and the second is a short on the front surface to give a dielectric delayed short. The third standard is a transmission line backed by a match, and it is accomplished by a blank heat spreader. Figure 4.11 shows the equivalent circuits used to calculate the reflection coefficients of the standards, and they are given as:

$$\Gamma_{L_{flush}} = -1$$

$$\Gamma_{L_{delay}} = \frac{j \frac{Z_0}{Z_a} \tan(2\alpha) - 1}{j \frac{Z_0}{Z_a} \tan(2\alpha) + 1}$$

$$\Gamma_{L_{line}} = \frac{Z_L - Z_a}{Z_L + Z_a},$$

$$Z_L = Z_0 \frac{Z_a + j Z_0 \tan(2\alpha)}{Z_0 + j Z_a \tan(2\alpha)}$$

where  $Z_0$  is the TEM impedance of the aluminum nitride heat spreader,  $Z_a$  is the TEM impedance of free space, and  $\alpha$  is the electrical thickness of the aluminum nitride.

Following calibration of the system with this technique, a reflection measurement of the grid amplifier was made without the polarizers. Figure 4.12 shows a comparison between simulated and measured reflection performance. Figure 4.13 shows the circuit model used to predict the reflection. Some of the difference between measurement and prediction may be due to the sensitivity that the calibration technique has to the positions of the standards and the test structure. Small movements result in large errors. Several sources of placement error exist. The first is the precision with which the metal short can be placed on the fixture substrate. The short standards are metal squares placed between the bias traces where the grid amplifier sits. The delayed short can be positioned very accurately between the bias traces, but its location along their length is difficult to control. Positioning the flush short is difficult because it is located on the *opposite* side of the substrate from the bias traces. Figure 4.14 shows the

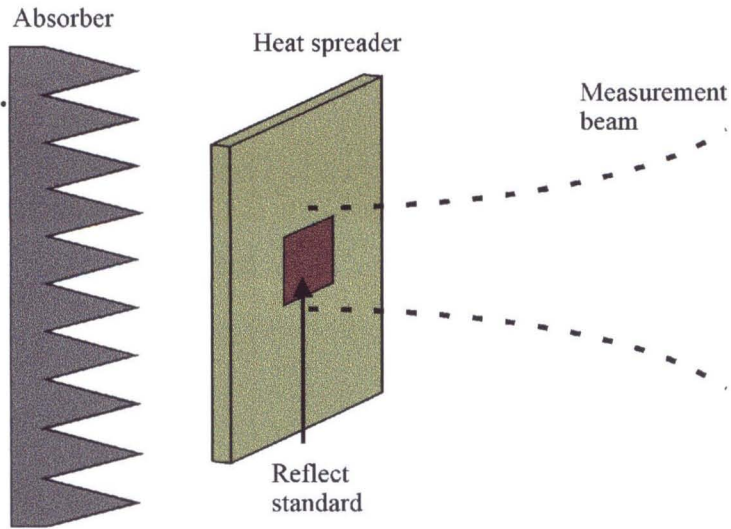


**Figure 4.10.** Calibration standard setup for reflection measurements. The first standard is a short on the back surface of the slab, the second is a short on the front surface of the slab, and the third is a blank slab. The aluminum nitride slab has the same dimensions as the grid amplifier's heat spreader. The structure is backed by absorber to eliminate spurious reflections from the environment.

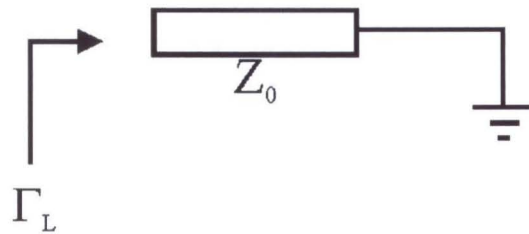


**Figure 4.11a.** Equivalent circuit used to determine the reflection coefficient for a delayed short. The transmission line represents the heat spreader.

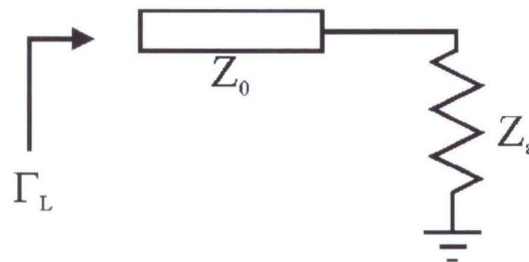


**Figure 4.11b.** Equivalent circuit used to determine the reflection coefficient for a delayed air match. The transmission line represents the heat spreader, and the resistance  $Z_a$  represents the TEM impedance of free space.

difficulties schematically. Another source of error is clearly that the cooler is not *exactly* identical to the standards. The grid amplifier is held in its cooler with a rubber seal to prevent water leaks. The standards are held in a cooler without the rubber seal. The seal should not interfere with the beam as it ought to be far outside of its radius, but its thickness causes the cooling frame to be slightly closer to the horn than the cooler holding the standards. As such, there is some error introduced by this difference.

Another source of error is in placing the grid amplifier. After calibration, the fixture used to hold the standards has to be removed from the focal plane, and the grid amplifier inserted. The position of the grid amplifier has to be adjusted by hand using micrometers. Placing the grid in the exact location as the standards with the exact angular orientation is difficult at best. An attempt at controlling the positioning of the grid structure was made by setting up two laser beams to intersect at the focal plane. This can control the longitudinal position of the grid reasonably accurately, but the lateral positioning is limited to eye-ball adjusting position of the grid so that the beam intersection occurs at the center of the standards and grid. A third laser beam was set up to control the angular positioning of the standards and grid. Reflecting the beam off of the heat spreader toward a target allows control of the angular position of the grid. Figure 4.15 shows the setup for the laser alignment used here.

#### 4.4 POWER MEASUREMENTS

A few additions to the system of figure 4.2 are made to measure the power performance of the grid amplifier. The test port power of the HP8722 network analyzer used for the measurement is limited to around  $-10$  dBm, a level far too low to measure a saturation curve for the grid. In order to increase the available power from the network analyzer, a traveling wave tube amplifier (TWTA) built by Amplifier Research was inserted in the forward path. A coupler was inserted directly after the TWTA to track the incident power. A second cou-

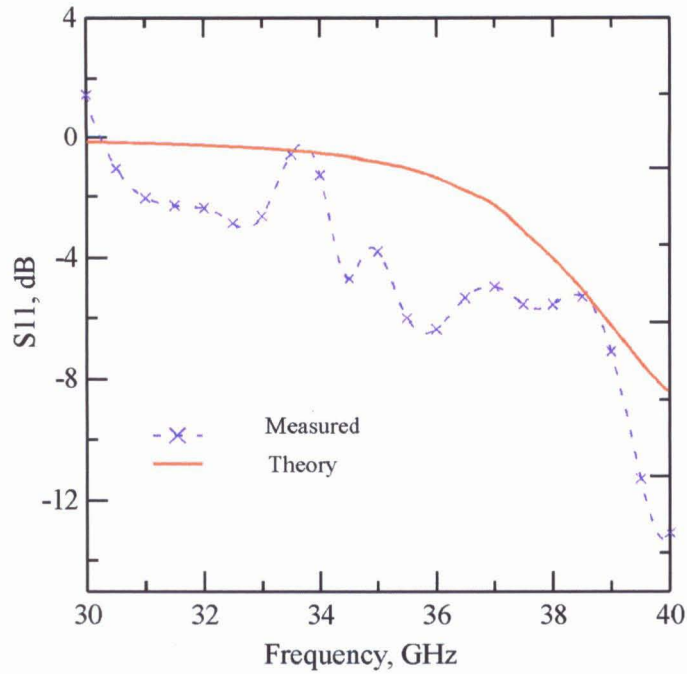


**Figure 4.12.** Reflection measurement from the grid amplifier chip without the polarizers. The error could be caused by the sensitivity to placement precision.

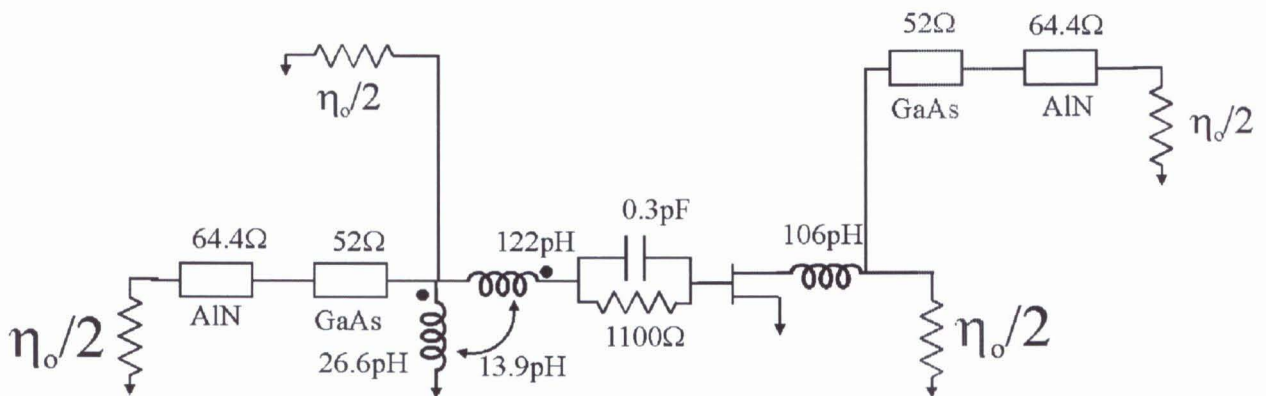


**Figure 4.13.** Circuit model used to predict the reflection from the grid amplifier.

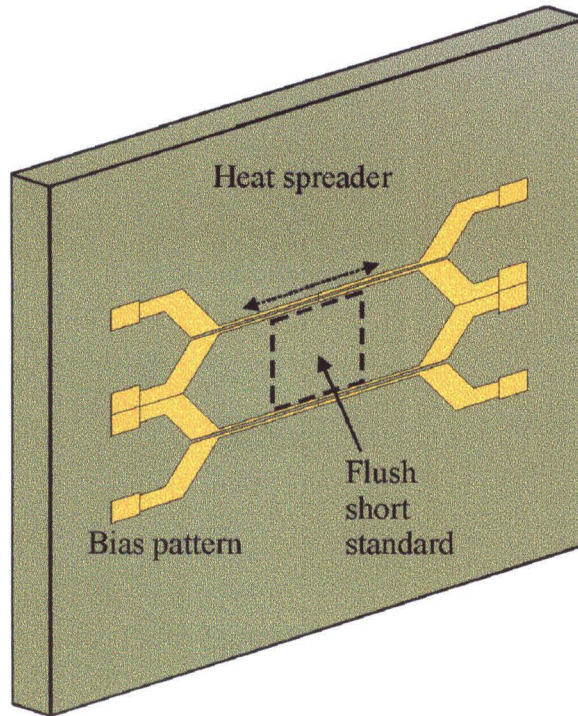


**Figure 4.14a.** Flush short standard for reflection calibration. The metal short lies on the opposite side of the substrate from the bias traces making it difficult to align in exactly the same location between the traces as the delayed short standard.

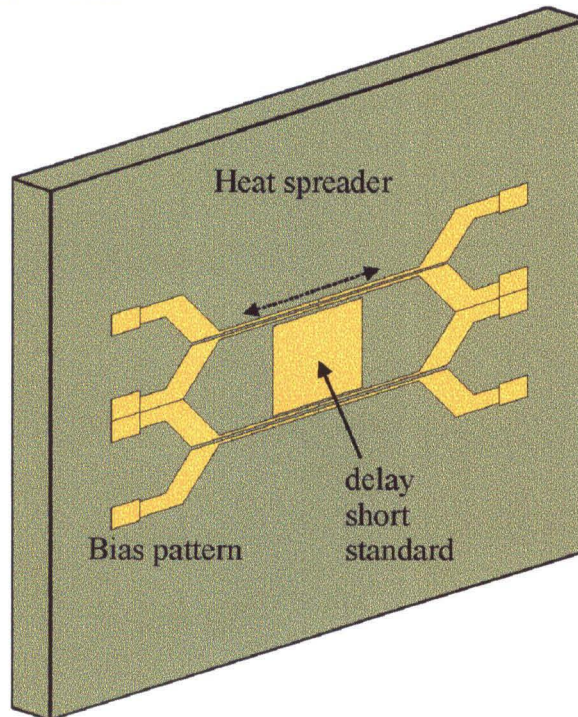


**Figure 4.14b.** Delayed short standard for reflection calibration.

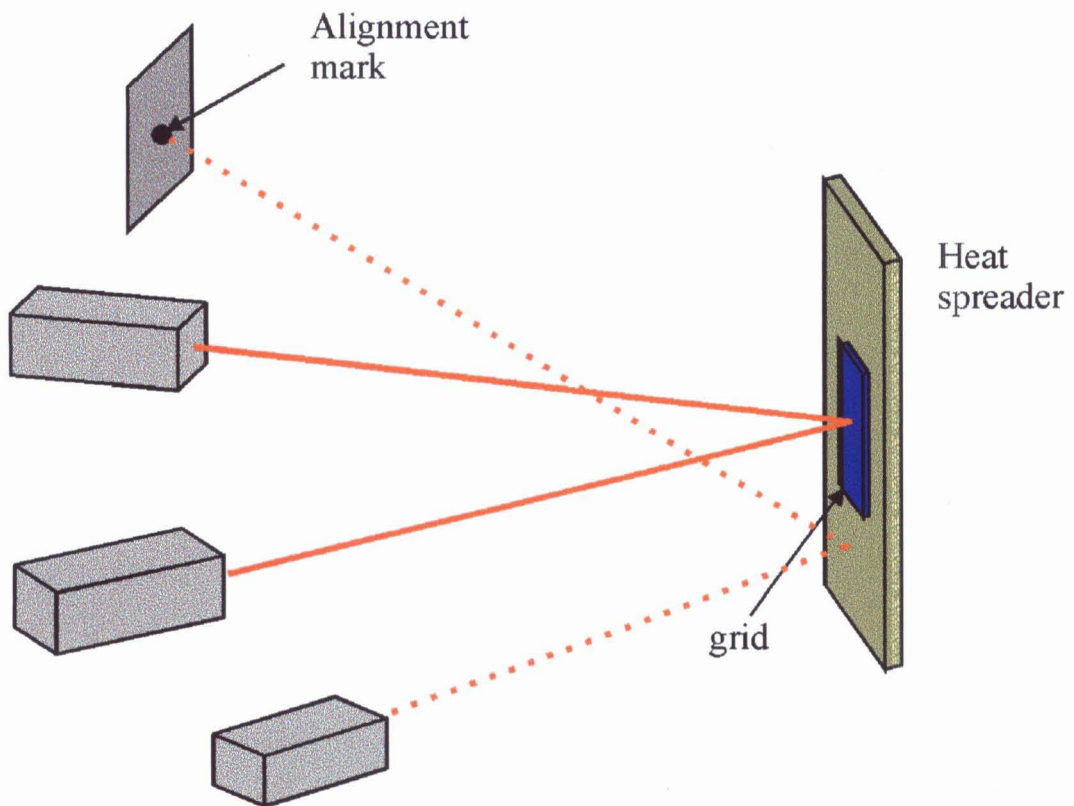


**Figure 4.15.** Setup to control the placement and angle orientation of the grid amplifier. Note that a reflected beam can be aligned with a mark on a target to track the angular position of the grid. The heat spreader is sufficiently reflective that a 5 mW HeNe laser can be used.

pler was connected to the receive horn to measure the output power from the grid amplifier. Calibration of the system proceeds exactly as for small signal measurements, with the test port power on the network analyzer set at about  $-45$  dBm. This calibrates out the gain of the TWTA and the couplers. Since the gain of the TWTA is constant<sup>4</sup> over the power sweep range, the saturation curve of the grid amplifier can be measured by recording its gain at each level of drive power (as measured by a power meter connected to the couplers). Since the network analyzer measures the grid's gain directly, its gating functions can be used to eliminate spurious room reflections that can cause misleading power measurements. Figure 4.16 shows the setup used for power measurements, and figure 4.17 shows the power performance of the grid amplifier measured with this technique.

---

<sup>4</sup>The gain of the TWTA remained constant to well below .1 dB over the entire power sweep range. Since the gain of the TWTA is about 60 dB, very little drive produces quite a lot of power.

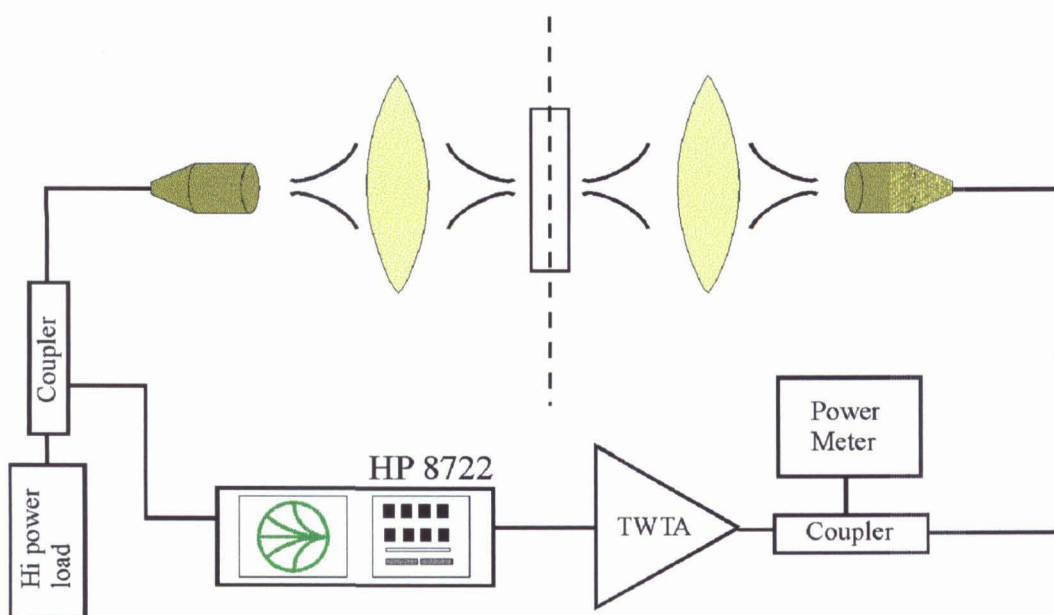


**Figure 4.16.** Measurement setup used for power measurements. The TWTA is a 20 W amplifier by Amplifier Research.

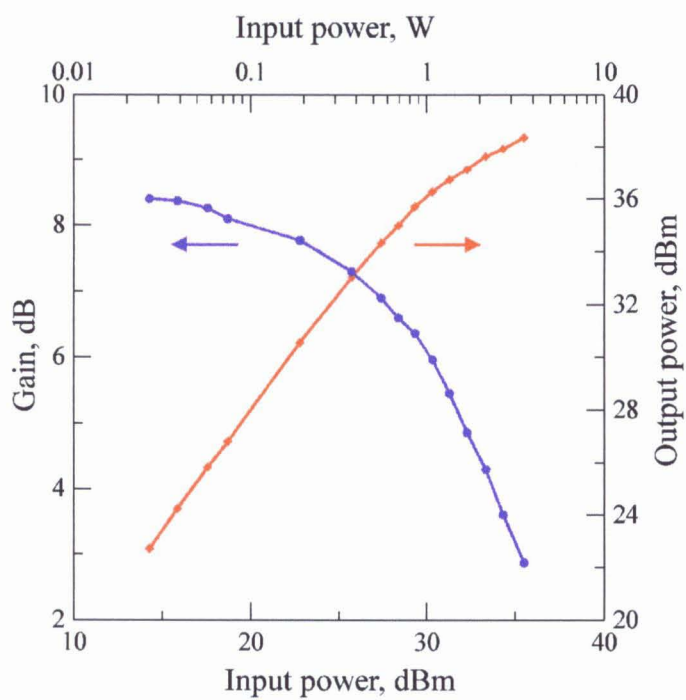


**Figure 4.17.** Measured power performance of the grid amplifier.

## References

- [1] D.R. Gagnon, "Highly Sensitive Measurements With a Lens-Focused Reflectometer," *IEEE Trans. Microwave Theory and Tech.*, vol. 39, No. 12, December 1991.
- [2] N.J. Koliass, "Monopole Probe Based Millimeter-Wave Quasi-Optical Amplifier Arrays," Ph.D. thesis, Cornell University, August 1996.
- [3] C.M. Liu, "Monolithic Grid Amplifiers," Ph.D. thesis, California Institute of Technology, May 1996.
- [4] M. Kim, "Grid Amplifiers," Ph.D. thesis, California Institute of Technology, December 1993.
- [5] M.P. De Lisio, "Hybrid and Monolithic Active Quasi-Optical Grids," Ph.D. thesis, California Institute of Technology, December 1996.
- [6] P.F. Goldsmith, "Quasi-Optical Techniques," *Proc. IEEE*, vol. 80, No. 11, November 1992.
- [7] A. Yariv, *Optical Electronics*, Orlando: Holt, Rinehart and Winston, Inc., 1985.
- [8] R.J. Wylde, D.H. Martin, "Gaussian Beam-Mode Analysis and Phase-Centers of Corrugated Feed Horns," *IEEE Trans. Microwave Theory and Tech.* vol. 41, No. 10, October 1993.
- [9] B.C. Deckman, J.J. Rosenberg, "Ka-Band Quasi-Optical Measurements Using Focused Gaussian Beams," to be presented at the ARFTG symposium, June 2000.
- [10] W.H. Press, B.P. Flannery, S.A. Teukolsky, W.T. Vetterling, *Numerical Recipes In Pascal*, Cambridge: Press Syndicate of the University of Cambridge, 1989.
- [11] A. Siegman, *Lasers*, Mill Valley: University Science Books, 1986.
- [12] D. Rutledge, *Caltech EE 153 Course Notes*, Chapter 15, 1996.

## Chapter 5

### A Kim Oscillator

#### 5.1 OSCILLATOR THEORY

Inexorably tied to the study and design of oscillators is the theory of feedback. An oscillator feeds part of its output back to its input, where it is mixed with a drive signal<sup>1</sup>. If the returned signal is in phase with and has at least the same magnitude as the drive signal, it can sustain itself in the absence of the drive signal. This is similar to the idea of a “friendly echo” in a digital flip-flop: once the output from the logic gates has been fed to the input, the input signal can be removed without disturbing the output. With reference to figure 5.1, this “friendly echo” situation can be described by the following equations [1], once the drive signal has been removed:

$$V_o = AV_f \tag{5.1a}$$

$$V_o = \frac{-1}{K}V_f \tag{5.1b}$$

From (5.1), it is clear that the interaction between what is called the “gain stage,”  $A$ , and the “feedback stage,”  $k$ , determine the behavior of the oscillator (or, for that matter, any active circuit that uses feedback), so a fast overview of feedback is germane here.

---

<sup>1</sup>The first oscillator is usually attributed to E. H. Armstrong circa 1917, although he ultimately lost the patent battle to Lee DeForest. Snippet from W. B. Bridges.

## 5.2 TRADITIONAL FEEDBACK THEORY

The study of feedback usually begins with the model shown in figure 5.1. “A” represents an active stage to provide gain, and “K” represents a feedback network. The transfer function of the system, H, is given as

$$H = \frac{A}{1 + AK}. \quad (5.2)$$

Here it is assumed that A and K are truly *feed-forward* networks; that signals can travel through them in only the direction of the arrows. As such, K and all that is connected to it do not load the input circuit.

To find H, a given circuit is usually broken up into a feed-forward network to get A, and then into a feedback network to get K. Here is found a bit of trouble. In many practical circuits the “A” and “K” blocks are not obvious, and are usually not truly feed-forward. The result is that K really does load the input, so breaking the circuit up destroys the loading effects. In an attempt to resolve the loading problem, it is common to model the loading of the input circuit with some additional elements to facilitate the process of breaking the circuit. This technique has been discussed in detail in [2], where it is acknowledged that the accuracy of the technique depends on the A and K blocks not loading each other. The resulting A and K circuits are analyzed, and the results plugged into (5.2). Using the loading model to analyze “A” introduces an accuracy concern. The

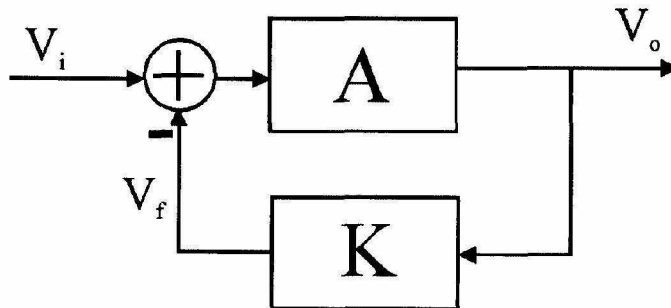


**Figure 5.1.** Block diagram for a typical feedback analysis. The blocks are assumed to feed the signals only in the direction of the arrows. It is also assumed that K doesn't load A.

conditions under which the load model provides accurate results are not given by the analysis; rather the circuit needs to be analyzed as a whole to get at the answer. This would seem to defeat the purpose of analyzing any circuit with the feedback model at all. But there remains another problem with this technique.

As a direct result of the *feed-forward* behavior of  $K$ , the gain of the  $A$  circuit can go to zero without driving the output to zero. This suggests that even the form of (5.2) needs revision.

### 5.3 AUGMENTED FEEDBACK ANALYSIS

The various effects of the feed-forward behavior of  $K$  can be included in a feedback analysis by adjusting the model in figure 5.1 to include a forward path. The analysis that follows is due to Middlebrook [3]. Figure 5.2 shows an augmented feedback circuit model. Analysis of the model shows that the transfer function of the circuit is given by

$$H = \frac{1}{K} \frac{AK}{1 + AK} + \frac{H_0}{1 + AK}. \quad (5.3)$$

Defining  $T$  as  $AK$ , the loop gain in figure 5.1, (5.3) can be rewritten as

$$H = \frac{1}{K} \frac{T}{1 + T} + \frac{H_0}{1 + T}. \quad (5.4)$$

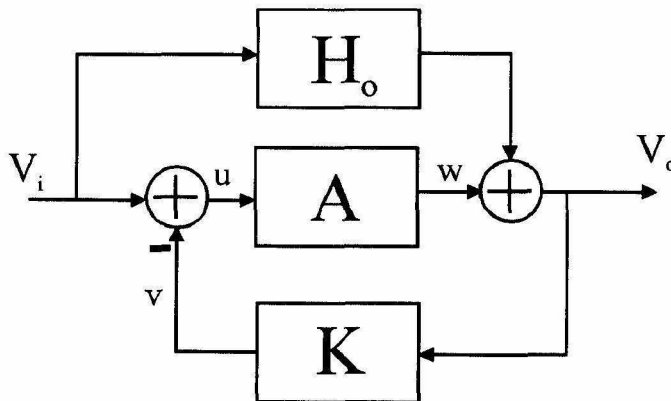


**Figure 5.2.** Augmented feedback model.  $H_0$  accounts for the feed-forward behavior of the circuit.

Here, the analysis of the circuit does not require that the loop be broken to find  $A$ ;  $A$  is always included with  $K$  in the loop gain. The various quantities in (5.4) can be calculated directly from the circuit by way of injecting a test source.

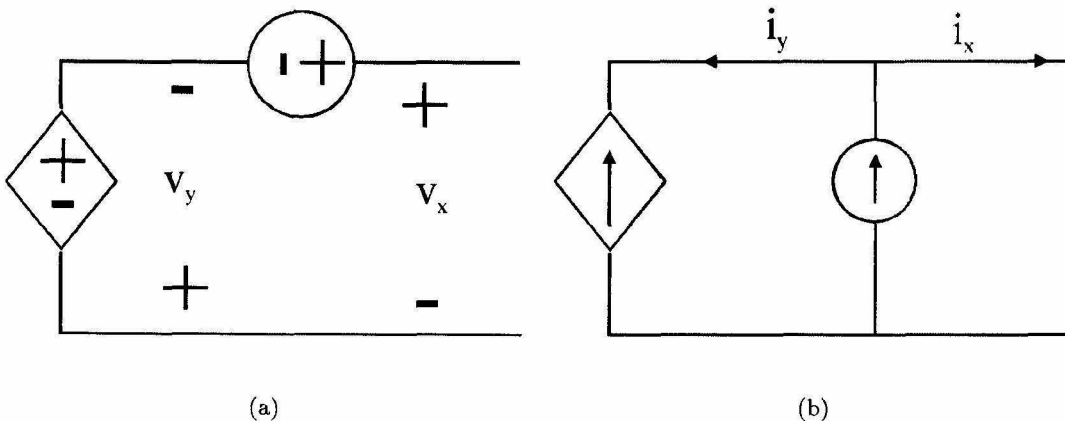
$T$  can be found by turning off the input, injecting a test source, and then finding  $u/v$ .  $K$  can be found by the use of null double injection where the two injected sources are the same test source used to find  $T$ , and the system input. With  $u$  nulled,  $V_{in} - V_{out}K = 0$ .  $K$  is then given by

$$K = \left. \frac{V_{out}}{V_{in}} \right|_{u \text{ nulled}} .$$

$H_0$  is also found by the use of null double injection. Adjusting an injected test source and the system input so that  $w$  is nulled,

$$H_0 = \left. \frac{V_{out}}{V_{in}} \right|_{w \text{ nulled}} .$$

Appropriate test source selection is illustrated in figure 5.3 [3]. This technique usually involves no more difficulty in analysis than the “traditional” technique, and includes the various effects of loading and forward paths through  $K$ .



The dependent source is the circuit's active element. The independent source is an injected test source. From [3],  $T = \left[ \frac{v_y}{v_x} \right]_{input \ off}$ ,  $H_\infty = \left[ \frac{output}{input} \right]_{v_y=0}$ ,  $H_0 = \left[ \frac{output}{input} \right]_{v_x=0}$  (a);  $T = \left[ \frac{i_y}{i_x} \right]_{input \ off}$ ,  $H_\infty = \left[ \frac{output}{input} \right]_{i_y=0}$ ,  $H_0 = \left[ \frac{output}{input} \right]_{i_x=0}$  (b).

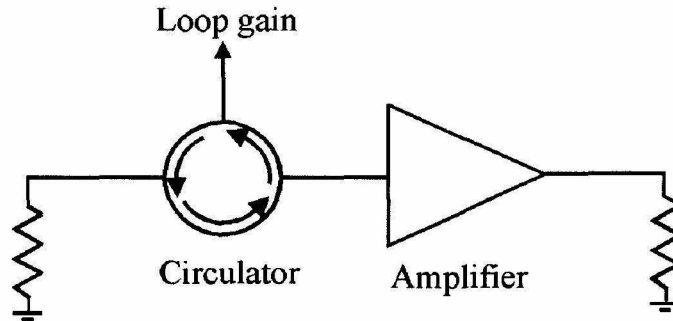


**Figure 5.2.** Circuit model used to find the loop gain. The circulator delivers the signal from the excitation port directly to the active circuit, and returns a reflected signal to the test port.

Once the various quantities of (5.4) have been found, the stability of the system can be determined by various methods. One common technique is to apply the Nyquist criteria. If  $K$  is a constant in the frequency range of interest, then the zeros of  $1 + T$  are shown to be the poles of (5.4), and the Nyquist criteria can be directly applied. If  $K$  adds either zeros or poles to (5.4), then the Nyquist criteria must be applied to (5.4) directly. In simple terms, the Nyquist criteria for stability require that the loop gain be less than unity when its phase (considering the  $-$  in figure 5.2) crosses zero. Gain and phase margins are usually determined as the difference between the operating gain and unity at zero phase, and the difference between the operating phase and zero at unity gain. The Nyquist criteria and several margins are discussed in detail in [2, 4].

The Nyquist criteria can also be applied from a reflection perspective. When the magnitude of the reflection coefficient from a two-port network reaches unity with zero phase, the system will oscillate. Figure 5.4 shows a circuit model that can be used to check the stability of a two-port.

#### 5.4 GRID OSCILLATORS

External feedback can be applied to the grid amplifier of chapter 3 to induce it to oscillate. The technique is to construct a device that rotates the polarization of the output beam by  $90^\circ$  and reflects it back to the input. Kim [5] constructed a  $1/4$ -wave plate, or “twist reflector,” using an angled polarizer backed by a mirror

to rotate the polarization of the beam and feed it back to a grid amplifier. Such a device showed tunable frequency oscillations between 8 and 11 GHz [5]. Figure 5.5 illustrates the technique. The polarizer of the twist reflector can be treated as either a perfect reflector to energy polarized along its wires and invisible to energy polarized perpendicular to them, or it can be analyzed electromagnetically to generate an S parameter model. Kim's analysis [5] assumes an ideal polarizer. Advancements in computing and simulation speed allow electromagnetic analysis of the structure for S parameters. Following this technique, an ideal 4-port device is defined to resolve an impinging electric field into components parallel and perpendicular to the wires of the polarizer. Figure 5.6 shows the layout of the device. The scattering matrix is that of a simple rotation and is given by:

$$\begin{pmatrix} 0 & \cos(\theta) & 0 & \sin(\theta) \\ \cos(\theta) & 0 & -\sin(\theta) & 0 \\ 0 & -\sin(\theta) & 0 & \cos(\theta) \\ \sin(\theta) & 0 & \cos(\theta) & 0 \end{pmatrix}$$

where  $\theta$  is the angle between the polarizer wires and the impinging electric field. To ports 2 and 4 of the rotator, appropriate devices can be connected to represent the polarizer. Transmission lines and shorts can then be connected to complete the model. To check the accuracy of the model, a twist reflector considerably larger than the measurement beam was constructed. Figure 5.7a shows the circuit used to model the twist reflector, and 5.7b shows a comparison between simulation and measurement. The polarizer for the measurement was constructed of beryllium-copper wire wound around a frame of #2-56 threaded rod.

Using the grid amplifier of Chapter 3, an oscillator was constructed by adding a small twist reflector constructed on a low dielectric duroid. The thickness of the substrate is  $\lambda/4$  at 37 GHz. Since the twist reflector replaces the input side polarizer that normally tunes the output circuit, a double-slug tuner was added behind the output side polarizer to supply output tuning. A photograph of the oscillator and twist reflector is shown in figure 5.8.

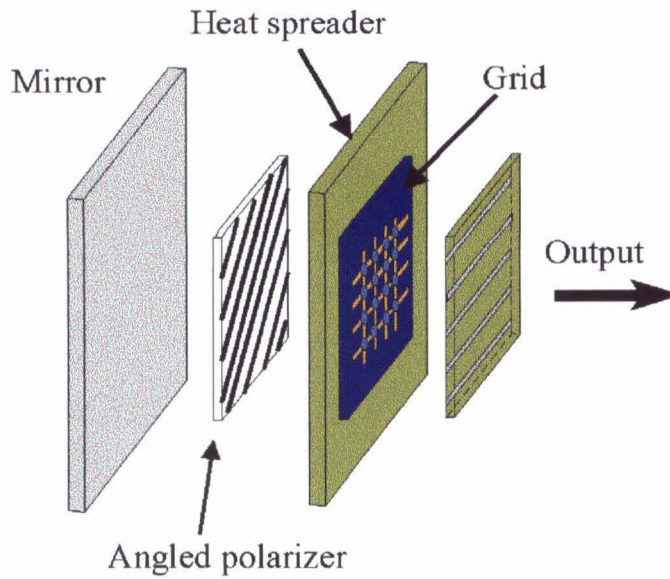


**Figure 5.3.** Layout of the grid oscillator. The twist reflector rotates the polarization of an incident beam by  $90^\circ$ , and reflects it back to the grid, providing external feedback to the amplifier.

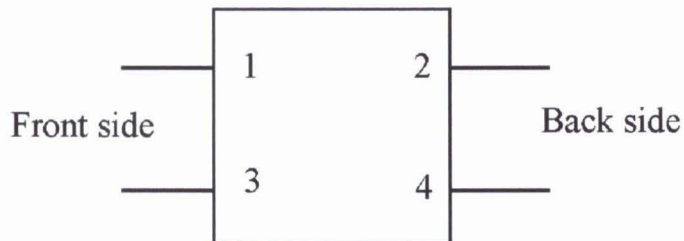


**Figure 5.4.** 4-port model for an ideal rotator. The function is to resolve the polarization of an incident beam into components parallel and perpendicular to the wires of the polarizer. Port 1 represents the gate polarization, and port 3 represents drain polarization on the input side. Port 2 gives parallel polarization with the grid wires, port 4 gives perpendicular polarization to the wires.

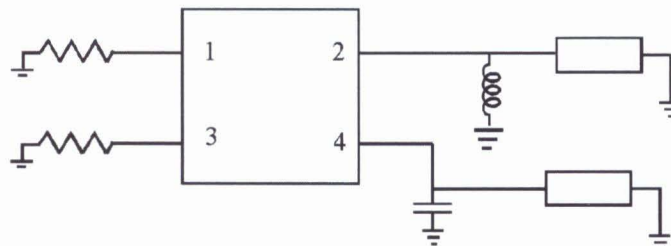


**Figure 5.5a.** Circuit model used to predict the behavior of the twist reflector. The lengths of the transmission lines are adjusted to determine the resonant frequency of the structure. The reactances model the polarizer structure.

By changing the position of the twist reflector, the frequency of the oscillator can be adjusted. Figure 5.10 shows a frequency plot of the EIRP of the oscillator. Assuming that the surface of the oscillator has a uniform field distribution, Friis' formula can be used to estimate the radiated power from the grid. Figure 5.10(b) shows a plot of the grid oscillator radiated power assuming a uniform field at the surface of the grid, and the peak in the curve is seen to be about 1 watt at 38.1 GHz. Figure 5.11 shows plots of the RF power performance of the grid oscillator against DC dissipation at 38 GHz. Figure 5.11a shows a DC to RF efficiency plot against radiated power, and figure 5.11(b) shows a plot of grid power against DC dissipated power. The peak efficiency of the grid is shown to be about 6%. Figure 5.12 shows an H-plane beam scan, compared to an ideal-

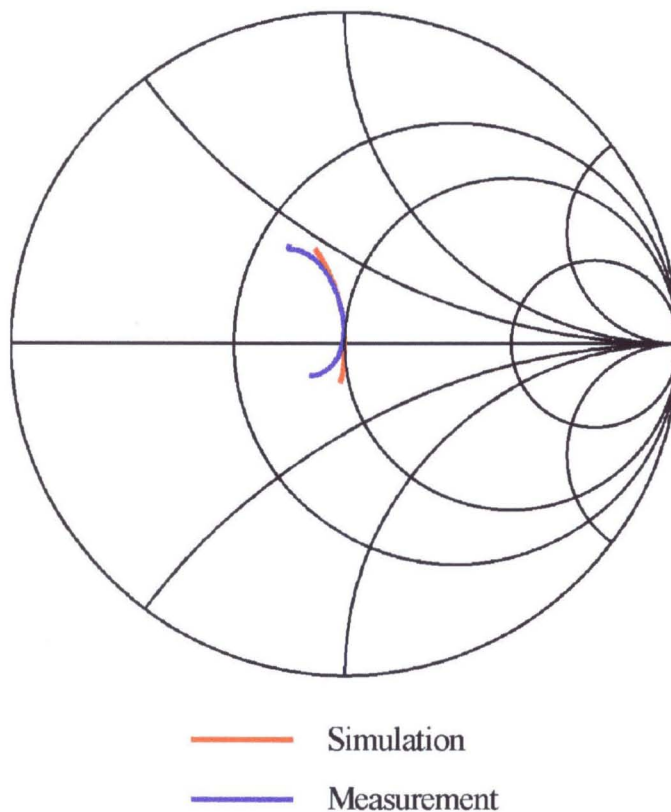


**Figure 5.5b.** Simulation and measurement for a twist reflector using BeCu wire wrapped around #2-56 threaded rod.

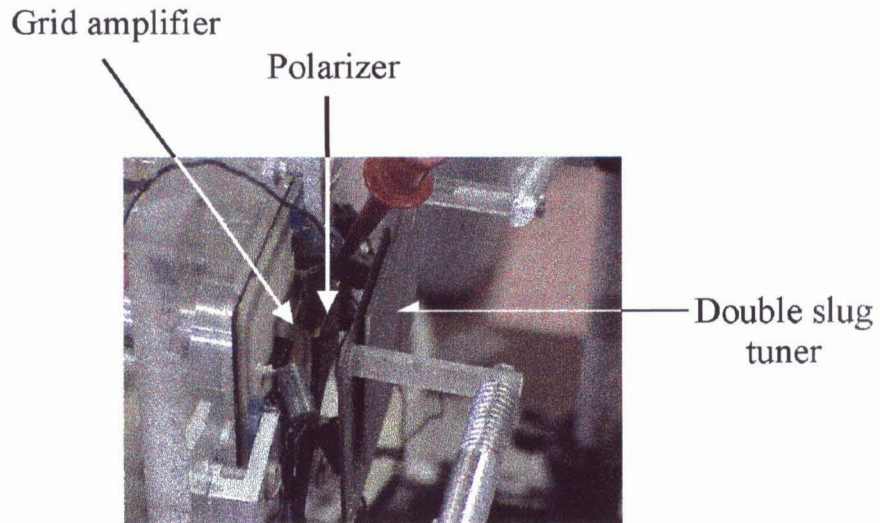


**Figure 5.6a.** Photograph of grid oscillator output side. The double slug tuner is used to match the output circuit.

Twist reflector  
fixture

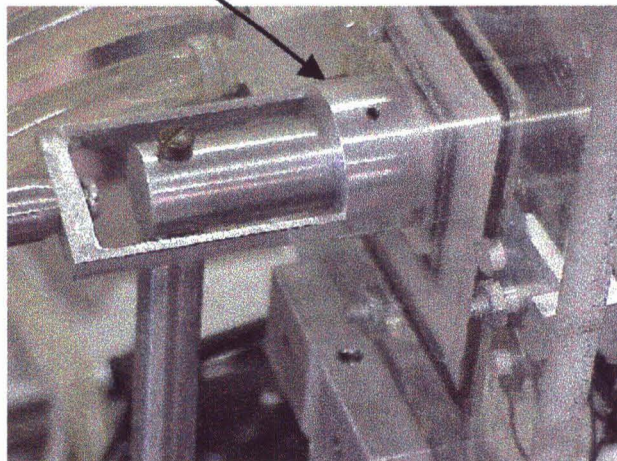


**Figure 5.6b.** Photograph of grid oscillator feedback side. The fixture holds a twist reflector constructed of low dielectric duroid. Adjustment of the fixture's position tunes the frequency of the oscillator.

ized model of diffraction from a uniformly illuminated aperture in an absorbing plane, a problem that can be solved by hand. It can be shown that the far-field diffraction pattern measured in either the E or H plane is given by

$$E(x, y, z) = \frac{j \cos^2\left(\frac{\theta}{2}\right)}{\lambda r} \int_S E(x', y') e^{jk \sin(\theta)y'} dx' dy' \quad (5.5)$$

where  $E(x', y')$  is the field in the aperture. (5.5) is a fourier transform of the aperture field. The solution is given by

$$E(x, y, z) = \frac{ja^2 \sin(k \sin(\frac{\theta}{2}))}{\lambda r k \sin(\frac{\theta}{2})} \cos^2\left(\frac{\theta}{2}\right).$$

The normalized power density is proportional to the square of the field. Some of the disparity between the model and the measured pattern may be that the model assumes an absorbing aperture surrounded by free space, while the oscillator's radiating surface is mounted on aluminum nitride and has a polarizer close to the surface. The substrate and polarizer effects may be similar to the effects of the reflector and directors of a Yagi antenna.

Estimating the phase noise performance of the oscillator from a plot of its spectrum gives about  $-106$  dBc/Hz at 1 MHz off the carrier. One reason that the phase noise is so strong is that there is no filter to sharpen the spectrum. Work currently in process attempts to construct a phase-locked loop with an electronically tunable twist reflector. The PLL may clean up the phase noise considerably. Prediction based on the electronics alone suggest a phase noise performance that is about 20 dB better than the measurement here. Simple experimentation (tapping the table) suggests that a significant source of the phase noise here is mechanical vibrations. All of the devices (the tuning slabs, polarizers, and oscillator itself) are mounted on long rods and suspended close to 1 foot above the bench. Such fixturing is quite vulnerable to vibrations. Figure 5.9 shows a typical free-running spectrum of the Kim oscillator.

Figure 5.12 shows the radiation patterns from the oscillator. Note that the H-plane pattern is narrower than a diverging beam from a uniform aperture. One reason for this may be resonator modes setup between the tuning plates.

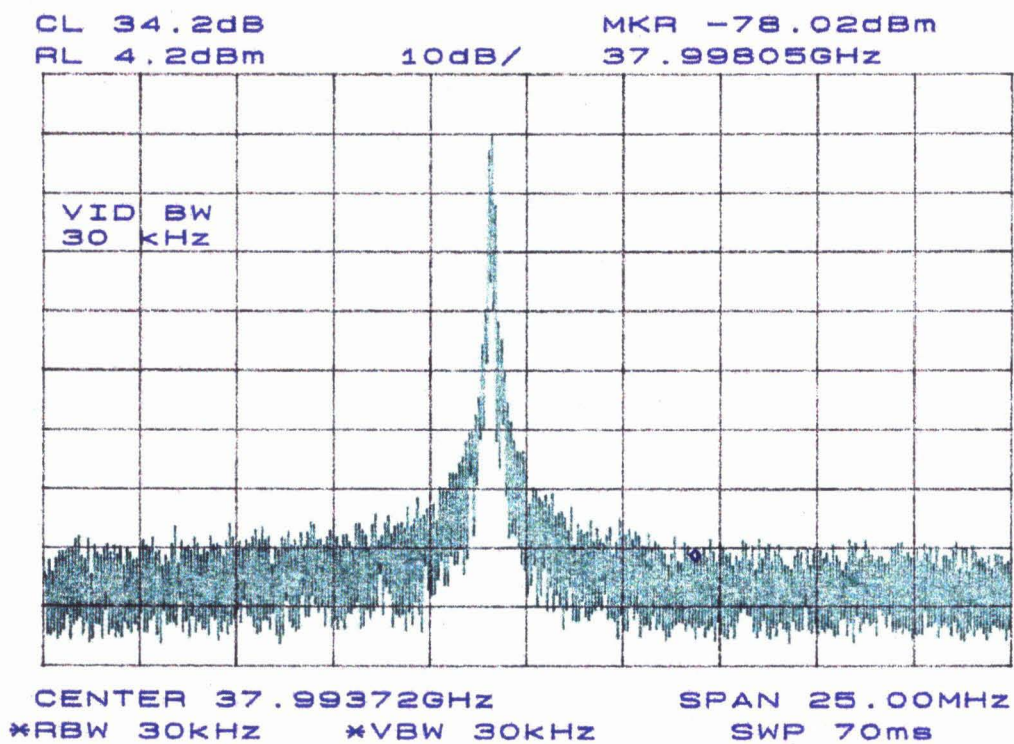


**Figure 5.7.** Typical spectrum for the Kim oscillator. An estimate of the phase noise at 1 MHz off the carrier is  $-106$  dBc/Hz.

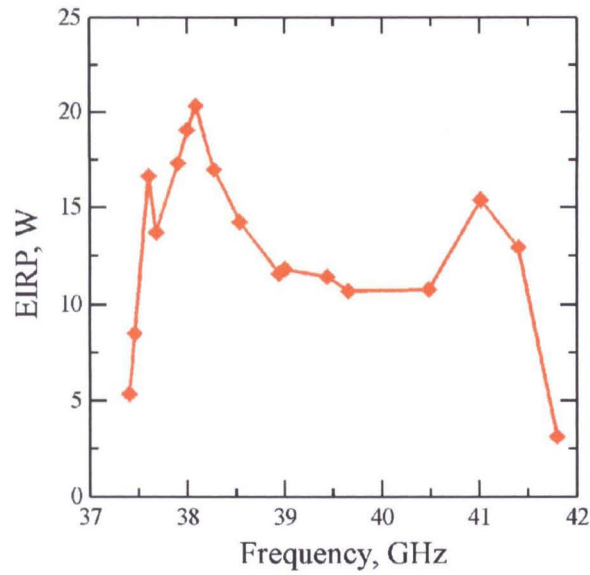


**Figure 5.8a.** Effective Isotropic Radiated Power from the grid oscillator. The notch in the curve at about 37.3 GHz results from a second oscillation developing at 41 GHz. The peak in the power curve is shown to be about 43 dBm, or 20 watts. Assuming a uniform field in an aperture surrounded by an absorbing plane, the radiated power is 1 watt.

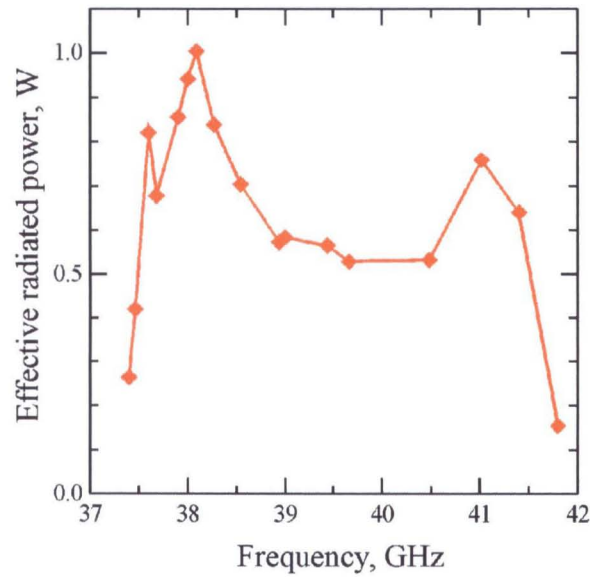


**Figure 5.8b.** Figures of merit are after Gouker, equations 2,3 [6].

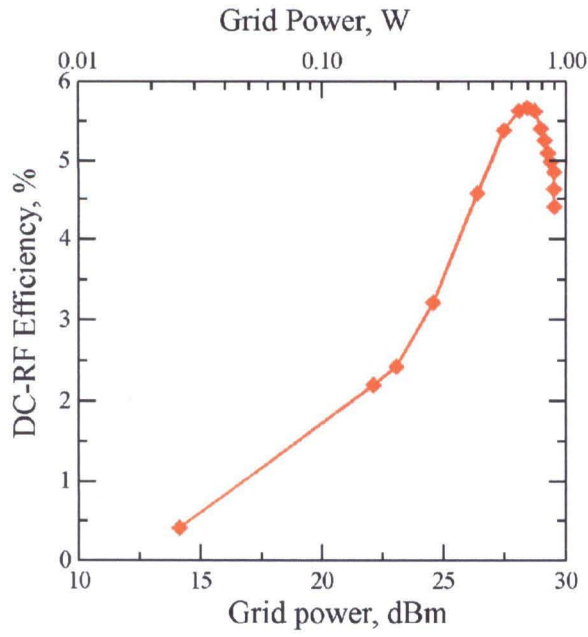


Figure 5.9a. DC-RF efficiency of the grid oscillator. The peak efficiency is shown to be about 6%.

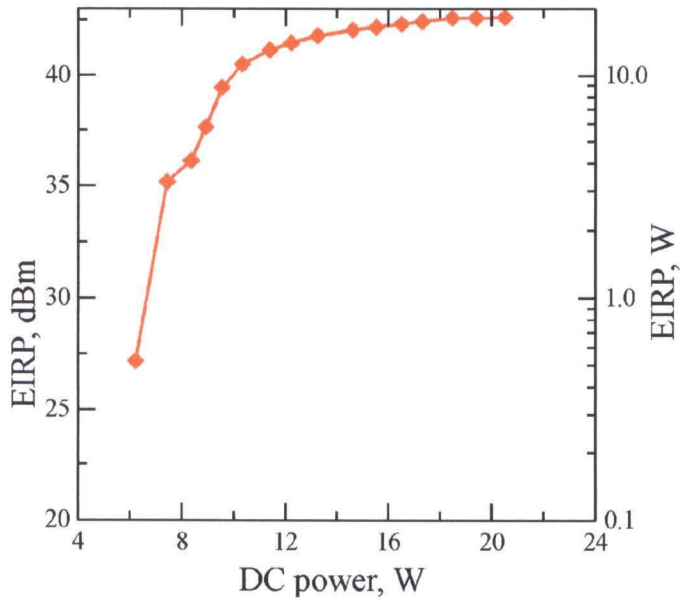
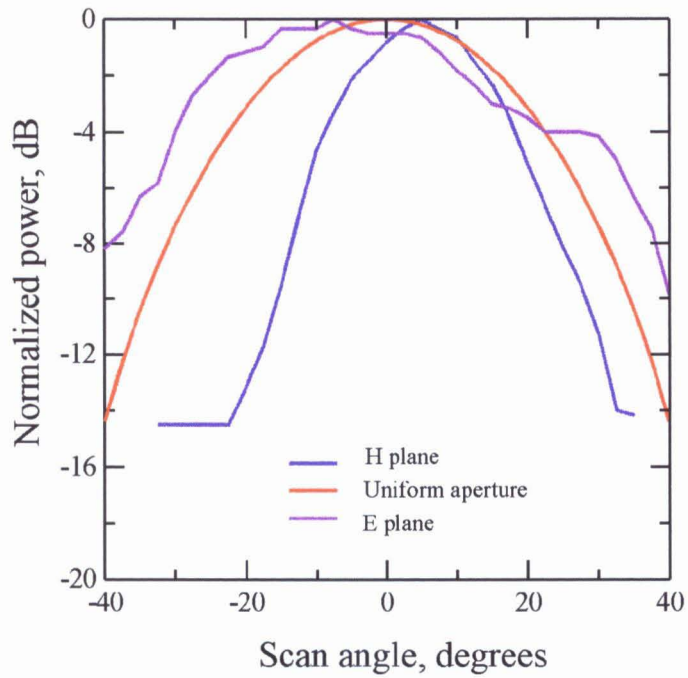


Figure 5.9b. Grid power against DC dissipated power.



**Figure 5.10.** H-plan scan of the grid oscillator at 38.1 GHz. The model is a uniformly illuminated aperture in an absorbing plane. The difference may be due to the presence of the substrate and polarizer in the measurements.

### References

- [1] D. B. Rutledge, *The Electronics of Radio*. Cambridge: Cambridge University Press, 1999, ch. 11, pp. 204-205.
- [2] A. S. Sedra, K. C. Smith, *Microelectronic Circuits*. Fort Worth: Saunders College Publishing, 1991, ch. 8, p. 599.
- [3] R. D. Middlebrook, J. Lindal, *Design-Oriented Analysis, Caltech EE114 Course notes*. 1995.
- [4] N. Nise, *Control Systems Engineering*. Redwood City: Benjamin/Cummings Publishing, 1992, ch. 10, pp. 517-536.
- [5] M. Kim, *Grid Amplifiers*. Pasadena: Caltech Ph.D. thesis, 1993.
- [6] M. Gouker, "Toward standard figures-of-merit for spatial and quasi-optical power combined arrays," *IEEE Trans. Microwave Theory Tech.*, vol. 43, pp. 1614-1617, July 1995.
- [7] H. Kogelnik, "Imaging of Optical Modes-Resonators with Internal Lenses," *The Bell System Technical Journal*, vol. 44, pp. 455-495, March 1965.
- [8] H. Kogelnik, T. Li, "Laser Beams and Resonators," *Proc. of the IEEE*, vol. 54, no. 10, pp. 1312-1329, October 1966.
- [9] A.G. Fox, T. Li, "Resonant Modes in a Maser Interferometer," *Bell System Technical Journal*, vol. 40, pp. 453-488, March 1961.
- [10] G.D. Boyd, J.P. Gordon, "Confocal Multimode Resonator for Millimeter Through Optical Wavelength Masers," *Bell System Technical Journal*, vol. 40, pp.489-508, March 1961.

## Chapter 6

### Future Work

#### 6.1 A 10-W GRID

Several difficulties building grid amplifiers have been heat removal and biasing. The 5-watt grid amplifier is a 16x16 design, dissipating about 22 watts over its area of 1 cm<sup>2</sup>. Its bias lines are gold traces about 5  $\mu\text{m}$  thick, and 50  $\mu\text{m}$  wide. The DC resistance of the traces gives a voltage drop that, for higher power grids, may prevent a good bias. A 10-watt design currently in progress uses a unit cell that is 580  $\mu\text{m}$  on a side, and has 24 rows by 22 columns. As such, the DC dissipation increases by a factor of two, and the voltage drop in the bias lines increases as well.

To address the thermal issue, a diamond substrate can be used as a heat spreader. Recently, various suppliers have begun to deliver optically flat CVD diamond substrates up to a few millimeters thick, and several inches in diameter. The nominal thermal conductivity of diamond is 1000 W/mK; about a nine-fold improvement over aluminum-nitride. Since the DC dissipation of the higher power grid increases by about two, the use of a diamond heat spreader allows operation of the grid at a temperature rise that should still be about four times lower: For thin substrates and highly conductive materials,  $\delta T = Q/2\pi KT$ .

Assuming an electrical conductivity of gold at  $2 \cdot 10^7$  S/m, the voltage drop from the center of the grid to the edges should be about 0.32 volt. Since optimal

power performance of the grid amplifier requires a gate-source voltage of about  $-0.3\text{ V}$ , a difference of  $0.32\text{ V}$  is fatal. Consequently, a method of tracking the source voltage drop with the gate voltage is necessary, without affecting the RF performance of the grid. Figure 6.1 shows a schematic view of the unit cell design, and edge bias plan, that allows the gate voltage to track the source voltage. The idea is to bleed a fraction of the source current away to a resistive “tracking” trace that maintains a constant voltage drop between the source bias line and the tracking line. Provided that the gates of the transistors draw negligible DC current compared to the tracking current, a resistive divider can be used to set the gate voltage. From symmetry arguments applied to the circuit of figure 6.1, the value of  $R_2$  is given by

$$R_2 = -\frac{2}{CI_D}(V_{gb} + V_g)$$

where  $V_{gb}$  is the gate bias supply, and  $V_g = -V_{gs}$ . Setting  $V_{gb} = -3\text{V}$ , and  $V_g = 0.3\text{V}$ ,  $R_1 = 300\Omega$ , and  $R_2 = 2700\Omega$  with  $R_g = .138\Omega$ .  $C$  is the fraction of the drain current bled off to the tracking circuit,  $1/20$  here. Control of the gate bias voltage can be achieved by changing the gate bias supply. The tracking circuit degrades the efficiency of the grid performance slightly. Resistor  $R$  in the tracking trace is given by

$$R = \frac{1 - C}{C}$$

such that its voltage drop matches the voltage drop in the source bias line. The fractional change in the grid’s efficiency is given by

$$\Delta\eta = \frac{V_{ds}}{V_{ds} + C|V_{gb}|}$$

where  $V_{ds}$  is the grid’s drain-source voltage. For  $V_{ds} = 3$ , and  $V_{gb} = -3$ ,  $\Delta\eta = 0.95$ . Hence the 17% efficiency of the grid amplifier in chapter 3 would change to 16%, a change of about 1%. Figure 6.2 shows a cross section of the grid amplifier on its diamond substrate.

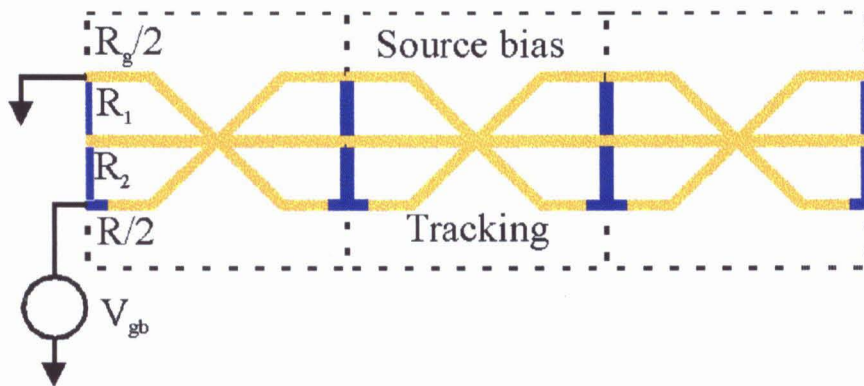


**Figure 6.1.** Unit cell layout including a  $V_{gs}$  tracking network. The voltage drop in the source bias line is tracked by the resistors added between the two traces.

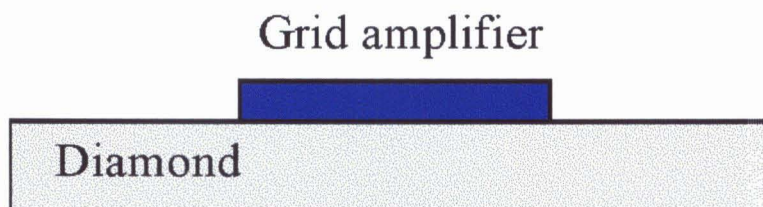


**Figure 6.2.** Grid amplifier mounted on a diamond heat spreader. Note that since the thermal conductivity of diamond is much greater than the conductivity of AlN, the higher power grid amplifier should operate at a lower temperature.

## 6.2 WAVEGUIDE FEED

To date, grid amplifiers have been used with free-space feeds. Packaging of the grid amplifier in a waveguide requires a waveguide that has an electric field distribution that is “optimally” flat across its aperture. There are several ways to approach the problem. Hubert [1] and others have designed a waveguide with dielectric loads on the walls to give a flat field over the aperture area of the guide, as shown in figure 6.3a. The trouble with this approach is that coupling the appropriate mode into the wall loads is difficult, and there is an immediate power loss that results from energy in the loads. With a flat field across the waveguide aperture, the power efficiency of the guide, defined as the ratio between the power in the aperture of the guide to the total power, is given by

$$\eta = \frac{W}{\int_0^t \sin^2(k_x x) dx + W} = \frac{W}{W + \frac{\lambda_0}{8\sqrt{\epsilon_r - 1}}}$$

where  $k_x$  is given by

$$k_x = \frac{2\pi}{\lambda_0} \sqrt{\epsilon_r - 1}.$$

Figure 6.3b shows a plot of the efficiency against the wall load dielectric constant. Higher efficiency means higher wall load dielectric, but that causes difficulty in coupling to the proper mode.

Another approach has been used by Kim [2]. Kim’s technique is to fabricate resonant circuits in the dielectric loads of the walls to cause them to appear as high impedance planes. The advantage is that the thickness of the dielectric can be made very small, and a material with good thermal conductivity can be used. The difficulty is that Kim’s structure is difficult to fabricate. The structure also stores energy in the walls.

A third approach is to exploit several higher order modes in an oversized waveguide to give a field distribution that resembles the Chebychev filter characteristic. Figure 6.4 shows a test structure. Carefully transitioning the width

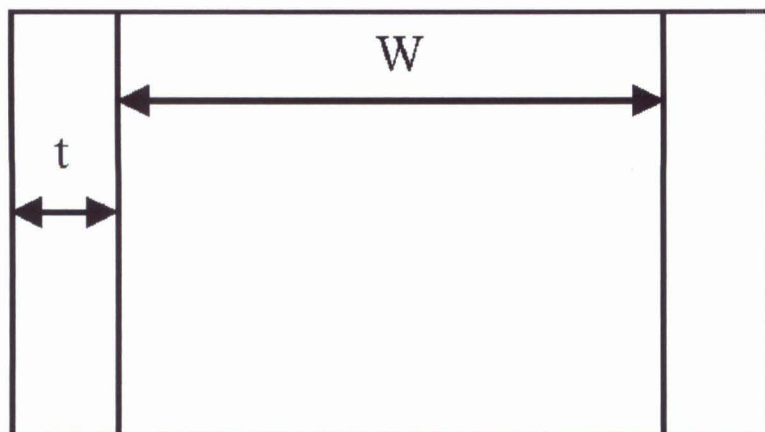


**Figure 6.3a.** Waveguide design for dielectric wall loads. The field in the aperture of the guide is TEM. It may be difficult to launch the correct mode in this structure.

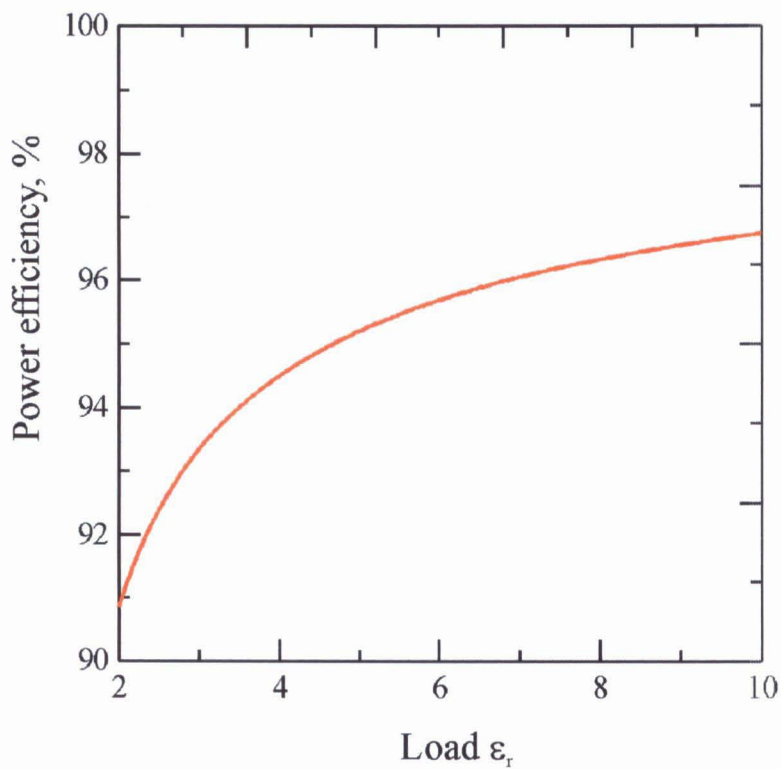


**Figure 6.3b.** Power efficiency of the wall-loaded waveguide. Higher dielectric constant material loading the walls yields higher efficiency, but makes it more difficult to couple the correct mode to the structure.

of the guide, two higher order modes are excited that interact to give a field that rolls off quickly near the walls, but is relatively flat over most of the guide. Exciting the proper ratios between the modes is accomplished by the step design. Figure 6.4b shows HFSS simulations and measurements for a test transition terminated in an absorber. The design difficulty is to match the impedance of the various modes to the surface impedance of the grid amplifier so as to minimize reflections that will disturb the field distribution. Development of this structure is currently under way at Caltech by Lawrence Cheung.

Combining all the various design improvements together, figure 6.5 shows a cartoon view of the next generation grid amplifier. Note that this layout is well suited to applications involving casagrain fed antennas.

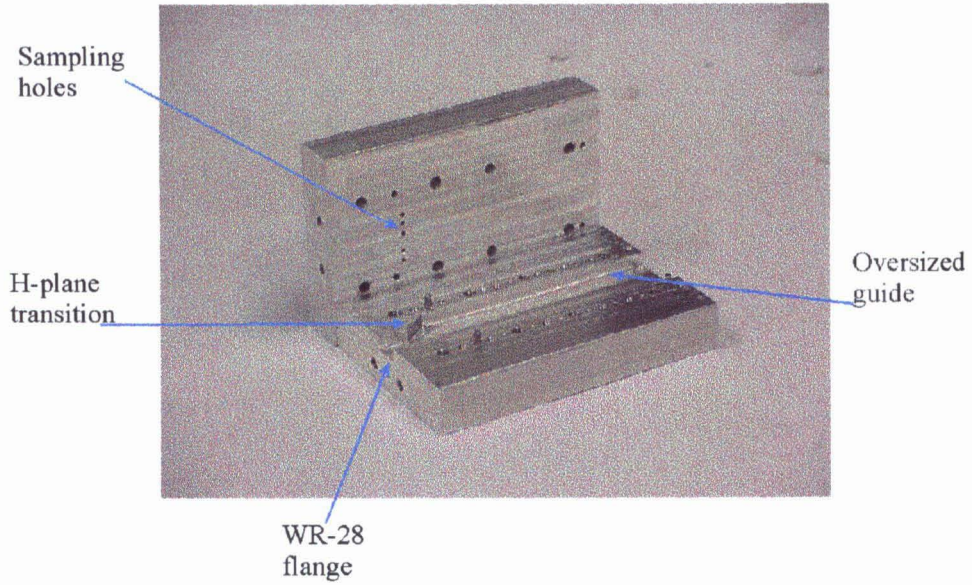


**Figure 6.4a.** Test structure for the H transition of the mode converter drive.

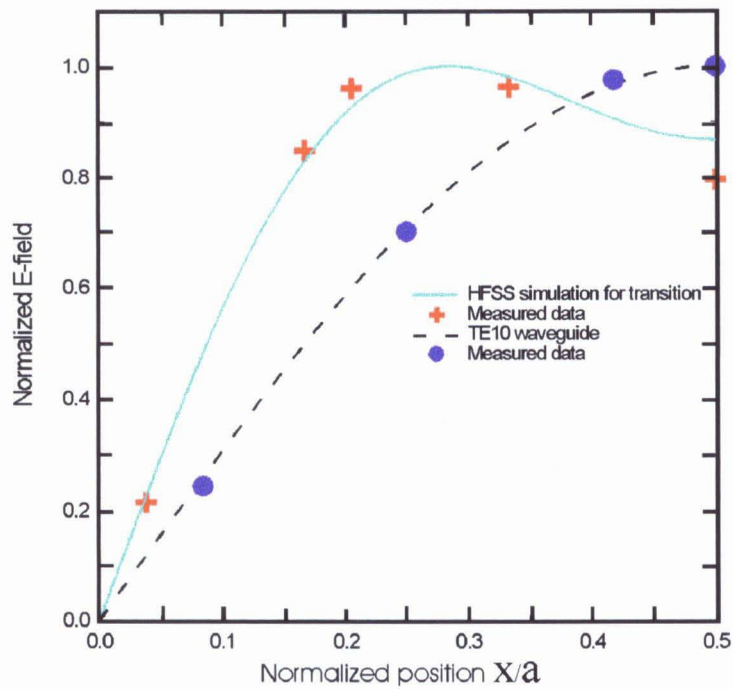


**Figure 6.4b.** Test measurement for the H transition. Comparison is shown for a standard  $TE_{10}$  waveguide to verify the accuracy of the probing technique.

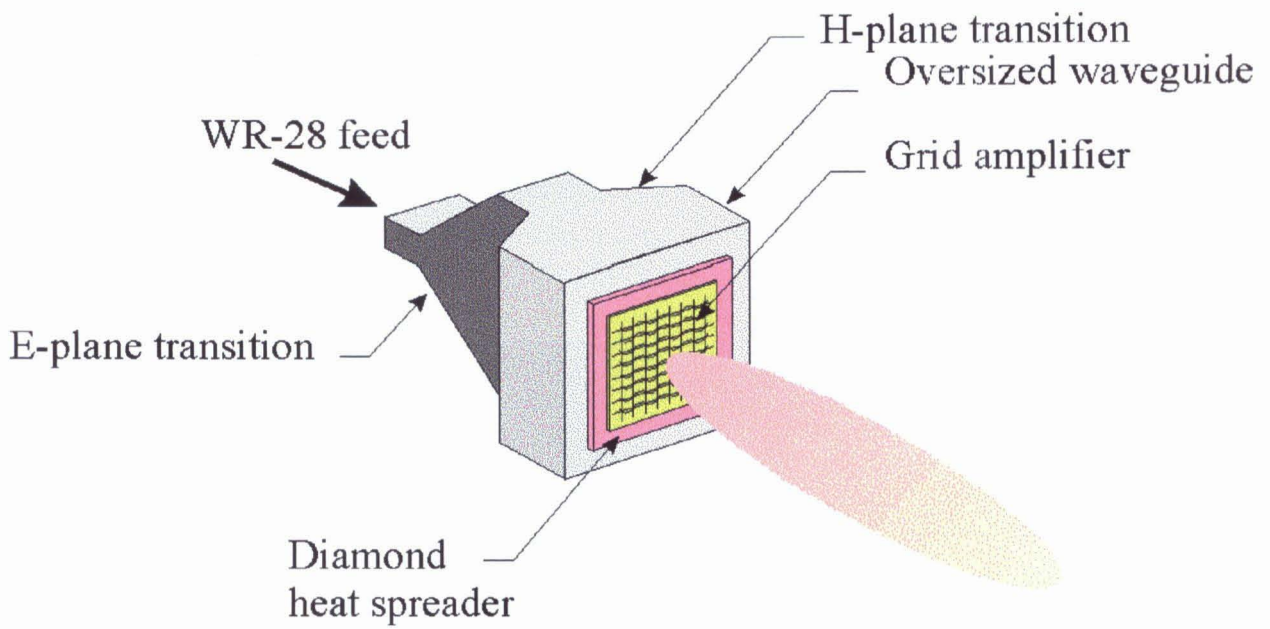


**Figure 6.5.** Grid amplifier design incorporating the mode converter to drive it.

### 6.3 ELECTRONICALLY TUNED GRID OSCILLATOR

The twist reflector of chapter 5 was constructed from printed copper traces on a duroid substrate. Though this structure provides excellent feedback, tuning requires movement of the structure with respect to the grid amplifier surface. J. Rosenberg has developed a reactive twist reflector that can be electronically tuned. The frequency of the grid oscillator can then be set electronically, without the need to move the twist reflector. Electronic tuning allows incorporation of the grid oscillator into a phase-locked loop to narrow the bandwidth and improve the noise performance of the structure. The design is also well suited to the waveguide feed so that its output can be directed into a standard guide. Figure 6.6 shows a layout of the structure. Metal pattern resonates at a frequency determined by the capacitance of the varactor diodes, and behaves as a metal polarizer at that frequency. As such, it replaces the twist reflector polarizer to provide for electronic tuning of the grid's oscillation frequency.

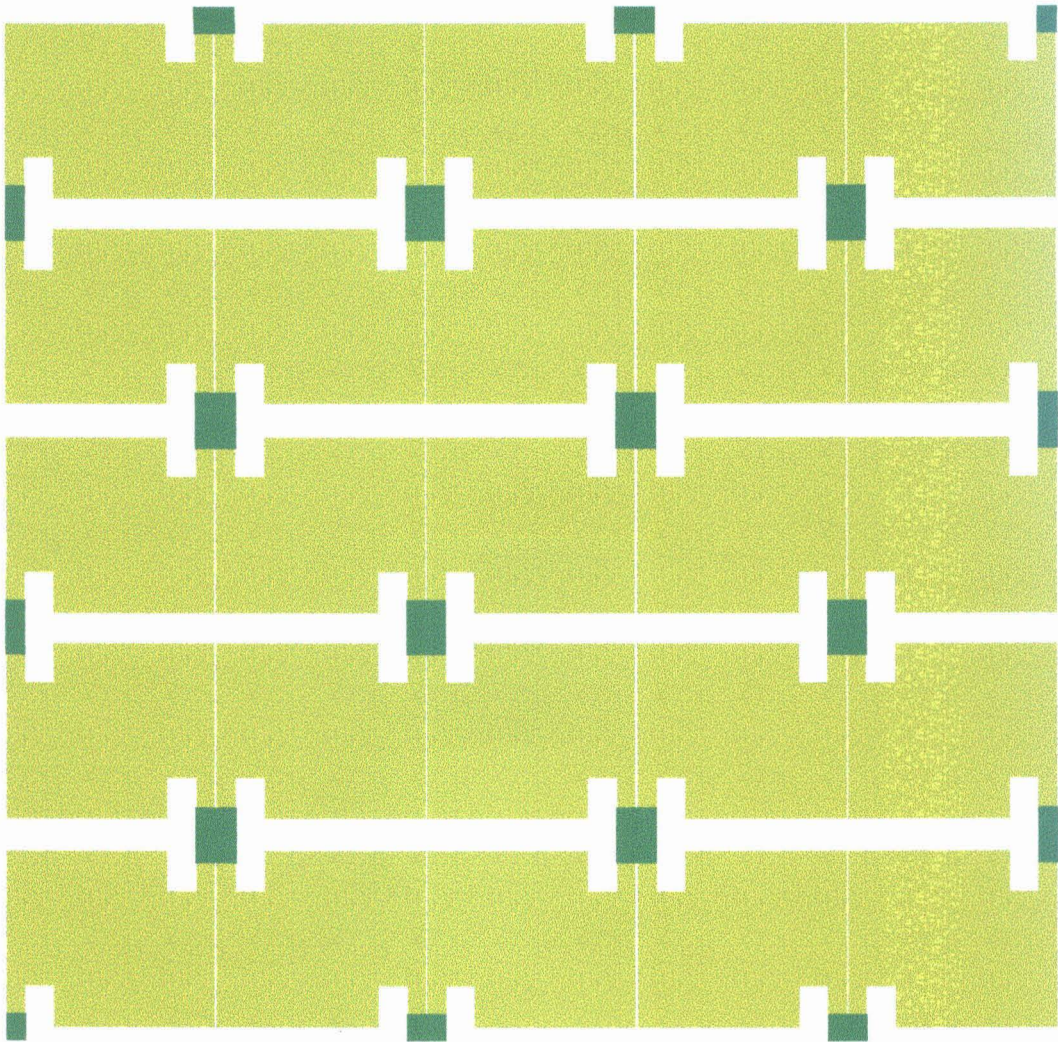


**Figure 6.6.** Metal pattern for a tunable polarizer. The capacitance of the varactor diodes determines the resonant frequency of the structure, and thereby can tune the oscillation frequency of the Kim oscillator.

**References**

- [1] J. Hubert, L. Mirth, S. Ortiz, A. Mortazawi, "A 4 Watt Ka-Band Quasi-Optical Amplifier," *IEEE International Microwave Symposium Diag.*, pp. 551-554, June, 1999.
- [2] M. Kim, J.B. Hacker, A.L. Sailer, S. Kim, D. Sievenpiper, J.A. Higgins, "A Rectangular TEM Waveguide with Photonic Crystal Walls for excitation of Quasi-Optical Amplifiers," *IEEE International Microwave Symposium Diag.*, pp. 543-546, June, 1999.

## Appendix 1

### Gaussian Beams

Various discussions of Gaussian beams begin by writing down a simplified wave equation, and then immediately writing down the answer [2]:

$$\left(\nabla_t^2 - j2k\frac{\partial}{\partial z}\right)\Psi(r, \phi, z) = 0$$

$$\Psi = \sqrt{\frac{2}{\pi w^2}} \exp(-r^2/w^2 - jkz - j\pi r^2/\lambda R + j\alpha).$$

Something about the juxtaposition of the seemingly complicated answer directly following an innocent-looking differential equation with no intermittent mathematics presented suggests to me that the answer resulted from an educated guess. This is indeed the case, and it is the purpose of this appendix to motivate that guess. The derivation that follows is due to Bridges [3].

Making the usual assumption of a time-harmonic, traveling wave solution to Maxwell's equations, the Helmholtz equation shows that

$$(\nabla_t^2 + \partial^2/\partial z^2 + k^2)\bar{E} = 0$$

where  $\nabla_t^2 = \frac{\partial^2}{\partial x^2} + \frac{\partial^2}{\partial y^2}$ . We proceed by assuming that the propagating wave is plane polarized; that is,

$$\bar{E} = E_x \Psi(x, y, z) e^{j(\omega t - kz)} \hat{x}$$

where  $\Psi(x, y, z)$  is the solution to the wave equation that we're trying to guess. Inserting the expression for the field into the wave equation yields the expression

$$\left( \nabla_t^2 + \frac{\partial^2}{\partial z^2} - j2k \frac{\partial}{\partial z} \right) \Psi(x, y, z) = 0.$$

Now we require that the solution  $\Psi$  not diverge too rapidly in  $z$ ; that [2]

$$\left| \frac{\partial^2 \Psi}{\partial z^2} \right| \ll \left| 2k \frac{\partial \Psi}{\partial z} \right|.$$

This being the case, the wave equation reduces to

$$\left( \nabla_t^2 - j2k \frac{\partial}{\partial z} \right) \Psi(x, y, z) = 0.$$

In cylindrical coordinates,

$$\nabla_t^2 = \frac{\partial^2}{\partial r^2} + \frac{1}{r} \frac{\partial}{\partial r} + \frac{1}{r^2} \frac{\partial^2}{\partial \phi^2}.$$

Looking for a solution that is symmetric about the propagation axis,  $\partial^2/\partial \phi^2 = 0$  so the wave equation is written as

$$\left( \frac{\partial^2}{\partial r^2} + \frac{1}{r} \frac{\partial}{\partial r} - j2k \frac{\partial}{\partial z} \right) \Psi(r, z) = 0. \quad (A1.0)$$

Guessing the solution to this simplified wave equation begins with knowledge of the far-field distribution of a gaussian field at a reference plane. Provided that the amplitude of the field at the reference plane is gaussian distributed, and its phase is flat, the far-field amplitude is gaussian, and the phase is spherical. This is known from the Huygens-Fresnel diffraction integral. As such, we expect that the solution should have a gaussian amplitude component and a spherical phase component. Mathematically, this can be expressed as

$$\Psi(r, z) = \Psi_0 \exp\left( \frac{jkr^2}{2R(z)} - \frac{r^2}{w^2(z)} \right) \quad (A1.1)$$

where the first term in the exponent gives a spherical phase front, and the second term gives a gaussian amplitude distribution.  $R(z)$  is the radius of curvature of

the diverging beam,  $w(z)$  is the  $1/e$  radius of the field, and  $k$  is the propagation constant. (A1.1) is usually rewritten in the form

$$\Psi(r, z) = \Psi_0 \exp \left[ -j \left( \frac{1}{R(z)} - \frac{2j}{kw^2(z)} \right) \frac{kr^2}{2} \right]. \quad (\text{A1.2})$$

We now guess that our solution represents the correct  $r$  dependence. Now an experience factor. Define a *complex beam parameter*,  $q$ , by

$$\frac{1}{q(z)} = \frac{1}{R(z)} - j \frac{\lambda}{\pi w^2(z)}$$

and rewrite (A1.2) as

$$\Psi(r, z) = \Psi_0 \exp \left[ -j \left( P(z) + \frac{kr^2}{2q(z)} \right) \right]. \quad (\text{A1.3})$$

Note that  $P(z)$  can be complex, so the amplitude of (A1.3) can change with  $P(z)$ . Plugging (A1.3) into the wave equation (A1.0) gives the relation

$$\left[ \frac{k^2}{q^2} \left( \frac{dq}{dz} - 1 \right) r^2 - 2k \left( \frac{dP}{dz} + \frac{j}{q} \right) \right] \Psi(r, z) = 0.$$

This results in two individual equations to ensure the above equation is satisfied for all  $r$ :

$$\frac{dq}{dz} = 1$$

$$\frac{dP}{dz} = \frac{-j}{q}.$$

It is easily found that

$$q(z) = z + q_0$$

leading to

$$\frac{dP}{dz} = \frac{-j}{z + q_0}$$

which has the solution

$$P(z) = -j \ln(z + q_0) + P_0.$$

$P_0$  is a constant of integration, so we can choose it. Let  $P(0) = 0$  so that  $P_0 = j \ln(q_0)$ . The expression for  $P(z)$  now becomes

$$P(z) = -j \ln\left(\frac{z + q_0}{q_0}\right),$$

leading to

$$\Psi(r, z) = \Psi_0 \exp\left[-\ln\left(1 + \frac{z}{q_0}\right) - j \frac{kr^2}{2(q_0 + z)}\right].$$

At this point it's a good idea to take a step back and remember what we were trying to accomplish. The solution we sought should have a gaussian amplitude profile, but with the  $j$  in the second term of the exponent, this is not looking promising. But since  $q_0$  is yet another constant of integration, we are at liberty to choose it. Let  $q_0 = jz_c$ , where  $z_c$  is a real number. Then

$$\Psi(r, z) = \exp\left[-\ln\left(1 + j \frac{z}{z_c}\right) - \frac{jkr^2}{2(z + jz_c)}\right].$$

Now there is a gaussian amplitude term, but we've gotten a real mess with the  $\ln$  term. But it can be simplified:

$$\exp\left[-\ln\left(1 + j \frac{z}{z_c}\right)\right] = \frac{1}{\sqrt{1 + \left(\frac{z}{z_c}\right)^2}} \exp\left[j \tan^{-1}\left(\frac{z}{z_c}\right)\right].$$

Fiddling a bit with algebra finally results in the expression for the electric field that we've been after:

$$E(r, z) = E_0 \frac{w_0}{w(z)} \exp\left[j \left(kz - \tan^{-1}\left(\frac{z}{z_c}\right)\right) - \left(\frac{r^2}{w^2(z)} + j \frac{kr^2}{2R(z)}\right)\right]$$

where

$$w^2(z) = w_0^2 \left[1 + \left(\frac{z}{z_c}\right)^2\right]$$

$$R(z) = z \left[1 + \left(\frac{z_c}{z}\right)^2\right]$$

$$z_c = \frac{\pi w_0^2}{\lambda}.$$

$w_0$  is the  $1/e$  radius of the gaussian beam at the plane where the phase is flat; the reference plane. Substitutions can be made to result with the same answer that was given in the beginning. *Voila!*

Now that we've got the field solution for the gaussian beam, we find that transforming it through the several optical components by multiplying the ABCD matrices of the elements commonly used in geometric optics and then transforming  $q(z)$  by the resulting overall ABCD matrix:

$$q_2 = \frac{Aq_1 + B}{Cq_1 + D}$$

where  $q_1$  is the beam parameter at the starting point, and  $q_2$  is the beam parameter at the field point of interest. This is the "experience factor" used to derive the gaussian beam field solution.